ANUL XLVII 2002

STUDIA
UNIVERSITATIS BABEŞ-BOLYAI

PHYSICA

1

EDITORIAL OFFICE: Gh.Bilaşcu no. 24, 3400 Cluj-Napoca ♦ Phone 0264-40.53.52

SUMAR - CONTENTS - SOMMAIRE - INHALT

STUDIA UNIVERSITATIS BABEŞ-BOLYAI, PHYSICA, XLVII, 1, 2002

EFFECT OF DEPOSITION PRESSURE ON THE STRUCTURAL AND ELECTRIC PROPERTIES OF Bi:2201 THIN FILMS

A. V. POP*, GH. ILONCA*, MARIANA POP, R. DELTOUR*****

ABSTRACT. Epitaxial Bi:2201 thin films were deposited on $SrTiO_3$ (100) substrates using an inverted magnetron sputtering method. The influence of sputtering gas pressure on the structural properties were studied by X-ray diffraction(XRD), scanning electron microscopy (SEM) and atomic force microscopy (AFM). Optimal deposition conditions for superconducting films with smooth film surface and high epitaxial quality were obtained. Electrical resistance measurements function of temperature shows a metal-insulator transition for low deposition pressures.

Introduction

$Bi_2Sr_2CuO_{6+d}$ (Bi:2201) compound has the simplest structure in the Bi:22(n-1)n superconducting materials. It has only one (n=1) Cu-O layer per unit formula. If the Bi concentration is slightly than Sr concentration, Bi:2201 presents a superconducting transition below 20K [1]. Deposited as epitaxial thin films, Bi:2201 is a good opportunity for fundamental studies and applications of copper oxide superconductors. However, it is difficult to prepare high quality thin films for this use. The effect of coupling in a multilayers Bi: 2201/$CaCuO_2$ and Bi:2201/ $CaCuO_2$ were studied after a deposition by using molecular beam epitaxy [2]. Josephson junctions consisting of epitaxial Bi:2201 thin films were also fabricated by Nose et al. [3]. There are several reports about te epitaxial growth of Bi:201 thin films by magnetron sputtering using Pb-doped [4] and La doped [5] planar target. This technique was used to prepare high quality superconducting $Bi_2Sr_2Cu_2O_{6+d}$ (Bi-2201) thin films. Some deviations of the Sr stoichiometry or of both Bi and Sr are suggested to be necessary to obtain a superconducting 2201 phase [6-8]. Zhang et al. studied the transport properties in magnetic fields up to 23 Tesla of c-oriented epitaxial $Bi_2Sr_{2-x}La_xCu_1O_{6+d}$ thin films

---

* *Faculty of Physics,University Babes-Bolyai, 3400Cluj-Napoca, Romania*

** *Department of Plastic Deformation, Technical University,3400 Cluj-Napoca,Romania*

*** *Universite Libre de Bruxelles, Physique des solides, Bruxelles-Belgium*

prepared using magnetron sputtering [9, 10]. The evolution of the resistivity of single layer Bi:2201 thin films were studied at various oxygen concentration obtained after succesive annealing treatments or by using different concentration of oxygen in sputtering gas [11, 12].

In this paper, we will report our studies on deposition and structural properties of c-axis films deposited on $SrTiO_3$ substrates using inverted cylindrical magnetron sputtering.

Experimental

Bi:2201 thin films were deposited onto heated single crystal (100) $SrTiO_3$ substrates by using an inverted cylindrical DC magnetron sputtering. An off-stoichiometric target with a nominal composition Bi:Sr:Cu = 2. 1:1. 9:1 was home made by a solid state reaction method. The sputtering gas was a mixture of O_2 and Ar with a ratio1:1.

Films were deposited at different deposition pressures: 85 Pa (film A), 105 Pa (Film B) and 160 Pa (FilmC). Sputtering was carried out in DC mode with a power of 25W. Before each deposition the target was presputtered for 30 minute.

Substrate temperature was kept at 700^0C, an optimised temperature regarding to the epitaxial and compositional properties of the films, for all depositions in this study. Deposition time was 3 h leading to the thin film tickness of approximately 300nm. After deposition, the films were annealed at 500^0C in an oxygen atmosphere (100Pa) for 1h and further annealed at 245^0C and 70. 000 Pa of oxygen for 1h.

The deposited films were charachterized by X-ray diffraction (XRD), scanning electron microscopy (SEM) and atomic force microscopy (AFM).

The films are chemicaly patterned and equipped with silver sputtered contacts pads. The temperature dependence of the in-plane resistivity is measured by using a standard four probe dc method.

Results and discussion

XRD patterns for films A, B and C show a c-axis orientation revealed by the presence of peaks associated by (00l) planes as shown in Fig. 1 for film B.

Epitaxial property was studied using the rocking curve diffraction mode performed on the (0010) peak. The value of the full width at half maximum (FWHM) obtained from the rocking curves increases from 0. 35^0 to 0. 60^0 with increasing deposition pressure from 85 to 160 Pascal.

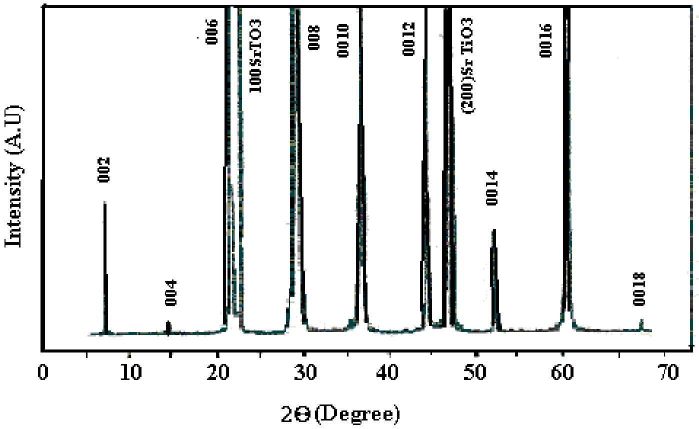

Fig. 1. *X-Ray diffraction pattern of Film B (Bi:2201)*

Figure 2 shows the SEM micrographs of the films A, B and C.

The influence of the deposition pressure on film surface morphology is clearly seen. Film A deposited at 85 Pa, has a rough surface with grains growing up (fig. 2a) and are visible cracks on the film surface. When the pressure is increased to 105 Pa, the film surface is smooth and free of any outgrowth (fig. b). With further increase the deposition pressure, the film roughness is increased and the surface is covered with outgrowths. The observed surface morphology can be partially explained with a phenomenological three-zone model [13]. This model shows that the adtom diffusion energy is decreased with an increasing deposition pressure at fixed substrate temperature.

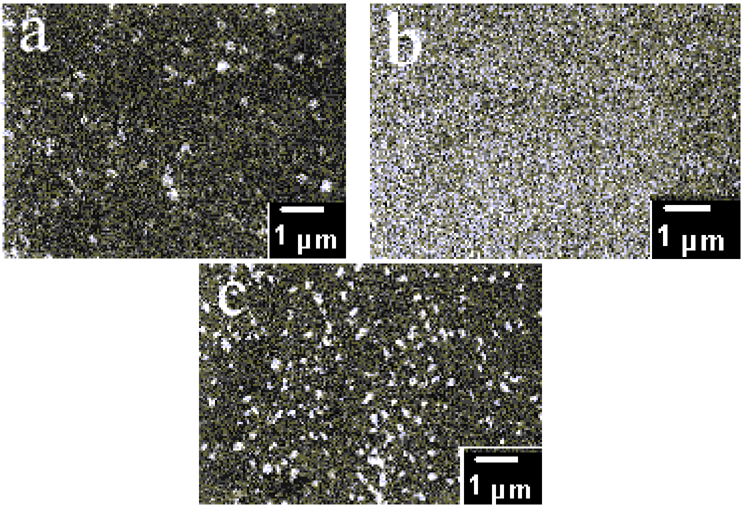

Fig. 2. *SEM micrographs of film A (a), Film B (b) and Film C (c).*

The Film C with rough surface and trapered crystalline grains has a low adtom diffusion energy. With decreasing the deposition pressure, adtom diffusion energy is sufficient to overcome the substrate and nucleation roughness and lead to a smooth surface (Fig. 2b). With a further decrease of the deposition pressure, large adtom diffusion energy lead to large grains produced by volume recrystallization (fig. 2a).

Fig. 3 shows the AFM images of film B.

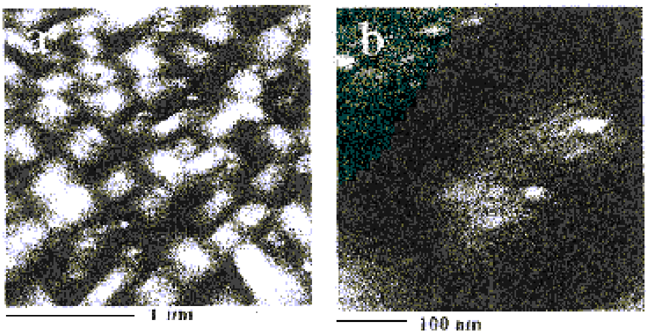

Fig. 3. *AFM image of film B (a) and detailed structure of te grain (b).*

It can be seen in Fig. 3a) that the film surface shows a oriented grain structure with grains parallel and perpendicular to each other, suggesting an a-b twinning structure. Fig. 4b)shows for one grain a step structure consisting of closed –loops.

The observed grain structure means that the films grow in a two dimensional mode on vicinal $SrTiO_3$ substrates. Similar results were obtained in the study of epitaxial $Bi_2Sr_{1-x}La_x\,Cu_2O_{6+d}$ [14].

Fig. 4 shows the dependence of electrical resistance as a function of temperature for the films A, B and C.

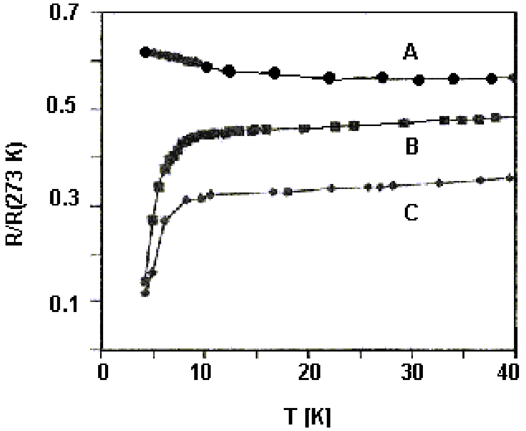

Fig. 4. *The reduced resistance function of temperatureof film A (95 Pa), film B (105 Pa) and film C (160)Pa.*

Film B and Film C show clearly a superconducting transition with a critical temperature T_c around 4. 5 K. For film A, an insulating behaviour appear at low temperature. Similar results were reported in ceramic samples of Bi:2201 if either small amounts of Sr and oxygen are removed from the structure [15]. We believe that the observed metal- insulator (M-I) should be due to the Sr deficiency in our epitaxial thin films. The variation in Sr stoichiometry may also influence te stoichiometry of oxygen and the observed M-I transition is a combination effect of Sr deficiency and the variation of oxygen content.

Conclusions

Epitaxial Bi:2201 thins films were deposited onto $SrTiO_3$ substrate by inverted cylindrical DC magnetron sputtering by using different pressure of sputtering gas.

The deposition pressure plays an important role regarding the superconducting transition, film surface morfology and epitaxial quality.

Epitaxial Bi:2201 thin films with smooth surface were obtained after the study of the influence of deposition pressure on the structural and electric properties of these samples.

REFERENCES

1. E. Sonder, B. C. Chakoumakos, B. C. Sales, Phys. Rev. B40, 6872 (1989).
2. M. Salvato, C. Attanasio, G. Carbone, T di Luccio, S. L. Prischepa, R. Russo, L. Maritato, Physica C 316, 215 (1999).
3. M. Nose, I. Tsukuda, K. Uchinokura, Physica C313, 98 (1999).
4. Z. Z. Li, H. Rifi, A. Vaures, S. Megtert, H. Raffi, Physica C 206, 367 (1993).
5. Y. Z. Yang, L. Li, D. G. Yang, B. R. Zhao, H. Chen, C. Dong, H. J. Tao, H. T. yang, S. L. Jia, B. Yin, J. W. Li, Z. X. Zhao, Phisica C 295, 75 (1998).
6. Z. Z. Li, H. Rifi, A. Vaures, S. Megtert and H. Raffy, Phys. Rev. Lett. 72, 4033 (1994).
7. M. Ye, Y. Z. Zhang, J. F. de Marneffe, M. P. Deplancke-Ogletree and R. Deltour, Thin Solid films (2000).
8. Z. Konstantinovic, Z. Z. Li, H. Raffy, Physica C351, 163-168 (2001).
9. Y. Z. Zhang, R. Deltour, J. F. de Marneffe, Y. L. Qin, L. Li, Z. X. Zhao, A. G. Jansen and P. Wider, Phys. Rev. B61, 8675(2000).

10. Y. Z. Zhang, Y. L. Qin, R. Deltour, H. J. Tao, L. Li, Z. X. Zhao, Physica C 322, 73-78(1999) and J. Supercond. 13, 153(2000).
11. Z. Konstantinovic, Z. Z. Li, H. Raffy, Physica C 351, 163 (2001).
12. A. V. Pop, Gh. Ilonca, M. Pop, R. Deltour, Int. J. Mod. Phys. B (2002)-accepted.
13. J. A. Thornton, J. Vac. Technol. 12, 830 (1975).
14. Y. Z. Zhang, H. T. Yang, L. Li, D. G. Yang, H. J. Tao, B. R. Zhao, Z. X. Zhao, J. Mater. Sci. Lett. 16, 1095 (1997).
15. B. C. Chakoumakos, P. S. Eby, B. C. Sales, E. Sonder, J. Mater. Res. 4, 767 (1989).

STUDIA UNIVERSITATIS BABEŞ-BOLYAI, PHYSICA, XLVII, 1, 2002

THE INFLUENCE OF HEAT TREATMENT ON STRUCTURAL AND ELECTRIC PROPERTIES OF BULK (Bi,Pb):2223 SUPERCONDUCTOR

A. V. POP*, GH. ILONCA*, MARIANA POP, I. I. GERU*****

ABSTRACT. The (Bi,Pb)(Sr,Ba):2223 samples were prepared by using different sintering temperatures. The structural and phase purity was studied by X-ray diffraction and electrical properties by electrical transport measurements. The critical current density from electrical measurement agree by the results obtained from complex magnetic susceptibilities measurements as function of temperature and a. c. field amplitude. The increase of sintering temperature induce the decrease of transition width and the increase of intergranular critical current density J_{cj} and phase purity.

Introduction

The bulk sintered specimen of high – T_c superconductors shows two critical temperatures corresponding to grain (intrinsic) and coupling between grains(weak links) respectively. AC susceptibility measurements have been used to investigate the intergranular critical current density J_{cJ}, which is equivalent to the transport J_c [1,2].

In bulk materials, grain boundaries present barriers to the passage of current and acts as a weak links(structural misalignment, dirt or other impurity phases, oxygen vacancies etc) [3]. The current can pass through many different path through grain boundaries, and the bulk SC is a multiple Josephson junction array. Misalignement between grains and their boundaries causes degradation of J_c, particularly in magnetic fields.

The bulk (Bi,Pb):2223 material consists of grains weakly coupled at the grain boundaries by junctions or weak links. The quadratic temperature dependence of J_{cj} near T_c suggests SNS junctions between the grains [4,5].

---

* *Faculty of Physics,University Babes-Bolyai, 3400Cluj-Napoca, Romania*

** *Department of Plastic Deformation, Technical University, 3400 Cluj-Napoca,Romania*

*** *State University of Moldova, Superconductivity&Magnetism Laboratory, 60 Mateevici str., MD-2009, Chisinau, R. Moldova*

In disordered weak-links network of HTS ceramic samples the increasing current induces dissipation due to normal conduction first in grain boundaries as directely demonstrated by locating precisely the ‚hot spots' in spatially resolved resistivity measurements [6]. The transition in polycristalline HTS samples is interpreted as a two stage processes process: the upper part corresponds to thermodynamic intragranular transition while the lower part corresponds to intergranular coherence transition. The intra- and intergrain properties of (Bi,Pb):2223 system are different influenced by the partial substitution of copper (Cu) by 3d elements [7,8]. In this paper we report the influence of sintering temperature on the phase purity, electrical resistance and critical current density of (Bi,Pb)(Sr,Ba):2223 bulk superconductor from V-I measurements at 77K.

Experimental

Bulk samples with nominal composition $(Bi_{1.6}Pb_{0.4})(Sr_{1.8}Ba_{0.2})(Ca_{0.998}Er_{0,002})_2Cu_3O_y$ were prepared by the conventional solid-state reaction of appropriate amounts of the metal oxides and carbonates of 99. 99% purity. The partial substitution of Sr by Ba was used to induce the reduction of the modulation period [9]. Appropriate amounts of Bi_2O_3, PbO, $SrCO_3$, BaO, Ca CO_3, Er_2O_3 and CuO were mixed in agate mortar and calcined at 800 ^{0}C for 36 hours. The calcinated powder was pressed into pellets and sintered at 845 ^{0}C for 200 hours. The pellets were grinding, pressed and resintered as following: the first (named sample S1) for 60 hours at 845 ^{0}C and the second (named sample S2) for 60 hours at 850 ^{0}C.

The X-ray diffraction (XRD) analysis confirmed the presence of a majority 2223 phase in S_1 and S_2 samples.

Electrical resistance function of temperature and V-I measurements by four probe method were performed by using a Keithley 182 nanovoltmeter and a Keithley 220 current source. Silver paint were used to obtain low contact resistance (after a heat treatment at 590 ^{0}C of pasting silver paint on the sample surface).

Results and discussion

Figure 1 shows the X-ray diffraction patterns of S1 and S2 samples. For S1 sample, most of the identified peaks belong to the "2223' with a few low-intensity peaks belonging to the '2212' and"2201" phases. XRD pattern for S2 sample show that the amount of "2212" phase decrease and '2201' phase is absent.

The temperature dependencies of electrical resistance, R (T), for the samples S1 and S2 are shown in Fig. 2. Above the excess conductivity region our samples are characterized by a linear temperature dependence of electrical resistance:

$$R=R(0) + a\,T.$$

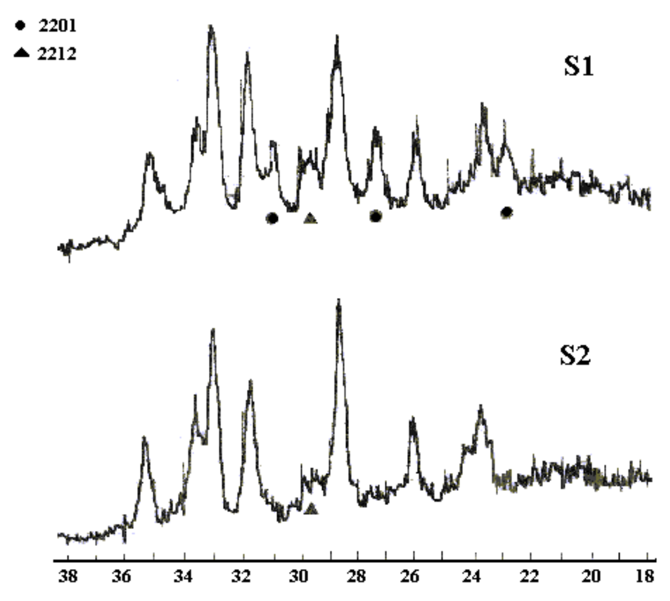

Fig. 1. *X -ray diffraction patterns of S1 and S2 samples as a function of angle 2θ. The "2212"phase are indicated by triangles and the "2201" phase by circles.*

By using the measured room temperature and the parameters R(0) and a, found by a linear regression on the data, the residual resistivity $\rho(0)$ and the temperature coefficient of the resistivity, $d\rho/dT$ were obtained (Table 1). The insert of Fig. 2 shows the broadening of resistive transition for sample S1 comparatively by S2 sample and the increase of $T_c(\rho=0)$ for S2 sample (table 1). The decrease of resistance tail for S2 sample suggest the decrease of intergrain dissipation processes.

The critical transition temperature, T_c,was obtained as the maximum observed in the first derivative dR/dT versus temperature (Fig. 3) The first derivative for S1 and S2 samples are reasonable fitted by Gauss function. By using this fit we obtain the transition width ΔT_c decrease with increasing sintering temperature (Table 1).

Table 1.

The parameters for S1 and S2 samples obtained from electrical resistance and I-V experimental data.

Sample	**T_c [K]**	**ΔT_c [K]**	**$T_c(\rho=0)$ [K]**	**$\rho(0)$ [$\mu\Omega$. cm]**	**$d\rho/dT$ [$\mu\Omega$. cm/K]**	**J_{cJ} (77K) [A/cm^2]**
S1	107. 7	4. 7	100. 0	1637	60. 9	27
S2	108. 2	3. 5	104	570	50. 1	331

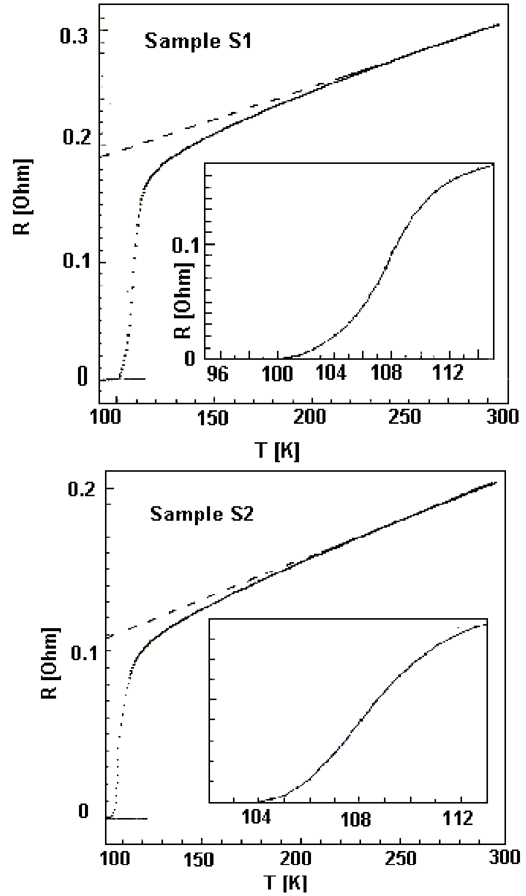

Fig. 2. *The temperature dependence of the electrical resistance for samples S1 and S2. The inserts show the transition regions.*

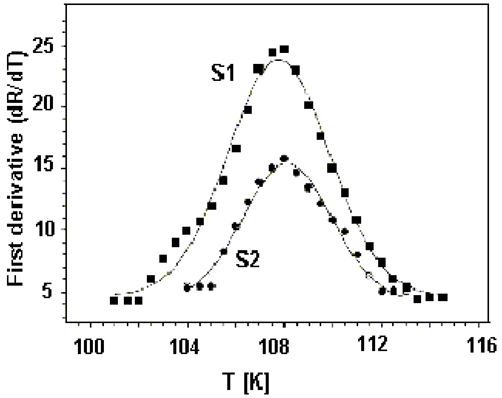

Fig. 3. *dR/dT versus temperature for samples S1 and S2. The full lines are the fits with Gauss function*

We have measured the voltage (V) as a function of current (I) for samples S_1 and S_2 sintered at 845 ^{0}C and 850 ^{0}C respectively. Fig. 4 shows for these sample the V-I characteristics at a temperature T= 77 K, much below the critical transition temperature T_c = 108. 5 K. The V(I) dependence are conventional ones for ceramic samples which have intrinsic Josephson junctions network between grains. The critical current I_c for samples S_1 and S_2 are I_{c1}= 126 mA and I_{c2} =1300 mA, respectively. The corresponding values for the the intergranular critical current density J_{cJ1}=27A/cm^2 and J_{cJ2}=331A/cm^2, evidenced that the increase of the sintered temperature by only 5 ^{0}C lead to the improvement by an order of magnitude of the conduction in intergranular junctions.

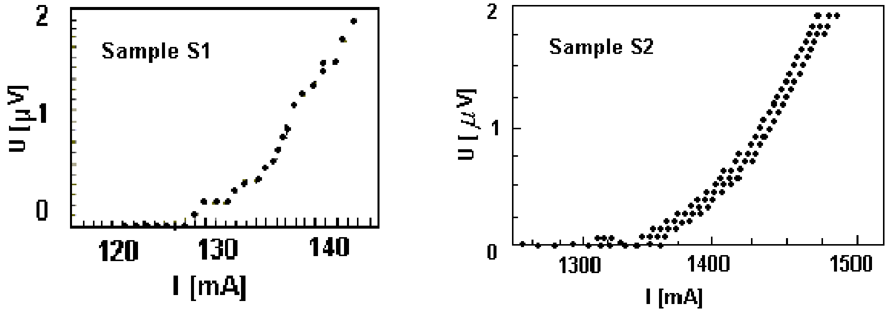

Fig. 4. *V-I plots of bulk samples S_1 (sintered at 845^{0}C) and S_2 (sintered at 850^{0}C) at the nitrogen temperture, T=77K.*

The intergranular critical current density J_{cJ} (77K) obtained from the $\chi^{''}$(T) data [10] are in agreement by the values obtained from I-V measurements (Table 1).

Conclusions

Two samples S_1 and S_2 with chemical formula $(Bi_{1.6}Pb_{0.4})(Sr_{1.8}Ba_{0.2})(Ca_{1-x}Er_x)_2Cu_3O_y$ (x = 0. 002), by majority 2223 phase were obtained by the conventional solid-state reaction by using two different sintered temperatures t_1 =845 ^{0}C (sample S1) and t_2 =850 ^{0}C (sample S2) respectively.

Traces of 2212 and 2201 were found in sample S1 and only small traces of 2212 phase in sample S2.

The temperature dependence of electrical resistance is linear above the excess conductivity region. The residual resistivity and trasition width decreases by increasing sintering temperature.

V-I measurements evidenced that the increase of the sintered temperature by only 5 ^{0}C lead to the improvement by an order of magnitude of the intergranular curerent density J_{cJ}. This result agree by the J_{cJ} obtained from a. c. susceptibility data.

REFERENCES

1. J. R. Clem, *Physica* **C153-155**, 50(1988).
2. K. -H. Müller, *Physica* **C159**, 717(1988).
3. J. Halbritter, Phys. Rev. B **48** 9735(1993).
4. D. Pandey, S. S. R. Inbanathan, P. K. Srivastava, A. Banerjee and G. Singh, Physica **C261**, 157(1996).
5. A. V. Pop, R. Deltour, A. Harabor, D. Ciurchea and Gh. Ilonca, *Int. J. Mod. Phys*. **B11**, 3461 (1997).
6. J. Manhhart, R. Gross, K. Hipler, R. P. Huebner, C. C. Tsuei, D. Dimos and P. Chaudhari, Science 245, 839 (1989).
7. A. V. Pop, Gh. Ilonca, D. Ciurchea, M. Ye, I. I. Geru, V. G. Kantser, V. Pop, M. Todica and R. Deltour, *J. Alloys and Compounds* **241**,116(1996).
8. A. V. Pop, Supercond. Sci. Technol. **12** 672 (1999).
9. H. K. Liu, S. X. Dou, N. Savvides, J. P. Zhou, N. X. Tan, A. J. Bourdillon and C. Sorrell Physica C **157,** 93, (1988).
10. V. Pop, G. Ilonca, Mariana Pop, R. Deltour, Proc. of 3rd international workshop" Materials for Electrotechnics", Bucharest, May 21-23, (2001), vol. 1, pg. 81-85.

STUDIA UNIVERSITATIS BABEŞ-BOLYAI, PHYSICA, XLVII, 1, 2002

MODEL FOR TEMPERATURE AND PROFILE DISTRIBUTION IN NONCONVENTIONAL PROCESSES OF PLASTIC DEFORMATION

MARIANA POP*, TRAIAN CANTA*

ABSTRACT. A model which had taken into account all parameters of the dieless drawing process and some elements of the process control for producing variable cross-sections are presented. With the proposed model it is possible to study the influence of various process parameters like: temperature, strain, strain rate, stress. The researches demonstrated the good agreements between the theoretical and experimental results. Also the paper present some elements of the process control for producing variable cross-sections

Introduction

In conventional metal forming processes, large plastic deformation is given to a material using tools such as dies. Some materials present much difficulties in forming because of high strengthes or poor ductilities.In most of forming processes large frictional force acts on the interface between the material and the tool, which has a negative influence in the process. To decrease the flow stress and to increase the ductility hot working is often used, but there still remain problems caused by heat resisting tools and lubricants in the high temperatures.

The non-conventional processes seem to solve these problems; are a kind of hot working and frictionless processes. Two of these processes are: dieless drawing of wires and bars and dieless bending of pipes, which present the characteristics of incremental plastic deformation processes [1,2]. A particularity of an incremental plastic deformation process is that the deformation is continuous on short parts of the semiproduct.The result of this fact is that the deformation stress, power and energy consumed in the process are lower than in the classical processes where the deformation take place in the whole volume of material.

Dieless drawing is an incremental metal forming process for plastic stretching of bars, wires, by using local induction heating. Figure 1 presents the principle of the process.

---

* *Technical University, Department of Plastic Deformation Cluj-Napoca, Romania*

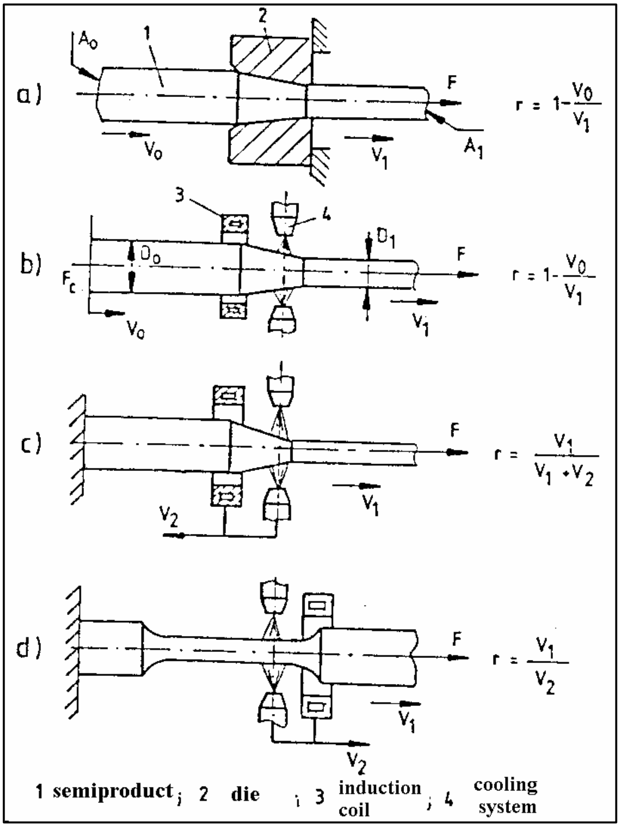

Fig. 1.

The main advantages of this process compared to the classical drawing are:

-the absence of die which makes the process less expensive compared to conventional process

-there are no intermediate heating and surface preparing operations

-absence of lubrication problems

-a large reduction of area can be obtained in a single pass(up to 80%).

The main parameters of the process can be classified into:

-control parameters: temperature, drawing force, velocity

-kinematic parameters: strain, strain rate

-material properties: density, heat conductivity, specific heat capacity

-mechanical parameters: yield stress

-disturbance parameters:inhomogeneity of material properties, changes of temperature, drawing force and velocity

A model of deformation in dieless drawing is presented in figure 2, from which result that in order to avoid the material fracture the following relation should hold in the deforming zone[3]:

$$A_0\sigma_0 = A\sigma = A_1\sigma_1 \qquad [1]$$

where A_0, A_1 are the cross sectional areas in the entrance and exit zones,
σ_0, σ_1 are the flow stress in the entrance and exit zones.

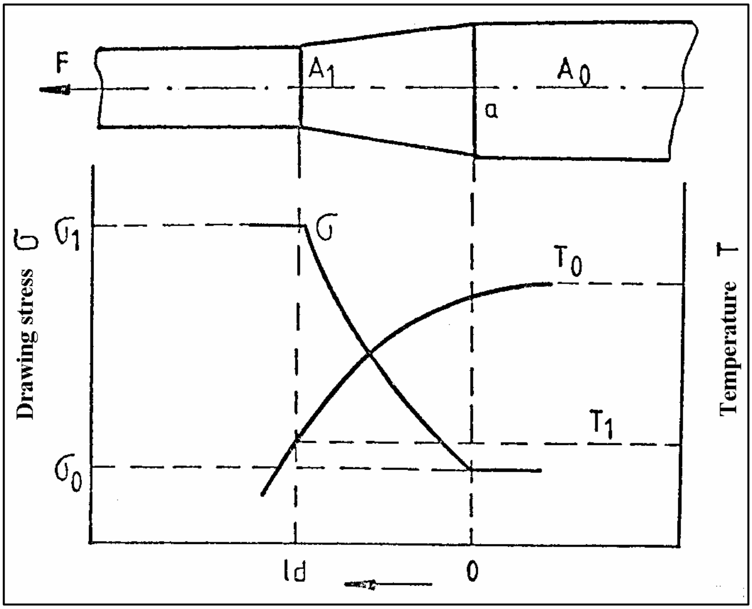

Fig. 2.

For simplicity we assume that the process is not stable when:

$$A_1\sigma_1 > A_0\,\sigma_0 \qquad [2]$$

The maximum reduction in area is:

$$r_{max} = A_{max}/A_o = 1 - A_{1min}/A_1 = 1 - \sigma_o/\sigma_1 \qquad [3]$$

The heating temperature and the cooling rate are the most important factors for the successful deformation.Induction heating is superior to any other heat method in view of the requirement for local heating, the ability to produce high heating rates and because of diminishing the phenomenos of oxidation and decarburation. In case of induction heating, the temperature of material depends on factors such as the power of the induction heating source, the shape of the induction coil, the distance between the coil and the material, and the material's physical constants(specific heat density, thermal conductivity, permeability).The cooling rate is changed by selecting the coolant. For high speed drawing liquid CO_2 can be used.

Theoretical model

For the analyze we assume that a round bar with initial radius R_0 is drawn through a fixed inductor to final radius R. Ingoing and out going speed V_0 and V_1 and also the drawing force F are constant, so that the process is in a steady state(Fig.3).The shape of the deformation zone is described by the function R=R(X). The equivalent strain is calculated with relation 4.

$$\varepsilon = \ln(\frac{A_0}{A_1}) = \ln(\frac{R_0^2}{R_1^2}) = 2\ln(\frac{R_0}{R_1}) \tag{4}$$

From relation 4 by differentiation with respect to time t, result the equivalent strain rate (5).

$$\varepsilon = \frac{d\varepsilon}{dt} = \frac{d\varepsilon}{dx}\frac{dx}{dt} = \frac{d\varepsilon}{dx}V \tag{5}$$

where V=V(x)

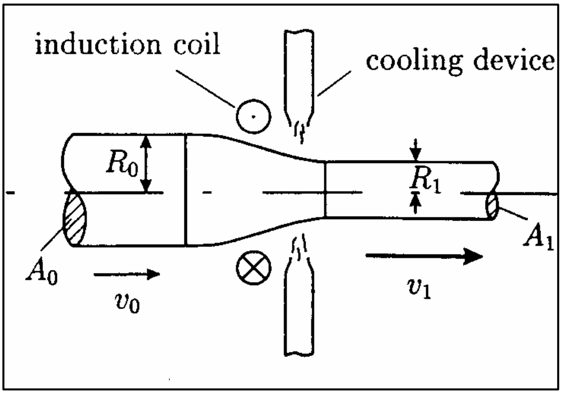

Fig. 3.

Taking into account the law of volume constancy expressed by relation 6 and with the notation $\frac{dR}{dx} = R'$ results equation 7.

$$VR^2 = V_0R_0^2 = V_1R_1^2 \tag{6}$$

$$\varepsilon = -\frac{2V_0R_0^2}{R^3}R' \tag{7}$$

As the radial component of the material flow in the deformation zone is very small compared to the longitudinal one a uniaxial stress distribution σ= σ(x) can be assume.

The force equilibrium demands that the drawing force F is constant along the bar,

$$F = \sigma_0 \pi R_0^2 = \sigma \pi R^2$$

from where result relation (8):

$$\sigma = \sigma_0 (\frac{R_0}{R})^2 \tag{8}$$

Considering the plastic deformation as a creep process [3], it can be considered the function σ = σ(T, ε, ε) as having the shape from relation 9:

$$\sigma = C e^{-m_1 T} (\varepsilon + \varepsilon_0)^{m_2} e^{m_4 / (\varepsilon + \varepsilon_0)} \varepsilon^{m_3} \tag{9}$$

where, C, m1, m2, m3, m4 are constants of material.

For numerical evaluations it is useful to solve equation 9 for R' after introducing equation 7.

$$R' = -\frac{R^3}{2V_0 R_0^2} \left\{ \frac{\sigma \exp(m_1 T)}{C(\varepsilon + \varepsilon_0)^{m_2} \exp[m_4 / (\varepsilon + \varepsilon_0)]} \right\}^{1/m_3} \tag{10}$$

In order to include the effect of large plastic deformation, we assume that the temperature T is only a function of the longitudinal coordinate x, the temperature gradient in radial direction can be neglected.

Considering a disc with infinitesimal thickness dx, cut out of the deformation zone, we can set up a balance of ingoing and outgoing heat per unit time(Fig.4).

As we have assumed steady state conditions, there is no accumulation of heat in the volume element, the temperature does not depend on time. Heat generation by plastic deformation can be neglected.

From the heat equilibrium equation on the disc result equation (11):

$$\frac{\partial^2 T}{\partial x^2} - (\frac{2}{R} tg\beta + \frac{V_0 c \rho}{\lambda} \frac{R_0^2}{R^2}) \frac{\partial T}{\partial x} - \frac{2\alpha}{\lambda R \cos\beta} T + \frac{2P}{\lambda R \cos\beta} = 0 \tag{11}$$

In case of small reductions with R≈R$_0$ we can solve equation (11) analytically in the form (12).

$$T(x) = C_1 e^{a_1 x} + C_2 e^{a_2 x} \tag{12}$$

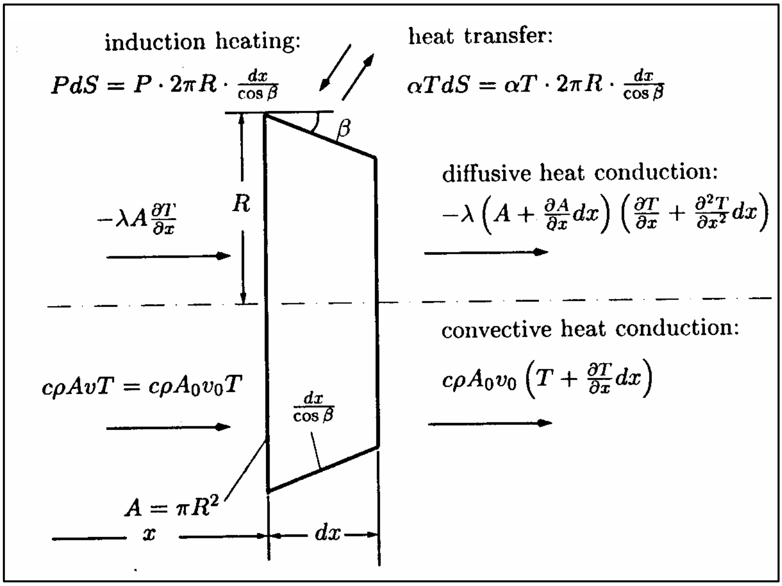

Fig. 4.

The calculation have shown that the convective part of the heat conduction, given by the drawing speed V_0, supasses the diffusive part nearly completely so it can be neglected.

$$\frac{\partial^2 T}{\partial x^2} - \frac{c\rho V_0}{\lambda}\frac{\partial T}{\partial x} \cong 0$$

The final differential equation of temperature is given by relation 13.

$$\frac{\partial T}{\partial x} + \frac{2\alpha R}{c\rho V_0 R_0^2}T - \frac{2PR}{c\rho V_0 R_0^2} = 0 \qquad (13)$$

Using the mathematical program Maple 5 were solved equations 10 and 13 and figures 5 and 6 present the results (the profiles of temperature, radius).

In the numerical example which is presented in figures 5, 6 were assumed the following stages of the process: inductive heating between $x_0=0$ and $x_1=0{,}04$m, forced air cooling between $x_2= 0{,}06$m and $x_3= 0{,}1$m, free air cooling along the rest of the bar. The numerical parameters for simulation are the following:

$P=10^8$ W/m^2, $R_0=2$ mm, $V_0= 0{,}0013$ m/s, $\sigma_0= 60$ N/mm^2, $C=1196$ N/mm^2, $\alpha_{1air}=30$W/m^{2}K,
$\alpha_{2air}= 250$ W/m^{2}K, $\rho= 7850$ kg/m^3, $c=660$ J/kg K, $m_1=0{,}0025$, $m_2= -0{,}05877$, $m_3=0{,}1165$, $m_4=-0{,}0207$

Following data were obtained for steel C45.

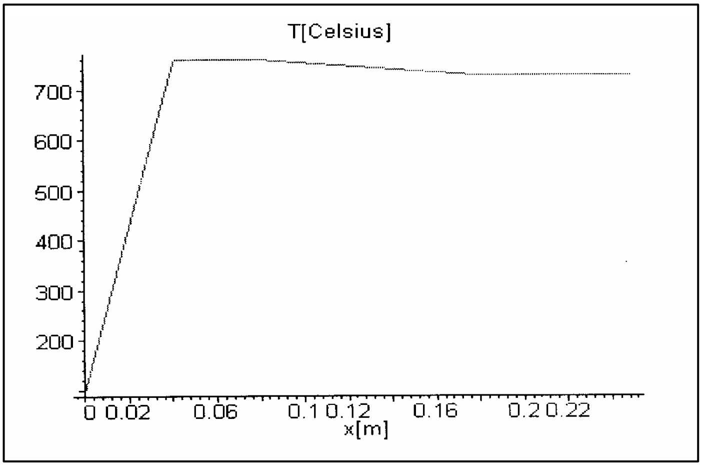

Fig. 5.

Figure 6 present the comparacy between theoretical an experimental profiles obtained for a wire with initial diameter of 4 m [4].

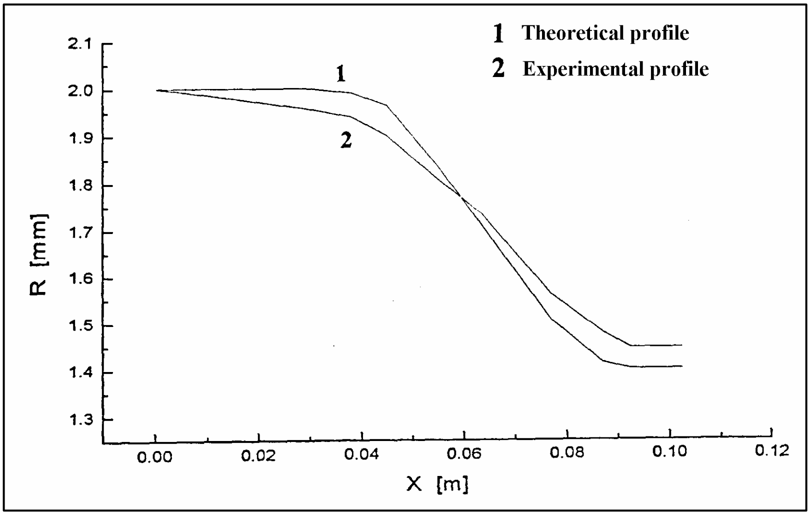

Fig. 6.

Conclusions

The theoretical model which was presented in this paper had taken into account all parameters of the dieless drawing process, that permit to obtain two differential equations for profile and temperature variations during the process.

Using the mathematical program Maple 5, were solved the differential equations and were represented the parameters of the process (profile, temperature, strain, strain rate, deformation stress).

The researches demostrated the good agrements between the theoretical and experimental results (Fig.6).

REFERENCES

[1] Pawelski, O., W. Rasp, W. Wengenroth, Investigation into processing of bars with variable cross-sections by dieless drawing, Proc. of the 6th International Conference on Technology of Plasticity, 1999.

[2] Pawelski, O., Kolling, A., calculation of the temperature distribution in dieless drawing, Steel Research, 66920, 1995.

[3] Hensel, A., Spittel, T., Kraft und Arbeitsbedarfbildsamer Formgebungsverfahren, VEB Verlag fur Grundstoffindustrie, Leipzig, 1978.

[4] Gliga, M., Canta, T., Theory and application of dieless drawing, Wire Industry, May,1999.

STUDIA UNIVERSITATIS BABEŞ-BOLYAI, PHYSICA, XLVII, 1, 2002

ELECTRON IMPACT MASS SPECTRAL STUDY OF SOME S-METHYL p-ARYLSULPHONAMIDES OF THE DIMETHYLAMIDOCYCLOHEXYLPHOSPHONIC ACID

*** SIMONA NICOARĂ[1], Z. MOLDOVAN[2], I. FENESAN[3], O. COZAR[4]**

ABSTRACT. This work deals with the analysis of the fragment ions resulted under electron impact from the molecules of the: **(1)** p-methoxybenzenesulfonimide-, **(2)** benzenesulfonimide-, **(3)** p-chlorine-benzenesulfonimide-, and **(4)** p - methylbenzenesulfonimide - of the S - methyl, N, N - dimethyl-amidocyclohexylthiophosphonic acid.

Mass spectra at 70 eV, metastable ions detection and accurate mass measurements were used to investigate the fragmentation processes.

Key words: S-methyl derivatives, electron impact mass spectrometry, fragmentation patterns

INTRODUCTION

This paper aims to elucidate the fragmentation pathways for molecules (1)-(4), the representatives of a newly synthesized class of thiophosphororganics, tested for their expected biological potential [1]. The organophosphorus compounds are widely studied and analyzed owing to their capability of biological interaction, being used as therapeutic agents, as insecticides, herbicides and fungicides [2-4].

Microorganisms have learned to develop their resistance against several pesticides, sulfonamides, or antibiotics, and thus, new compounds need to be synthesized, studied and tried against several bacteria and pests. Among other physico-chemical spectroscopic techniques, the mass spectrometry plays an increasingly important role in the structural characterisation, in the identification and the quantitative determination of different classes of pesticides [5,6].

---

[1] Physics Department, Technical University of Cluj-Napoca, C. Daicoviciu str., nr. 15, 3400 Cluj-Napoca

** author for correspondence: e-mail:* ***<simona.nicoara@personal.ro>***

[2] Mass Spectrometry Laboratory, National Institute for Research and Development on Isotopic and Molecular Technology, INCDTIM Cluj-Napoca

[3] Chemistry Institute "Raluca Ripan", Donath Street, nr. 101, Cluj-Napoca

[4] Department of Atomic, Nuclear and Environmental Physics, Faculty of Physics, "Babes-Bolyai" University, Kogălniceanu str., nr. 1, Cluj-Napoca

The compounds described here, have the following structural formula:

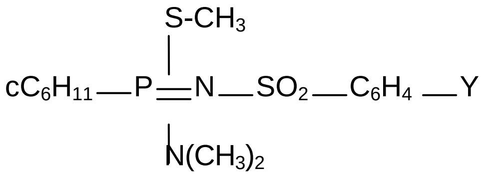

$$cC_6H_{11}-\underset{N(CH_3)_2}{\overset{S-CH_3}{P}}=N-SO_2-C_6H_4-Y$$

1. Y = OCH_3 (31 amu)
2. Y = H (1 amu)
3. Y = Cl (35 amu)
4. Y = CH_3 (15 amu).

EXPERIMENTAL

All the experimental data were recorded using a double focusing mass spectrometer MAT-311, set at the following parameters: electron energy 70 eV, electron emission 60 µA, ion source temperature 150 ^oC, and resolution R = 800 for the normal mass spectra. Few micrograms of each sample were introduced in the ion source by using the solid sample inlet system, at the optimum evaporation temperature, for each compound: 60 ^oC (**1**), 85 ^oC (**2**), 80 ^oC (**3**), and 110 ^oC (**4**).

The metastable ions transitions were analyzed in the HV mode, by scanning the accelerating voltage V, to detect the ion fragmentations in the first field free region, and in the MIKE mode respectively, by scanning the electric sector U, to identify the daughter fragments of the metastable ions that breake up in the second field free region, between the magnetic and the electric sectors [7].

Accurate mass measurements were performed through the peak matching unit, with PFK ions as mass references, at resolution R = 4000 with 10 % valley, to confirm the elemental compositions of most of the fragment ions.

RESULTS AND DISCUSSION

Figures 1-4 present the 70 eV mass spectra of the four arylsulfonimidic thiophosphonamides studied here.

The mass spectrum of compound ***(1)***, under low electron impact energy (~ 10 eV) is shown in figure 5. By comparing the spectra of the p-methoxybenzenesulfonimide of the dimethylamidocyclo-hexylthiophosphonic acid ***(1)***, in figures 1 and 5, respectively, one observes the higher abundance of heavier ions in the low energy spectrum with the base peak at m/z 374 (resulted from $M^{+\cdot}$, by the loss of a neutral NC_2H_5 molecule), unlike the pattern of the 70 eV mass spectrum, where the low mass ions have dominant abundances, and the base peak is at m/z 55, the well-known fragment $[C_4H_7]^+$, from the cyclohexyl cleavage.

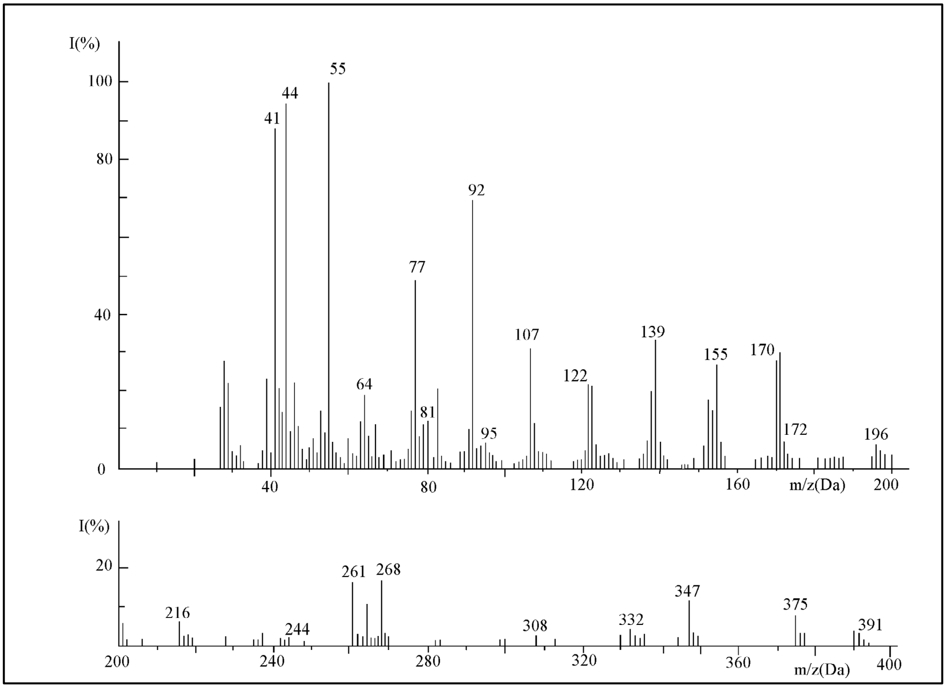

Fig. 1. *The 70 eV mass spectrum of the p-methoxybenzenesulfonimide of the dimethylamidocyclohexylthiophosphonic acid (1).*

Most of the ions were found to have correspondants in all the four spectra ***1-4****,* Table 1 contains the main fragment ions in these mass spectra. Table 2 shows some results of the accurate mass measurements, and Table 3 contains some MIKE data collected for the metastable ions detected in compound ***4***, the p-methylbenzenesulfonimide of the dimethylamidocyclohexylthiophosphonic acid.

The fragmentation patterns proposed in schemes I-III, of figures 6-8, show some characteristics due to the presence of the double bond P=N in the molecules, and also some other features specific to each radical bonded to the aryl group. One characteristic common to all four spectra is the low abundance of the molecular ions (0,5 - 3 %), that can be explained by the high degree of the molecules ramification, as found in other similar cases [8].

The ion *a*, m/z (277+Y) results from $\boldsymbol{M}^{+\cdot}$ through a four membered transition state involving the rearrangement of the hydrogen atom from the cyclohexyl to the P atom, as remarked in similar molecules [9]. The transition $\boldsymbol{M}^{+\cdot}$ --> *a* was not detected in metastable ions analysis but, the loss of a C_6H_{10} neutral molecule was reported for other thiophosphororganic compounds containing the cyclohexyl group [10-12].

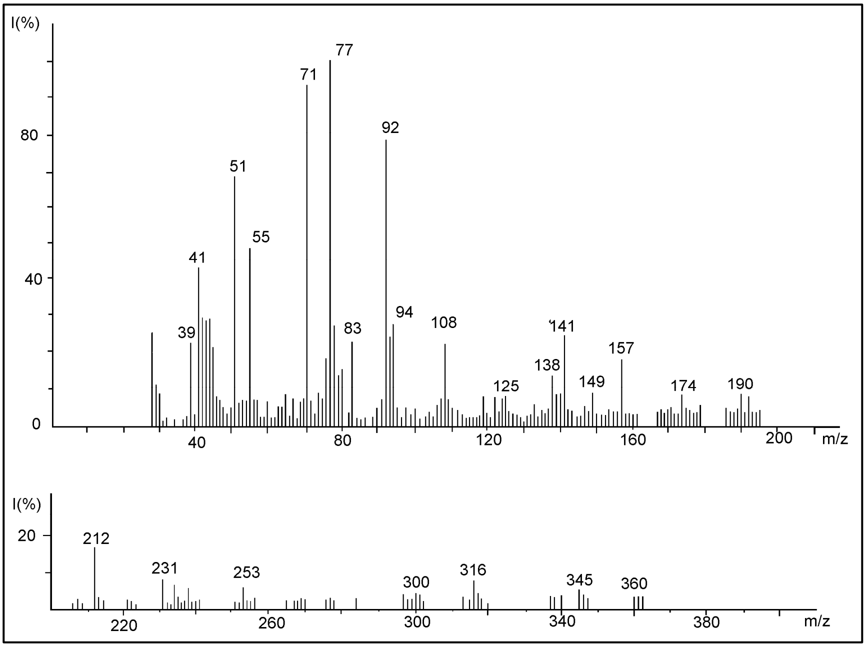

Fig. 2. *The 70 eV mass spectrum of the benzenesulfonimide of the dimethylamidocyclohexylthiophosphonic acid (**2**).*

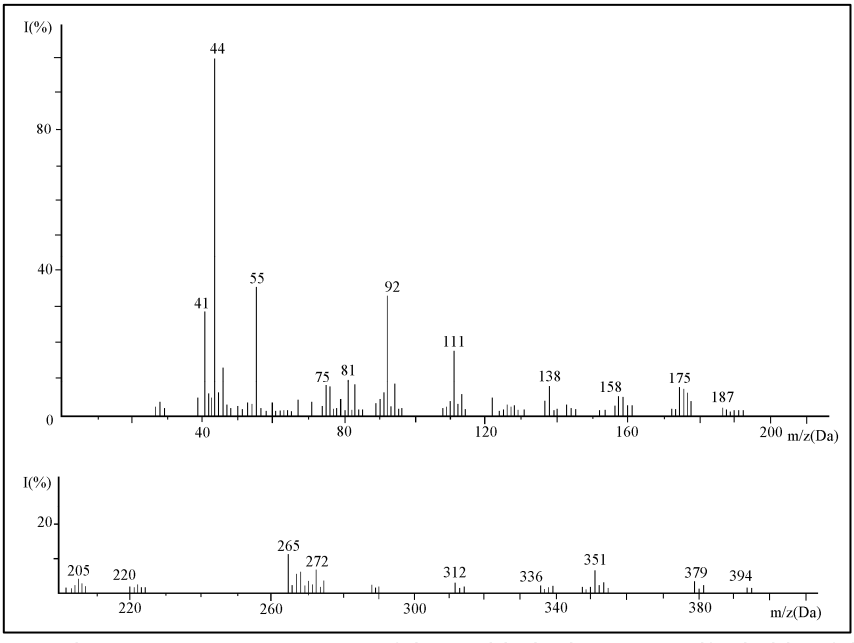

Fig. 3. *The 70 eV mass spectrum of the p-chlorinebenzenesulfonimide of the dimethylamidocyclohexylthiophosphonic acid (**3**).*

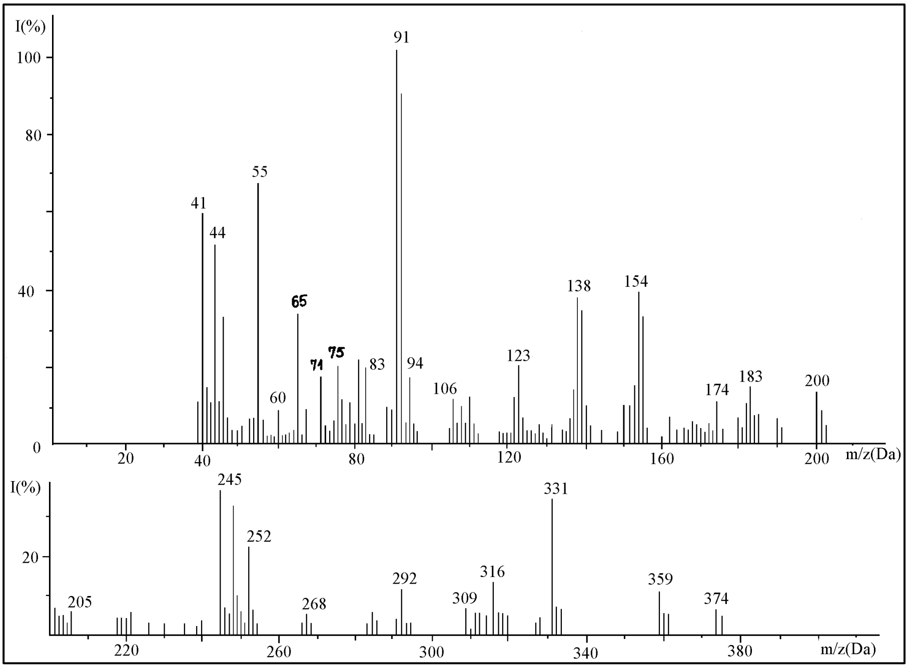

Fig. 4. *The 70 eV mass spectrum of the p-methylbenzenesulfonimide of the dimethylamidocyclohexylthiophosphonic acid (**4**).*

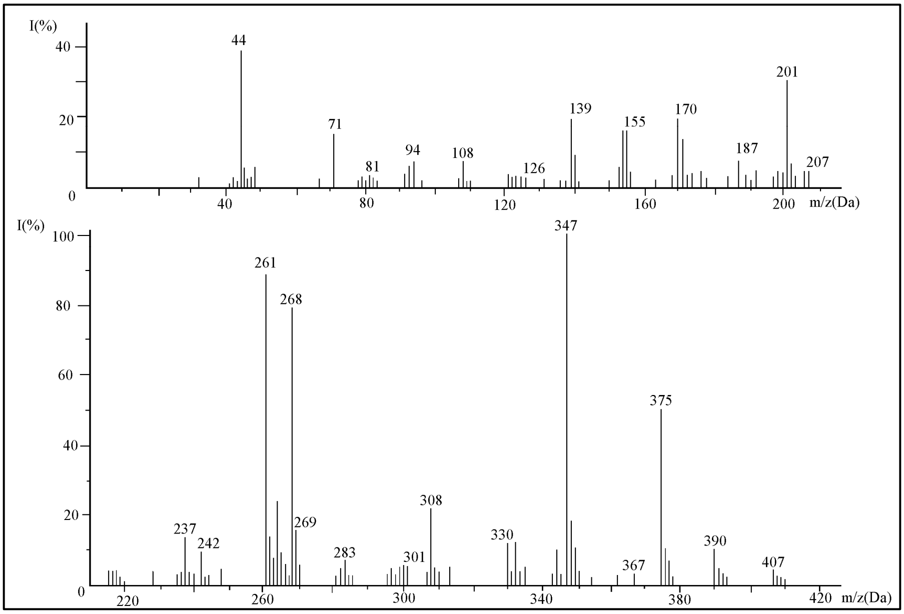

Fig. 5. *The 11 eV mass spectrum of the p-methoxybenzenesulfonimide of the dimethylamidocyclohexylthiophosphonic acid (**1**), inlet system temperature 100 ^{o}C.*

Table 1.

The main fragment ions in the 70 eV mass spectra of the compounds ***1-4*** (inlet system temperature ^{o}C), m/z (relative abundance %)

Ion	**1** (60 ^{o}C) Y=OCH$_3$	**2** (85 ^{o}C) Y = H	**3** (80 ^{o}C) Y = Cl	**4** (110 ^{o}C) Y = CH$_3$
$\mathbf{M}^{+\cdot}$	390 (1,7)	360 (1,4 %)	394 (0,8)	374 (3,0)
a (277+R)	308 (2,5)	278 (0,7)	312 (2,5)	292 (10,2)
b (233+R)	264 (10,2)	234 (6,3)	268 (5,8)	248 (32,7)
c (140+R)	171 (29)	141 (22,2)	175 (7)	155 (25)
d (154)	-	-	-	154 (28)
e (138)	-	-	-	138 (37)
f (124+R)	155 (25)	125 (7)	158 (7)	139 (33)
g (108+R)	139 (31)	109 (6)	143 (3)	123 (18)
h (107+R)	138 (19)	108 (21)	142 (0,2)	122 10)
i (186+R)	217 (3)	187 (1,4)	221 (19)	201 (6)
j (230+R)	261 (15)	231 (8)	265 (12)	245 (36,7)
k (187+R)	218 (3)	188 (1,4)	222 (2)	232 (4)
l (153)	-	-	-	153 (12)
m (185+R)	216 (3)	186 (3)	220 (2)	200 (6)
n (215+R)	246 (0,1)	216 (0,4)	250 (0,3)	230 (2)
o (313+R)	344 (1)	314 (1,5)	348 (1)	328 (3)
p (271+R)	302 (0,2)	272 (0,3)	306 (0,2)	286 (1)
q (207+R)	248 (1)	208 (2)	242 (1)	222 (1)
r (192+R)	-	193 (2)	227 (0,1)	207 (1)
s (316+R)	347 (10)	317 (2)	351 (7)	331 (33)
t (269+R)	300 (1)	270 (2)	304 (1)	284 (4)
u (252+R)	183 (1)	253 (6)	287 (1)	267 (4)
v (237+R)	268 (16)	238 (6)	272 (6)	252 (22)
w (301+R)	332 (34)	302 (2)	336 (2)	316 12)
x (253+R)	248 (1)	254 (1,4)	288 (1)	268 (2)
y (344+R)	375 (7)	345 (3,5)	379 (3,3)	359 (8)
z (312+R)	343 (0,4)	313 (1)	347 (0,4)	327 (1)
z_1 (270+R)	301 (0,2)	271 (1)	305 (1)	285 (2)
z_2 (206+R)	237 (3)	207 (2)	241 (0,3)	221 (5)
z_3 (191+R)	222 (0,2)	192 (6)	226 (1)	206 (5)

Some simple fission processes of the P-N and P-S bonds, in the ion *a*, lead to the ionic structures *b*, m/z (233+Y) and *j*, m/z (230+Y), having relatively important abundances (> 10 %) in all four spectra.

The transition *b--> c,* m/z (140+Y) was registered as the cleavage of the metastable ion *b*, through a simple fission. In molecule ***4*** , the ion *c* consequently loses the H and O atoms, respectively, to produce the ions *d*, m/z 154 and *e*, m/z 138, that involve the formation of the tropylium cycle, encountered in the cleavage of other molecules with substituted phenyl [13,14]. The structure *c* successively eliminates two oxygen atoms, as reported for other compounds containing the SO_2 group [11,15], to result in the ions *f*, m/z (124+Y) and *g*, m/z (108+Y), of higher abundance (> 20 %) in spectra **1** and **4**, probably due to the higher stability provided by the radicals CH_3 and OCH_3, respectively.

The structure *g*, may then eliminate a H atom, resulting in the double cycled ion *h*, m/z (107+Y), as reported in the literature, in other compounds with phenyl and S or O atoms [11,13].

The ion *i*, m/z (186+Y) is possibly formed from the ion *b*, by the elimination of the neutral radical SCH_3, similar losses by simple fission being reported in the literature for other phosphorodithioates [16].

Another series of abundant ions is generated from *a,* by the elimination of the SCH_3 radical, resulting the ion *j,* m/z (230+Y). The latter may also lose a methyl radical and form the ion *n*, m/z (215+Y). The metastable ions detection confirmed the transitions: *j-->k-->n*, in compound **4**, as marked in Scheme I, figure 6.

The HR mass measurements confirmed the elemental compositions of the ions involved (See Table 2) and the metastable ions analysis revealed that the ion *m*, m/z (185+Y) is generated by the elimination of the neutral molecule $HN(CH_3)_2$, from the structure j_1, m/z (230+Y), the isomer of the ion *j*, m/z (230+Y), in Scheme I, fig. 6. In the spectrum of compound ***4***, the ion structure *l*, m/z (153), with the atomic composition confirmed via HR mass measurements, results from *j*, by the loss of a C_7H_8 neutral radical, as confirmed in the metastable ions analysis. The process is not possible in molecules ***1-3****,* with other radicals, that do not have C atoms, directly bonded to the phenyl group.

In all the four spectra, there are ions at m/z (313+Y), and the accurate mass measurements suggested an elemental composition compatible with the structure *o*, m/z (313+Y), in Scheme II of figure 7. This ion is formed through a four membered transition state, involving the transfer of a H atom from SCH_3, to the P atom, and the subsequent elimination of a neutral SCH_2 molecule.

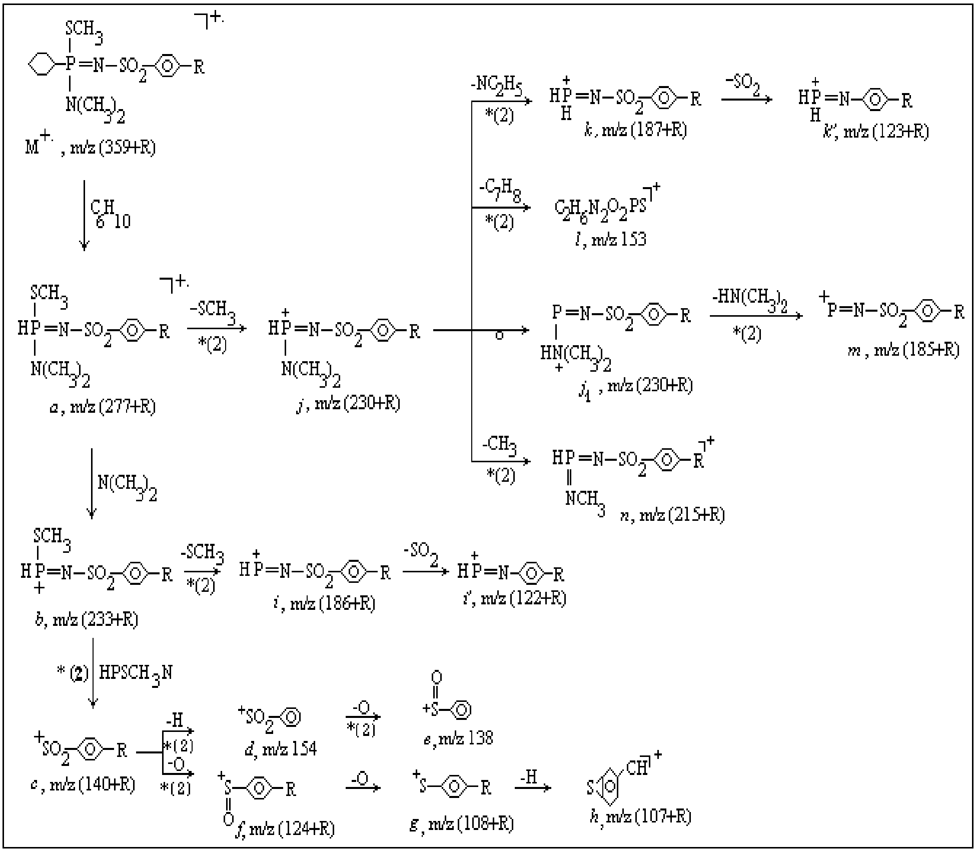

***Fig. 6.** Scheme I- Fragmentation of the S-methyl derivatives **1-4**, starting with the elimination of the C_6H_{10} neutral molecule. Includes the ions labelled a-n.*

Table 2.

Accurate masses of some fragment ions in the spectrum of the p-methylbenzene-sulfonimide of the dimethylamidocyclo-hexylthiophosphonic acid (**4**).

m/z	formula	theoretical mass	measured mass	abs. error
(Da)	-	amu	amu	10^{-3} amu
316	$C_{13}H_{19}NO_2PS_2$	316,05946	316,05975	0,3
292	$C_{10}H_{17}N_2O_2PS_2$	292,04688	292,04784	0,96
267	$C_{14}H_{22}NPS$	267,12105	267,11261	8,44
252	$C_{13}H_{19}NPS$	252,09757	252,09806	0,49
248	$C_8H_{11}NO_2PS_2$	247,99686	247,9969	0,04
245	$C_9H_{14}N_2O_2PS$	245,05134	245,04951	1,83
221	$C_{12}H_{18}N_2P$	221,12073	221,13078	10,05
155	$C_2H_8N_2O_2PS$	155,0044	155,0167	12,3
139	$C_2H_8N_2OPS$	139,0207	139,0207	11,2
92	C_2H_6NSO	92,01701	92,02507	8,06
75	C_2H_5NS	75,01427	75,02289	8,62

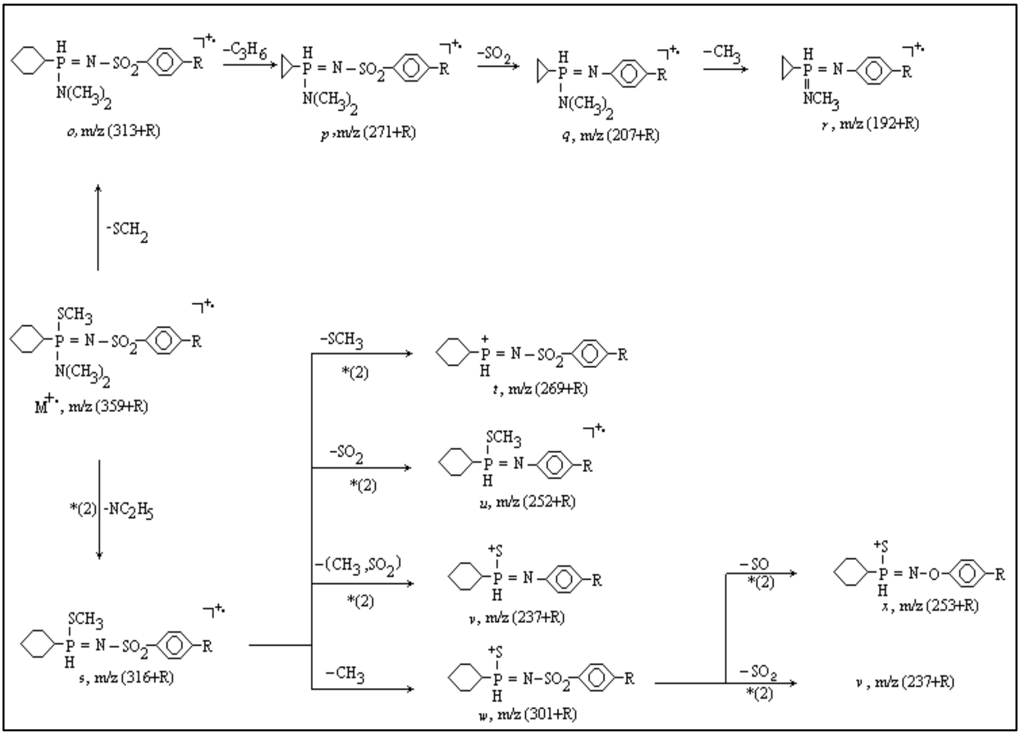

Fig. 7. *Scheme II- Fragmentation of the S-methyl derivatives, including the ions containing the cyclohexyl group (labelled o-w).*

The ion *o* may further undergo the cleavage of the cyclohexyl group, eliminating a neutral C_3H_6 molecule, and resulting the ion *p*, m/z (271+Y), that involves the ring contraction, as reported in other cases of molecules having cyclic structures [8,11,13].

The ion *p* possibly loses the neutral SO_2 molecule, to generate the ion *q,* m/z (207+Y), which subsequently eliminates one of the methyl radicals bonded to the N atom, and results the ion *r*, m/z (192+Y).

A series of relatively abundant ions (5-38 %) rise at *s,* m/z (316+Y), formed from the ion $\mathbf{M}^{+\cdot}$ through a four membered transition state, involving the transfer of a H atom, from the dimethyl-amido group to the P atom, subsequently losing the neutral molecule NC_2H_5, the transition being detected as a metastable ion cleavage.

The simple fission of the ion s may yield the ions *t,* m/z (269+Y) and *w*, m/z (301+Y), by the elimination of either the SCH_3 or the CH_3 radicals, respectively. The same ion *s*, may also generate the ion *u*, m/z (252+Y), through a three membered transition state, involving the loss of the SO_2 neutral molecule, a process that is typical for molecules containing SO_2 and the phenyl group [11,17].

Table 3.
Experimental data concerning the metastable ions detection in compound **4.,** in the MIKE mode, by scanning the electric sector voltage.

m_1/z (precursor ion)	**U_0**	**U_1**	**m_2/z (daughter ion)**
(Da)	(V)	(V)	(Da)
374	500,7	481,2	359
		443,5	331
		390,6	292
359	500,8	480,9	345
		442,7	316
		390,0	279
		288,1	206
331	500,8	478,5	316
		404,3	267
		380,7	252
316	493,6	395,4	252
		479,3	301
j, m/z 245	493,3	462,9	230
		434,3	216
		496,5	201
		306,9	152

The metastable ions analysis in compound **4**, indicated that the ion *v*, m/z (237+Y) results from the ion *s*, m/z 331, a process that involves the simultaneous elimination of the two neutral fragments CH_3 and SO_2. The ion *v* is fairly abundant (4-22 %) in all spectra. Other cases of simultaneous elimination of several small neutral fragments from heteroatomic organic molecules are reported in the literature [11,18].

The metastable ions spectra also indicated that the ion w eliminates the neutral molecule of sulfur monoxide SO, to generate the ion *x*, m/z (253+Y), through a cleavage encountered in other molecules containing the SO_2 group [9,11,19]. Another ion of rather low (>3 %) abundance in all spectra, is *y*, m/z (344+Y), formed from the molecular ion $M^{+\cdot}$ by the simple fission of the C-S bond, and the loss of the CH_3 neutral radical from the S-methyl substitute, as presented in figure 8 - Scheme III. The metastable ions analysis revealed that the ion y undergoes the H rearrangement onto P and it further eliminates the neutral molecule NC_2H_5, to generate the ion w, m/z (301+Y), whose elemental composition was confirmed via HR mass measurements (Table 2). The ions *z,* m/z (312+Y), z_1, m/z (270+Y), z_2, m/z (206+Y), and z_3, m/z (191+Y) can be observed in all the spectra of the four S-methyl derivatives. Although the metastable ions analysis could not be performed, owing to their low abundance (~ 2 %), we suppose that they are generated from $M^{+\cdot}$ by the subsequent losses of the SCH_3, C_3H_6, SO_2 and CH_3 neutral fragments.

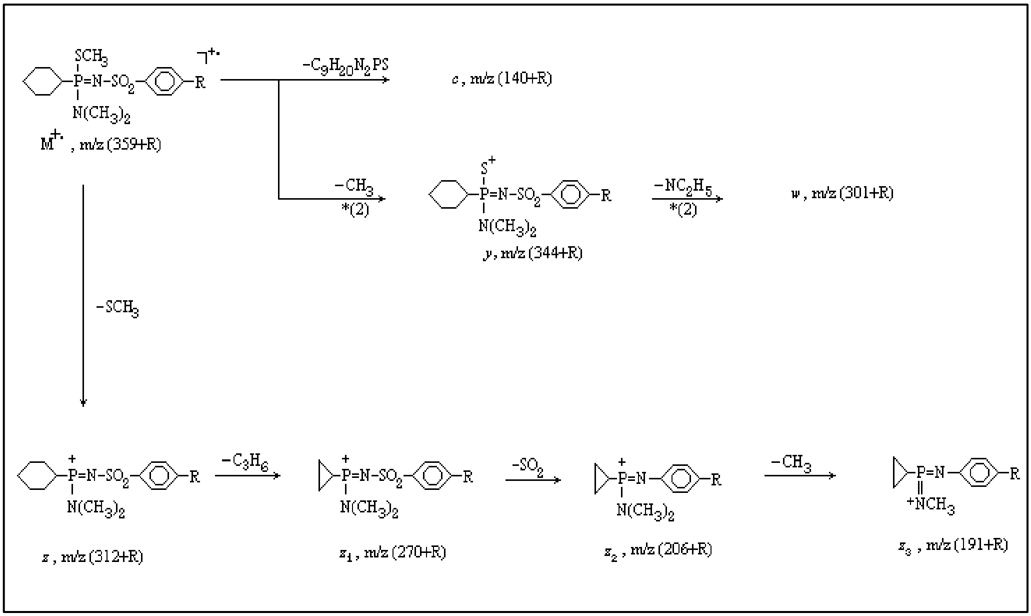

Fig. 8. *Scheme III - Fragmentation pathways of the S-methyl derivatives* ***1-4****, starting with the cleavage of the S-C bond.*

The loss of the C_3H_6 group from the ion z is followed by the cyclohexyl ring contraction, as reported for other similar molecular structures, under electron impact [8,11,13].

All the four 70 eV mass spectra contain the abundant ion (> 30 % relative intensity) at m/z (76+Y), and the accurate mass measurements confirmed for this ion the structure C_6H_4-CH_3 (here, with Y = CH_3). The ion at m/z (76+Y) is probably formed from the molecular ion $\boldsymbol{M^{+\cdot}}$, by the simple fission of the S-C bond, between the SO_2 and the phenyl groups. This ion gives the base peaks in spectra ***2*** and ***4****,* and has an important abundance (> 30 %) in spectra ***1*** and ***3****,* due to the stability of the aromatic cycle.

Another intense (> 30 %) peak is recorded in all the spectra at m/z 92, whose elemental composition $(CH_3)_2NSO$ was confirmed through HR mass measurements (see table 2). The formation of this ion involves the migration of some groups of atoms, a process encountered in other thiophosphororganic compounds and in derivatives whose molecules contain the $N(CH_3)_2$ group [20,21].

The fairly abundant (>15 %) ion at m/z 75 in all the spectra, except for compound ***4****,* has the elemental composition C_2H_5NS, confirmed by accurate mass measurements, and may be formed from the ion recorded at m/z 92, by the elimination of a neutral OH radical. The process was not detected as the transition of a metastable ion, but the loss of an OH group was previously reported in molecules with O and H atoms, the oxygen being bonded to a carbonyl group and not directly to H [22-24].

The peak at m/z 44, intense in all the spectra (30 %), and also the base peak in spectrum 3, is given by the ion $N(CH3)_2$, whose elemental composition was confirmed in HR mass measurements. Similar thiophosphororganics, their molecules containing the $N(CH_3)_2$ radical, gave abundant peaks at m/z 44 [10].

The series of ralatively abundant ions at m/z 83, 55 and 41 are charcateristic to the cyclohexyl ring cleavage [10].

Conclusions

The mass spectra of the four S-methyl derivatives discussed here contain numerous fragment ions formed by the simple bonds fission, with the elimination of the neutral atoms or radicals: O, H, OH, CH_3, SCH_3, $N(CH_3)_2$.

Other ions were also recorded, whose generation involved the rearrangement of H or of several atoms, with the subsequent elimination of neutral molecules such as: SCH_2, NC_2H_5, $HN(CH_3)_2$, C_6H_{10}, C_3H_6, SO, SO_2.

REFERENCES

1. Rodica Popescu, Viorica Muresan, I. Fenesan, A. Hantz, V. Chioreanu - unpublished data.
2. C. T. Supuran, V. Muresan, R. Popescu, I. Fenesan, *Main Group Metal Chemistry*, vol. **18**, nr. 11 (1995) 629.
3. C. Fest and K. J. Schmidt: "The Chemistry of Organic Pesticides", Springer Verlag, Berlin (1973).
4. P. Wieczorek and D. Miliszkiewicz, *Pestic. Sci.*, **40** (1994) 57.
5. S. Safe and O. Hutzinger: "Mass Spectrometry of Pesticides and pollutants", CRC Press Clevelenad (1976).
6. K. Biemann: "Mass Spectrometry Organic Chemistry Applications", Mc-Graw-Hill, New-York (1962).
7. Z. Moldovan, N. Palibroda, V. Mercea and G. Mihăilescu, *Org. Mass Spectrom*., **20**, 2 (1985) 77.
8. M.C. Hamming and N.C. Foster: "Interpretation of Spectra of Organic Compounds", Academic Press, New-York (1972).
9. J. Seibl: "MassenSpektrometrie", Akademische Verlagsgesellschaft, Frankfurt-am-Main (1970).

10. Simona Nicoară, Monica Culea, N. Palibroda, O. Cozar, I. Fenesan, A. Hantz, *Rapid Commun. Mass Spectrom.*, **9** (1995) 61.
11. Z. Moldovan, N. Palibroda, Monica Culea, I. Fenesan, A. Hantz, *Org. Mass Spectrom.*, **24** (1989) 81.
12. Z. Moldovan, Simona Nicoara, Monica Culea, I. Fenesan, O. Cozar, P. Vegh and J. J. Rios, *J. Molec. Struct.*, **348** (1995) 393.
13. Q. N. Porter and J. Baldas: "Mass Spectrometry of Heterocyclic Compounds", Wiley-Interscience, New-York (1971).
14. I. Lengyel, F. D. Greene and J. F. Pazos, *Org. Mass Spectrom.*, **15** (1970) 412.
15. A. Venema, N. M. Nibering and Th. de Boer, *Org. Mass Spectrom.*, **3** (1970) 623.
16. M. Medved, *Rapid Commun. Mass Spectrom.*, **5** (1991) 11.
17. I. Opreanu: "Spectrometria de masă a compusilor organici", Ed. Dacia, Cluj (1973).
18. M. Lozynsky and E. Kryzanovska, *Org. Mass Spectrom.*, **21** (1986) 33.
19. I. Fenesan, R. Popescu, C. T. Supuran, Simona Nicoara, Monica Culea, N. Palibroda, Z. Moldovan and O. Cozar, *Rapid Commun. Mass Spectrom.*, **15** (2001) 721.
20. E. Almasi: "Les composees thiophosphororganiques", Ed. Masson, Paris (1976).
21. G. Giordano, G. Peterson, W. Y. McMurray, K. Shyam and A. C. Sartorelli, *Biol. Mass Spectrom.*, **20** (1991) 693.
22. E. J. Griffith and M. Grayson: "Topics in Phosphorus Chemistry", Wiley-Interscience, New-York (1976).
23. S. N. Sawhney, S. Bhutani and D. Vir, *Org. Mass Spectrom.*, **22** (1987) 447.
24. E. D. Mitchel and G. R. Waller, *Organic Mass Spectrom.*, **3** (1970) 519.

STUDIA UNIVERSITATIS BABEŞ-BOLYAI, PHYSICA, XLVII, 1, 2002

METASTABLE ION STUDIES IN THE CHARACTERISATION OF SOME p-X SUBSTITUTED ARYLSULFONAMIDES OF THE O,O-DIPHENYLTHIOPHOSPHORIC ACID

*** SIMONA NICOARĂ[1], Z. MOLDOVAN[2], N. PALIBRODA[2], M. CULEA[2], I. FENESAN[3], R. POPESCU[3], C. BELE[4]**

ABSTRACT. The paper presents the fragmentation pattern proposed for the p-carboxybenzenesulfonamide *(**1**)*, p-carboxy-methyl-benzenesulfonamide *(**2**)*, p-methoxybenzenesulfonamide *(**3**)*, and p-fluorinebenzenesulfonamide *(**4**)* of the O,O - diphenylthiophosphoric acid.

The molecules behaviour under 70 eV electron impact was investigated based on their normal mass spectra, the accurate mass measurements and the metastable ions fragmentations. The kinetic energy release T_{50} was determined in the MIKE mode for the cleavages recorded in the second field free region, for compound ***1***, and the qualitative correlation is discussed, concerning the peak shapes, the amount of energy released, and the mechanism of decomposition proposed.

Key words: arylsulfonamides of the diphenoxythiophosphoric acid, mass spectra, metastable ions fragmentation, kinetic energy release

Short title: *Metastable* ions fragmentation in diphenoxy-thiophosphoric sulfonamides

Introduction

Many studies are focused on the physico-chemical characteristics of organophosphorus compounds, as well as on their biological properties, being used as chemosterilants, antiviral, antimicrobial, or other therapeutic agents, and as pesticides [1-5].

The purpose of this paper is to present and interprete the mass spectral data of the four arylsulfonamides of the diphenoxythiophosphoric acid, through a qualitative analysis. The discussion is based on the mechanism

---

[1] Physics Department, Technical University of Cluj-Napoca, C. Daicoviciu str., nr. 15, 3400 Cluj-Napoca
** author for correspondence: simona.nicoara@personal.ro*
[2] Mass Spectrometry Laboratory, National Insitute for Research and Development on Isotopic and Molecular Technology, Donath str., nr. 107-109, 3400 Cluj-Napoca
[3] Institute of Chemistry "Raluca Ripan", Donath str., nr. 103, 3400 Cluj-Napoca
[4] Biochemistry Department, University of Agricultural Sciences and Veterinary Medicine, Cluj-Napoca

proposed in the fragmentation pattern, related to the amount of kinetic energy released during the cleavage, and by examining the MIKE peak shape.

These compounds were synthesized at the Chemistry Institute "Raluca Ripan" [6,7]. Their MS [8], IR and NMR spectra combined with potentiometric data [6,7,9] confirmed the following chemical structure:

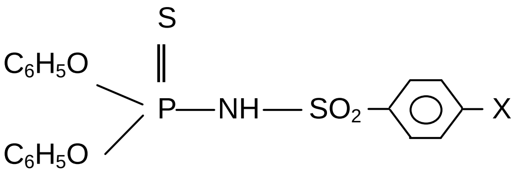

1. X = COOH
2. X = $COOCH_3$
3. X = OCH_3
4. X = F

Structural characterisation and quantitative determination of organophosphorus compounds in different biological or environmental matrices can be performed by means of mass spectrometry (MS), possibly coupled to gas- (GC) or liquid-chromatography (LC) [10-12]. The MS technique also allows the measurement of the energy released T, in the translation of the ionic and neutral fragments of organic molecules, under electron impact. These determinations are helpful in ion structure studies, since they provide information on the energetics and on the ion fragmentation mechanisms [13-15].

The kinetic energy release may originate in the excess energy of the activated complex, E^{++} (non-fixed energy) , and in the reverse critical energy E_o^r, their contributions to the total kinetic energy being T^{++} and T^r respectively: $T = T^{++} + T^r$ (See the energy diagram of fig. 1).

When the activated complex undergoes rearrangements of atoms and the reaction products are very stable ions and molecules, then the amount of E_o^r is substantial, and T^r it is most likely the dominant term in T [13,14]. Simple fission reactions are expected to have small or even no reverse reaction energy E_o^r, and therefore T^{++} is supposed to have a dominant role in T. The metastable ions generally have small internal energies, and the fissions controlled by the statistical partitioning of the excess energy E^{++} involve a small kinetic energy release T, that is mostly due to $T^{++} \cong T$ [13,14].

The amount of kinetic energy release is also dependent on the mechanism(s) that drive the fission reaction (simple fission, rearrangement reaction, Mc Lafferty transposition, isomerisation, cyclisation, ring contraction, etc.), and a correlation can be found with the metastable peak shape [14].

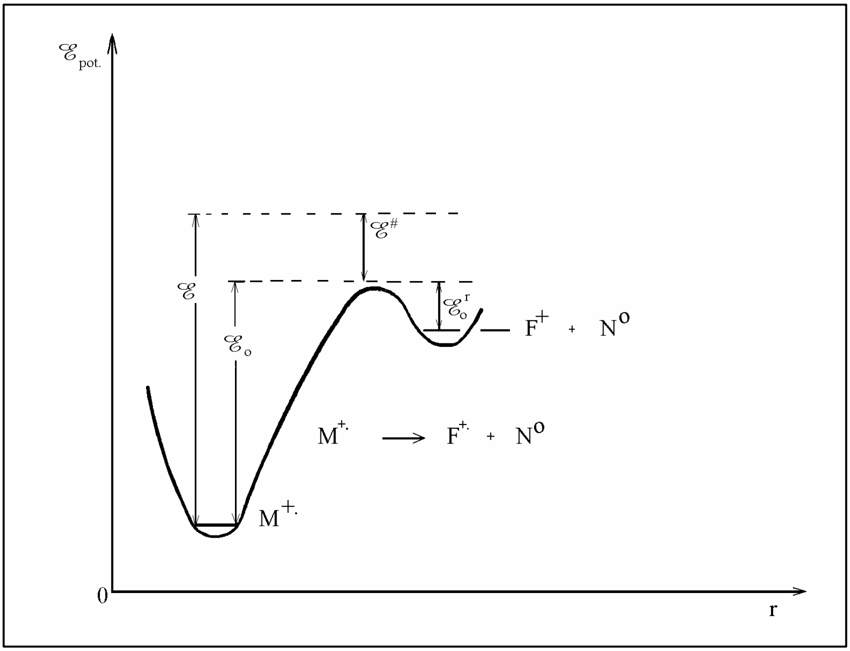

Fig. 1. *Potential energy diagram, versus the reaction coordinate: $M^{+\cdot}$, $F^{+\cdot}$, and N = parent ion, daughter ion, and neutral fragment; E= internal energy of $M^{+\cdot}$, E^{++}= excess energy of the activated complex, E_o^r = reverse reaction energy, and E_0 = direct reaction critical energy.*

A Gaussian peak, with the squared ratio of the *average* (peak width at 22 % height) to the *most probable* energy release(width at 61 % height), $r = (w_{22} / w_{61})^2$, equal to ***3*** indicates a reaction controlled by the statistical partitioning of the excess energy E^{++} in the activated complex. If, on the other hand, the reverse activation energy E_o^r is the dominant source of the translational energy release, and if the fraction of it converted to T^r covers only a reduced range of values, the metastable peak shape is not pure Gaussian, the **r** values being smaller than ***3****.* Previous studies showed that T^{++} is important only for relatively small values of the total kinetic energy release T [16,17].

EXPERIMENTAL

The mass spectrometry experimental measurements were made using a VARIAN-MAT 311 double focusing mass spectrometer with inverse Nier-Johnson geometry, equiped with a computerized system of data aquisition and processing. Standard operating conditions were as follows: 70 eV electron impact energy, 100 µA electronic current, 150 °C ion source temperature, and R=800 resolution in normal mass spectra. The solid sample inlet system was used and maintained at the optimum evaporation temperatures for each of the four compounds: 200 ^{o}C *(**1**),* 220 ^{o}C *(**2**),* 150 ^{o}C *(**3**),* and 120 ^{o}C *(**4**).* The majority of the fragment ion elemental compositions were tested by accurate mass measurements by the peak matching method, with PFK ions for reference, resolution R= 4500, valley definition 10 %, in high resolution spectra.

The metatsable ions were recorded in HV and MIKE mode. The accelerating voltage was scanned from 2000 V (divised 1:300, about 6,6 V) up to 3000 V (divised 1:300, about 10 V), to detect the fragmentation processes in the first field free region [13,14]. The electric sector voltage was decreased from about 505 V down to 0, allowing the detection of the daughter ions resulted in the second field free region [13,14]. In slow scanning of the electric sector voltage (0,35 V/s), the peak width at 50 % height was used to determine the kinetic energy release T_{50}. The MIKE mode was preferred for the energetic analysis, because of the technical limitations in HV scanning, caused by the rapid de-focusing of the ion beam, resulting in a poor signal.

RESULTS AND INTERPRETATION

The 70 eV mass spectrum of the p-carboxybenzenesulfonylamide of the O,O - diphenylthiophosphoric acid *(**1**)* is shown in figure 2. Table 1 contains the most remarkable ions, exhibiting abundant peaks in all the four spectra.

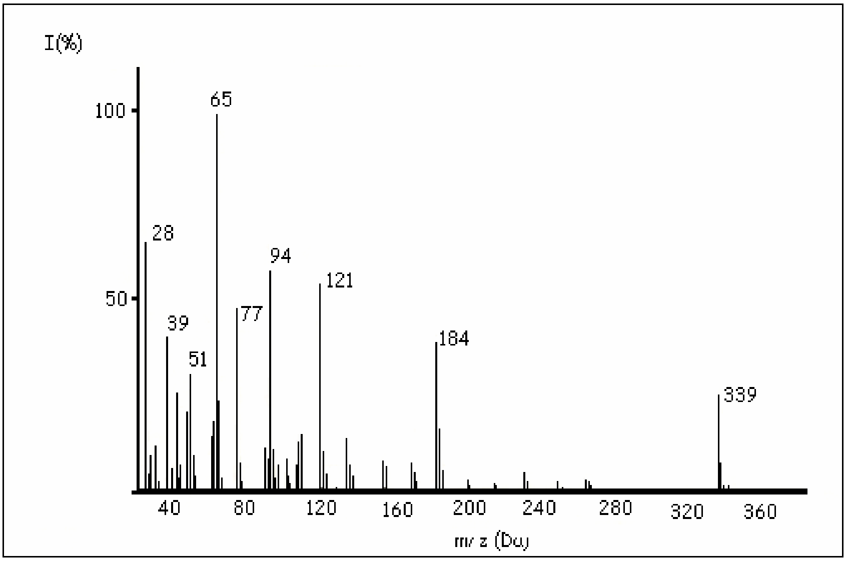

Fig. 2. *The 70 eV EI mass spectrum of the p-carboxyphenylsulfonamide of the O,O - diphenylthiophosphoric acid (**1**).*

The MIKE data recorded for the p-carboxybenzenesulfonamide of the O,O - diphenylthiophosphoric acid (**1**), in slow scanning of the electric sector voltage, are given in Table 2. The kinetic energy release, in Joules, was calculated as the average of three determinations of T_{50}, by using the relationship [13]:

$$T_{50} = \frac{y^2}{z} \cdot \frac{m_1^{\ 2}}{m_2 m_3} \cdot \frac{e \cdot V}{16} \cdot \left(\frac{\Delta U}{U_0} \right)^2 \quad \text{(J)} \qquad (1)$$

Table 1.

The main ions recorded in spectra ***1-4.*** Compound, molecular mass (inlet temperature), m/z (abundance %)

Ion, general formula	**1** (200 °C)	**2** (220 °C)	**3** (150 °C)	**4** (120 °C)
M, m/z (404+X)	449 (-)	463 (-)	435 (5)	423 (18)
$[M-SO_2]^+$	385 (-)	399 (21)	371 (50)	359 (-)
a (294+X)	339 (25)	353 (100)	325 (56)	313 (61)
b (76+X)	121 (53,4)	135 (86,2)	107 (73)	95 (100)
c (65)	65 100)	65 (52)	65 (27)	65 (53)
d (93	93 (7)	93 (6)	93 (8)	-
e (139+X)	184 (42)	198 (95)	170 (63)	158 (35)
f (156)	156 (7)	156 (8,6)	156 (5)	156 (9)
g (92)	92 (12)	92 (15)	92 (45)	92 (15)
h (94)	94 (61)	94 (67)	94 (24)	94 (53)
i(66)	66 (23)	66 (17)	66 (12)	66 (25)
j (76)	76 (17)	76 (28)	76 (10)	76 (25)
k (77)	77 (48)	77 (83)	77 (100)	77 (63)
Base peak	65 (100)	353 (100)	77 (100)	95 (100)

[Note - the X group in each compound: X= COOH (**1**); X = $COOCH_3$ (**2**); X = OCH_3 (**3**); X = F (**4**).]

where: y and z are the numbers of positive charges on the daughter and parent ions, respectively, m_1, m_2, and m_3 are the nominal masses of the ions, and of the neutral structure eliminated, e = elementary charge, V = 2970 V = accurate value of the accelerating voltage, ΔU = the peak width at 50 % height, in Volts, and U_o = the voltage of the electric sector, when the spectrometer was tuned on the parent ion.

With an average rate of 0,174 V/mm, by using the peak width in mm, the kinetic energy release in meV, was [14,18]:

$$T = 5{,}62 \cdot \frac{m_1^{\,2}}{m_2 m_3} \cdot \left(\frac{w_c}{U_o} \right)^2 \qquad \text{(meV)} \tag{2}$$

The measured metastable peak widths (w_{50}) needed to be corrected (w_c) for the kinetic energy distribution in the main ion beam (w_o = the main ion beam peak width, at 50 % height), and with respect to the different masses of the daughter and parent ions [14]:

$$w_c = \sqrt{w_{50} - \left(\frac{m_2}{m_1} \cdot w_0 \right)^2} \qquad \text{(mm)} \tag{3}$$

The method gave results in a good agreement with rigorous deconvolution methods, except for very narrow peaks [20], and was already applied to the fission of the methyl-, ethyl-, and propyl-pivaloyl- acetates [14], the kinetic energy values, being consistent with data found in the literature. The values obtained for the p-carboxybenzenesulfonamide of the diphenoxythiophosphoric acid ***(1)**,* the representative of molecules ***1-4**,* analyzed in this paper, are presented in Table 2. The last column contains the average values of the coefficient r, calculated as $r=(w_{22}/w_{61})^2$, the squared ratio between the peak widths at 22 % and 61 % of height, reflecting the energy distribution function *n(T)* [14,16,19].

Table 2.

Experimental data found by MIKE scanning of the metastable ions, in the p-carboxybenzenesulfonamide of the diphenoxythiophosphoric acid ***(1)**.*
U_0 = 504,4 V, accurately measured voltage for the main ion beam.

m_1/z (Da)	U (V)	m_2/z (Da)	<T>± σ[a]	<r> [b]
184	331,5	121	40,4±4	3,8
339	273,7	184	25,3±1,8	3,0
339	179,2	121	30,3±2,1	3,6
121	389,3	93	32,0±0,9	3,6

[a] σ = standard deviation of T, calculated for 3-4 repeated measurements
[b] $r = (w_{22}/w_{61})^2$, coefficient associated with the energy distribution function, n(T).

The fragmentation pattern proposed for the four compounds is shown in figure 3. The cleavage reactions were sustained by metastable ions detection, the fragment ions elemental composition was confirmed via accurate mass measurements, the detailed discussion of the fragmentation processes is given elsewhere [8].

The molecular ion ***M***$^{+\cdot}$ in compound *(**1**)* is very likely to undergo the thion-thiol isomerisation, prior to lose the neutral molecule C_6H_5SH, producing the ion *a*, m/z (294+X), with a quite stable structure, involving an additional cycle, formed on the heteroatoms O and P. The process was not detected as a metastable ion cleavage, but it was previously encountered in other O,O-diphenylthiophosphoric compounds [21].

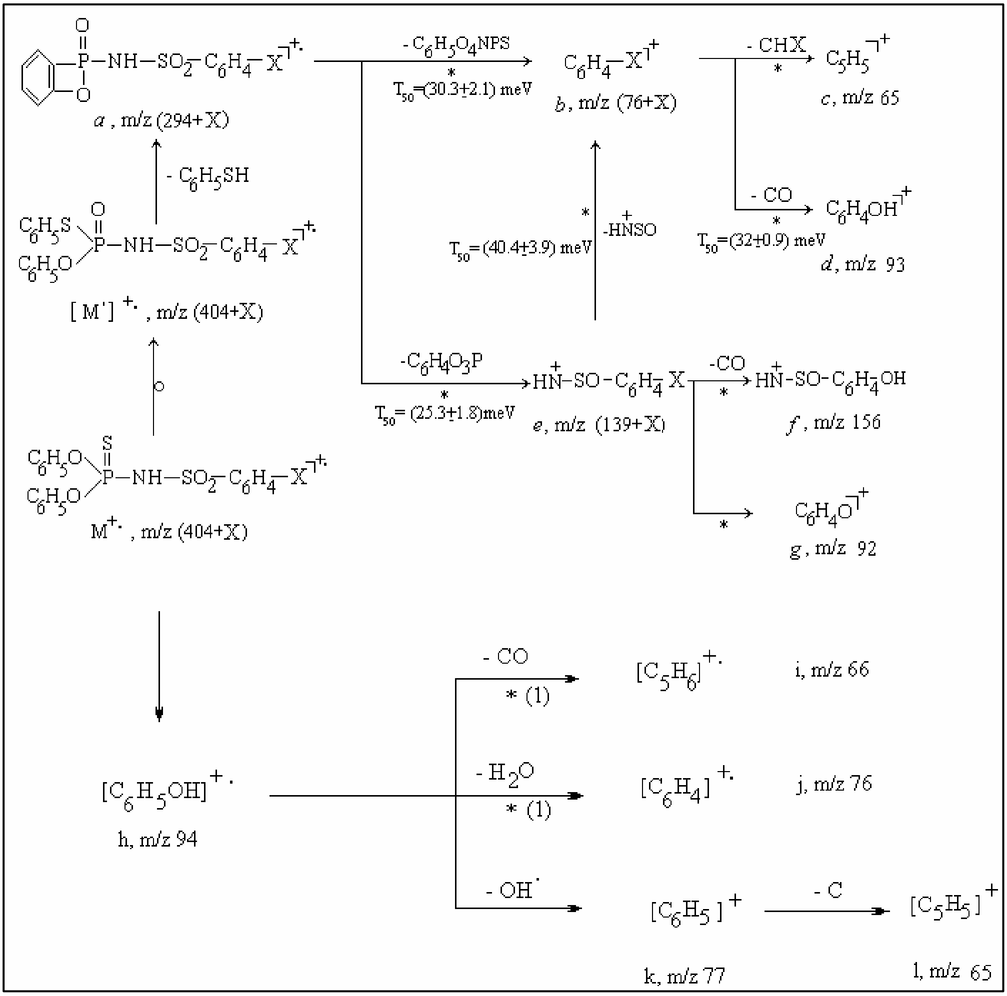

Fig. 3. *Fragmentation pattern suggested for compounds **1-4**.*
(= detected metastable ion cleavage in HV or MIKE mode)*

The ion *a* loses the relatively stable, large molecule $C_6H_5O_4NPS$, to yield the structure *b*, m/z (76+X), by the cleavage of the S-C bond, probably an electron is withdrawn by the SO_2 group, with the positive charge left on the aryl group. The kinetic energy release of 30,3±2,1 meV, is slightly greater than that usually found for simple bond fission, and may originate in the reverse activation energy E_o^r, as the peak shape is wider than a pure Gaussian one ($r \cong 3,6$) (figure 4), reflecting a rather complex fission mechanism [13,14].

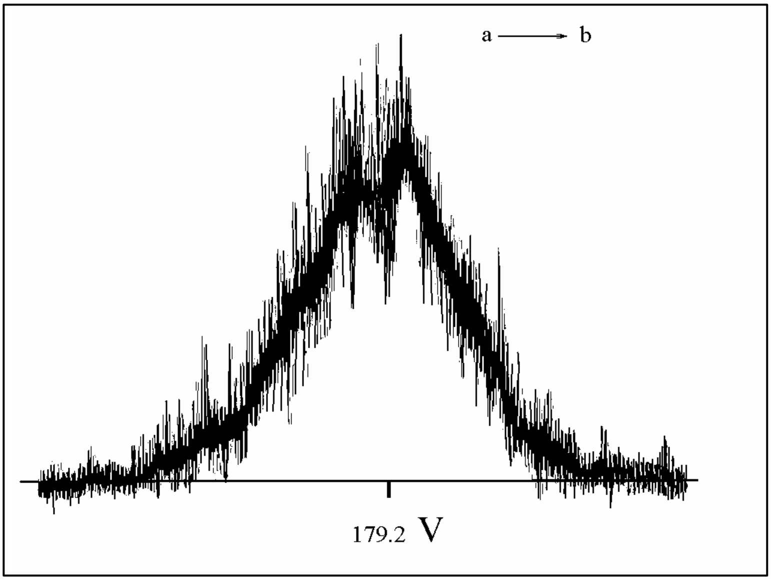

Fig. 4. *MIKE peak for the transition: a → b*

The ion *b* subsequently loses the (CXH) neutral fragment and generates the ion *c*, m/z 65, that produces the base peak in spectrum ***1,*** and relatively abundant (> 30 %) peaks in the other three compounds. The process was detected as a metastable ion transition, but the poor quality signal did not allow the determination of the kinetic energy release in this case. Metastable ions analysis also provided evidence that the ion *b* further loses a stable, neutral CO molecule, resulting the ion *d*, m/z 93, with detectable peaks in compounds ***1-3,*** missing in spectrum ***4,*** due to the specific elemental composition of the X groups bonded to the aryl. By examining the structure of the parent ion *b*, the MIKE peak shape (fig. 5) wider than a pure Gaussian one ($r \cong 3.6$) and the value found for T = (32.0±0.9) meV, we suggest that the cleavage process involves a seven membered transition state, rather that a four membered one. This very probably indicates that the kinetic energy release originates in the reverse activation energy $\boldsymbol{E_o^r}$, T^r being dominant in T.

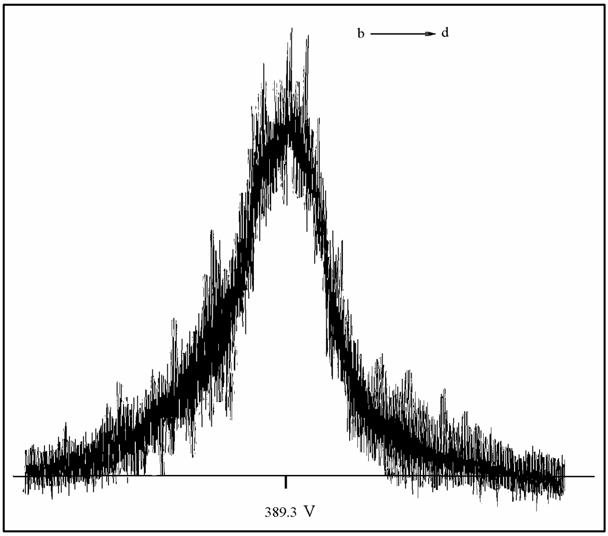

Fig. 5. *MIKE peak for the transition b → d.*

Following another fragmentation channel, through a five member transition state, the ion *a* may undergo the rearrangement of an O atom from the SO_2 group, prior to the loss of a neutral $C_6H_4O_3P$ radical, while the S atom changes its valence state from 6 to 4. The cleavage *a* → *e*, m/z (139+X), was detected in the slow scanning MIKE mode (fig. 6), the relatively small translation energy release T = 25,3+1,8 meV, and the Gaussian peak shape ($r \approx 3$) correspond to a cleavage driven by the excess energy of the activated complex E^{++} [13,14].

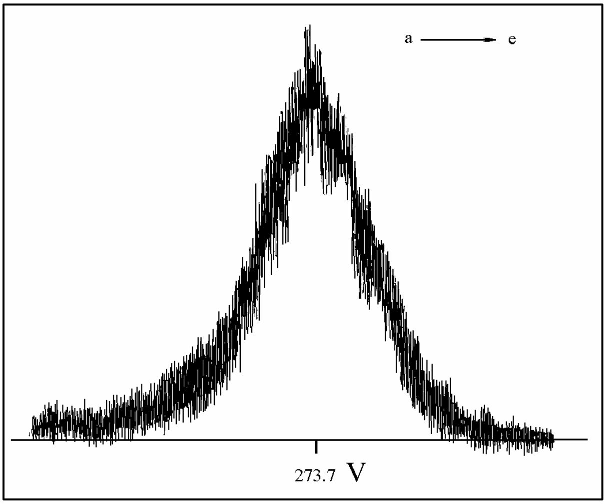

Fig. 6. *MIKE recording of the transition: a → e*

By metastable ions analysis we found that the ion *b* may also be formed from the ion *e*, by the fission of the S-C_{aryl} bond. We assume that the N atom withdraws an electron from the aryl group, and a neutral HNSO fragment is eliminated, the positive charge being transferred from N^+, onto the aryl group. The value T=40,4+3,9 meV, higher than in an ordinary simple fission, and the peak shape (fig. 7) wider than a pure Gaussian one ($r \cong 3,8$), indicates that possibly the whole structure *e* is excited by the complex fragmentation process. Thus, a significant value of the reverse energy E_0^r probably determines the dominant contribution of T^r to the total kinetic energy release in this case.

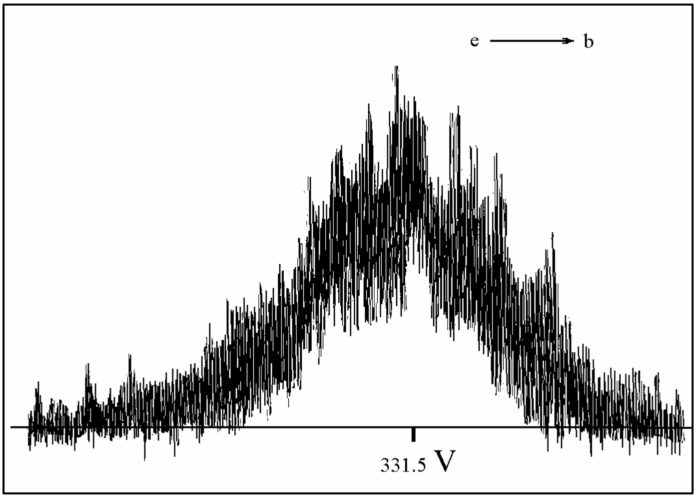

Fig. 7. *MIKE recording of the transition : e → b*

Along another fragmentation channel, the ion *e* may also lose a neutral CO molecule, to generate the ion *f*, m/z 156, of relative abundance 9 % in the spectrum of compound **1**, the process being detected via metastable ions analysis. The relatively abundant ion *e*, m/z (139+X) may produce the fragment ion *g*, m/z 92, detected as the daughter of the ion at m/z 184, in compound **1**.

A series of abundant ions is likely to originate in a reaction involving a five membered transition state, and the migration of a H atom from one phenoxy group to the other, the process yielding the ion *h*, m/z 94. This was not detected as a metastable ion transition, but the HR mass measurements confirmed the elemental composition of the ion *h*, and the subsequent fragmentations were supported by DADI analysis with fixed accelerating voltage and magnetic field. Thus, for the ion *h* two daughter ions were found: *i*, m/z 66 and *j*, m/z 76, both checked by accurate mass measurements, and resulted by the elimination of the neutral CO and H_2O molecules, respectively, as marked in the scheme of figure 3.

The ion *k*, m/z 77 is probably formed from *h*, by the elimination of a neutral OH radical. Accurate mass measurements supported the elemental compositions of both ions *k* and *h*, as well as the well known products at m/z: 65, 51, 50, typical for the spectra of molecules undergoing the phenyl group cleavage [22-24].

CONCLUSIONS

All the four mass spectra exhibit no peak for the molecular ions, that are likely to undergo the thion-thiol isomerisation with the subsequent elimination of the neutral C_6H_5SH molecule, giving rise to remarkably abundant peaks in all spectra. Based on the values found for the kinetic energy release in compound **1** and on the metastable peak shapes, the fragmentation mechanisms were suggested for each process. The reverse activation energy E_o^r was found significant in most cases, except for the reaction involving the migration of an O atom, through a five membered transititon state, that seemed rather controlled by the excess energy of the activated complex E^{++}.

REFERENCES

1. W. Lorenz, K. Mannes and G. Schrader (inventors), Farbenfabriken Bayer Aktiengesellschaft (Germany) (assignee), French Patent 1.301.634, 1961.
2. L. Almasi: "Les composes thiophosphororganiques", Ed. Masson, Paris (1976)
3. M. Sauli (inventor), Rhône-Poulenc SA, France (assignee), German Patent 2.431.192, 1973, Phosalone, *Chem. Abstr*. **82** (1975) 170877 b.
4. I. Fenesan, R. Popescu, A. Scozzafava, V. Crucin, E. Mateiciuc, R. Bauer, M. Ilies, C.T. Supuran, *J. Enzyme Inhibition*, vol **15** (2000) 297-302.
5. I. Fenesan, I. Chiorean, A. Hantz, Al. Alexandru, R. Pop, *Farmacia,* vol. **XXXVI,** nr. 3 (1988) 143-150.K
6. A. Scozzafava, F. Briganti, C.T. Supuran, I. Fenesan, R. Popescu, V. Muresan, S. Fărcas, Main Group Metal Chemistry, vol. 19 (1996) 503-510.
7. L. Almasi, R. Popescu, L. Paskucz, Rev. Roum. Chimie, vol 24 nr. 1 (1979) 3-12.
8. M. Culea, N. Palibroda, Z. Moldovan, S. Nicoară, I. Fenesan, R. Popescu, V. Muresan, E. Postoiu, V. Znamirovschi, *Rapid Commun. Mass Spectrom*., **12** (1998) 1808-1812.
9. R. Popescu, I. Fenesan, F. Badea, Rev. Roum. Chimie, **37**, 5 (1993) 19-28.

10. Z. Moldovan, M. Culea, N. Palibroda, R. Popescu, V. Muresan, O. Musat, *The Sci. Total Environ.,* **132** (1993) 147-154.
11. D. G. Durand and D. Barcelo, *Anal. Chim. Acta*, **243** (1991) 259-268.
12. H. J. Stan, B. Abraham, J. Jung, M. Kellert, K. Steihland, *Fresenius Z. Anal. Chem*., **287** (1977) 271-278.
13. R. G. Cooks, J. H. Beynon, R. M. Caprioli, G. R. Lester: "Metastable Ions", Elsevier, Amsterdam (1973).
14. Z. Moldovan, N. Palibroda, V. Mercea, G. Mihăilescu, *Org. Mass Spectrom*., **20**, 2 (1985) 77-82.
15. J. H. Beynon and R. K. Boyd, *Adv. Mass Spectrom*., **78** (1987) 1115-1124.
16. J. F. Elder, R. G. Cooks, J. H. Beynon, *Org. Mass Spectrom*., **11** (1976) 423-430.
17. I. L. Holmes and A. D. Osborne, *Int. J. Mass Spectrom. Ion Phys*., **23** (1977) 189-198.
18. Simona Nicoară: "Spectrometria de masă cu impact electronic în investigarea structurii moleculelor unor compusi organici biologic activi", teza de doctorat (1997).
19. J. Elders, J. H. Beynon and R. G. Cooks, *Org. Mass Spectrom*, **10** (1975) 273-288.
20. A. Mendez, W. D. Mead, A. C. Brenton, C. J. Proctor and J. H. Beynon, *Int. J. Mass Spectrom. Ion Phys*., **36** (1980) 57-64.
21. I. Fenesan, R. Popescu, C.T. Supuran, Simona Nicoară, Monica Culea, N. Palibroda, Z. Moldovan and O. Cozar, *Rapid Commun. Mass Spectrom.,* **15** (2001) 721-729.
22. J. Seibl: "MassenSpektrometrie", Akademische Verlagsgesellschaft, Frankfurt-am-Main (1970).
23. Z. Moldovan, Simona Nicoară, Monica Culea, O. Cozar, I. Fenesan, P. Vegh and J. J. Rios, *J. Molec. Struct*., **348** (1995) 393-396.
24. Simona Nicoară, Monica Culea, N. Palibroda, O. Cozar, I. Fenesan and A. Hantz, *Rapid Commun. Mass Spectrom*., **9** (1995) 61-63.

STUDIA UNIVERSITATIS BABEŞ-BOLYAI, PHYSICA, XLVII, 1, 2002

CHARGE CARRIERS LIFETIME DISTRIBUTION FOR CDSE EPITAXIAL LAYERS

GEORGETA CERBANIC[1], I. BURDA, S. SIMON[1]

ABSTRACT. The study of lifetimes regarding the recombination of non-equilibrium carriers and their kinetics is essential in order to explain the recombination mechanisms in semiconductors. The recombination kinetic and lifetime's values in CdSe epitaxial layers are the target of this paper. CdSe layers have been deposited on (0001) mica substrates by vapour epitaxial method. The epitaxial layers contain defects that induce gap states and specific recombination kinetics. The lifetimes were determined by Photoconductive frequency-resolved spectroscopy (PCFRS) a usual method for such measurements. The obtained lifetime spectra show, in all studied samples, that are present three types of recombinations mechanisms: lifetime τ_1 is due to bulk band-to-band recombination, lifetime τ_2 to recombination associated with chemical impurities and τ_3 to recombination associated with structural defects. The lifetime measured as a function of the substrate temperature denotes a complex correlation between the crystal perfection and the growth temperature.

Introduction

The thin layers of the CdSe semiconductor compounds are very attractive for the manufacture of electronic devices. The CdSe semiconductor has high photosensitivity and high luminescence quantum efficiency. The carrier lifetime distribution in a semiconductor is important for material's characterisation and/or for device evaluation. The recombination kinetics and lifetime of a luminescence process often provide evidence crucial to the understanding of its recombination mechanism [1]. The application fields of CdSe, wurtzite (hexagonal) structure are IR optics, substrates, detectors, sources for vacuum deposition [2,3].

In the Shockley-Hall-Read (SHR) mechanism [4], recombination may be monomolecular over a very wide range of excitation intensity. The recombination probability between a given electron and a single hole is close to one; the probability of recombination with any other hole is small. First-order kinetics, strictly, should refer to an exponential decay with lifetime independent of carrier density. For SHR recombination at low excitation

---

[1] *Babes-Bolyai University, Faculty of Physics, 3400, Cluj-Napoca, Romania*

pulse intensities and direct recombination at low injection levels, like in the case of PCFRS, the kinetics is first-order and the recombination lifetime can be obtained directly from the peak position of the PCFRS response. This is because the excitation is a small perturbation of the metastable excited state. The carriers injected by the pulse are sparse compared with the metastable carriers and do not interact with each other during their decay.

The spectrometer theory

The experimental system consists in an ensemble of centres with a distribution of lifetime *$P(\tau)$*. The kinetics is then first-order and monomolecular, although the form of the decay curve is left unspecified. If the excitation is modulated at an angular frequency ω it may be written as

$$G(t)=G_0+g\sin(\omega t),\ g<G_0 \tag{1}$$

where G(t) is the excitation rate at the time t, G_0 is the value at the moment $t_0=0$ and g is amplitude of the modulation. For a component of the luminescence with a lifetime τ (with $\tan\phi=\omega\tau$), one may write

$$I(\tau,t)=G_0+g\cos\phi\sin(\omega t-\phi) \tag{2}$$

The lock-in output is

$$S(\tau)=(2\pi)^{-1}\omega\int_0^{2\pi/\omega} I(t)R(t)dt \tag{3}$$

and for quadrature the lock-in response function R(t) is given by

$$R(t)=-\cos(\omega t) \tag{4}$$

and the expression (3) becomes

$$S(\tau)=g/[(\omega\tau)^{-1}+\omega\tau] \tag{5}$$

The lock-in output from all lifetimes components as the frequency sweeps is

$$S(\omega)=\int_0^{\infty} P(\tau)S(\tau)d\tau \tag{6}$$

For the response function of the in-phase frequency-resolved spectroscopy (FRS) method, it is merely necessary to replace R(t) above by

$$R(t)=\sin(\omega t) \tag{7}$$

giving

$$S(\tau)=g/(1+\omega^2\tau^2) \tag{8}$$

The in-phase FRS gives the integral of lifetime distribution, between the limits $\tau \sim (\omega)^{-1}$ and ∞, while in the quadrature FRS gives the lifetime distribution directly.

The foregoing analysis assumes that the indirect recombination is through a set of centres whose lifetime distribution is independent of excitation power (or independent of the pump rate G). This condition is not satisfied in the case of optical saturation of long-lives centres and distant-pair recombination.

The depth of modulation, g/G_0, in practical FRS experiments, is typically 10% to 30% that ensures a better signal-to-noise ratio in comparasion with TRS technique. Because the PCFRS technique uses the sample as detector the depth of modulation can be fixed up to 20% with very good discrimination performance. The excitation power is very low because only a super-bright LED also commercially available, ensures the light [5]. But all this experimental condition in approximation of this theory can be an advantage [6]. The performance of the signal generator (responsible for light modulation) and lock-in amplifier is very important in PCFRS technique. So we used the quadrature method of the frequency-resolved spectroscopy.

Results and discussion

The CdSe layers were grown onto (0001) oriented mica substrates by vapour epitaxial method at a remanent gas-pressure of $2 \cdot 10^{-5}$ torr. The vapour epitaxial method consists in the transport of source material from the region with high temperature, where CdSe thoroughly dissociates in Cd and Se atoms, to the region with low temperatures, due to the temperature gradient. CdSe polycrystals heated at 800°C were used as evaporation sources. Information on layers structure and crystal perfection were obtained from the analysis of metallographic micrographs and X-ray diffraction [7], which indicate that the growth of crystallites from CdSe layers correspond to hexagonal modification.

The measurements of the lifetime spectrum of the CdSe epitaxial layers were performed using a photoconductive frequency-resolved spectroscopy. The PCFRS [8] available has the time-scales and resolution in the range of the lifetime of carriers in the CdSe semiconductor compounds. The quadrature method of the frequency-resolved spectroscopy with an infinitely small signal amplitude modulation, and the detection carried out by using a digital lock-in amplifier is the basic technique used by the PCFRS. The advantage of this method in comparison with classical time-resolved spectroscopy (TRS) is presented by Depinna and Dunstan [1].

In Figure 1 are presented the lifetime spectra of the CdSe epitaxial layers. The data plotted in figure 1 contain real data collected with PCFRS described above using CdSe epitaxial layers grown on (0001) oriented mica at various substrate temperatures between 672°C and 545°C (a-d).

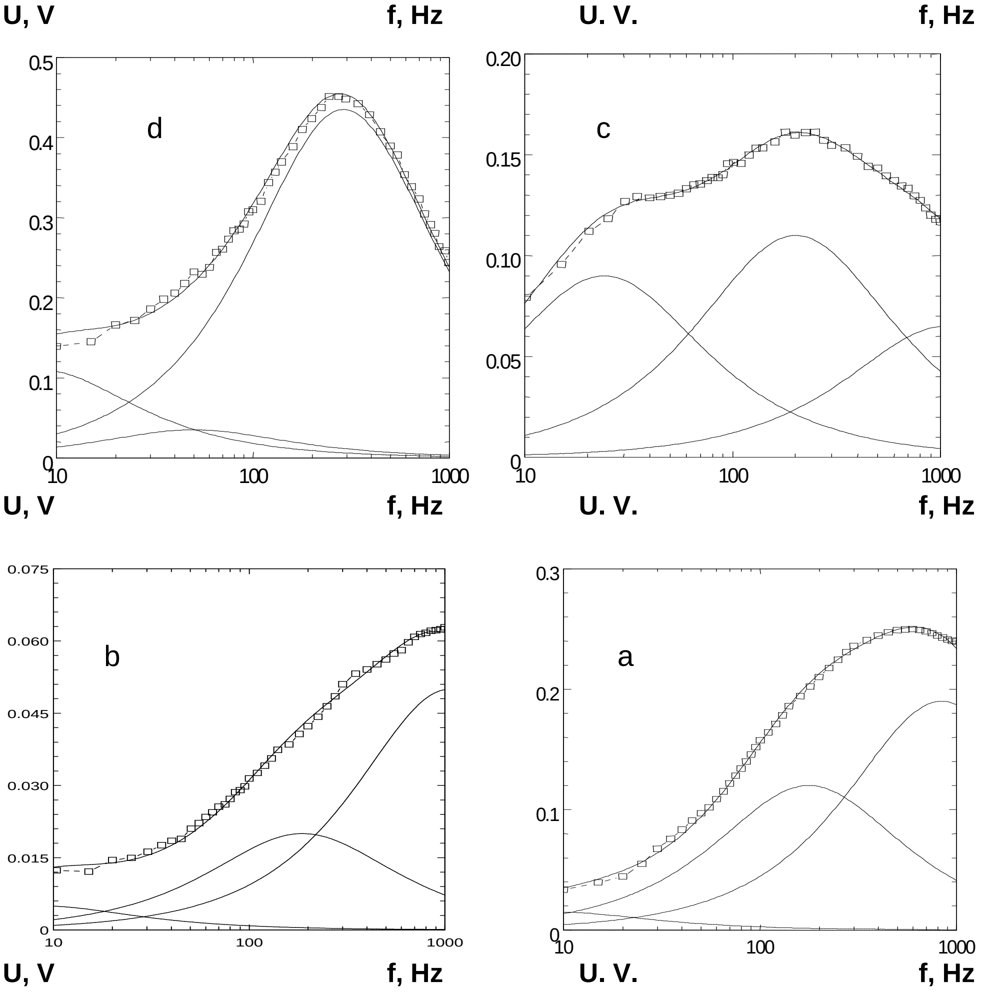

Fig. 1. *Lifetime spectra of the CdSe epitaxial layers grown on (0001) mica substrates at various temperatura: (a) 545^{0}C; (b) 565^{0}C; (c) 662^{0}C; (d) 672^{0}C.*

Multilifetimes are obtained for these samples. Lifetime data, determined using a smooth and a good deconvolution, can be obtained by taking into account three lifetimes distributions. The lifetimes values are calculated with relation $\tau=1/(2\pi f)$, where f is the frequency of signal response in peak position.

In order to obtain information about the recombination of carriers and lifetimes parameters of the material, equation (5) was fitted with the experimental measurements of the lifetime spectrum of the CdSe epitaxial layers [9]. The lifetimes values obtained from this fitting procedure and the substrate temperature of analysed samples are summarised in Table 1. Complex data processing can be made with a dual microprocessor data acquisition system [8], the parallel data processing being a very fast solution. These values of lifetimes denote the complexity of the recombination process in CdSe compounds. The epitaxial layers contain defects that induce gap states and specific recombination kinetics.

Table 1.

The lifetime values of the CdSe epitaxial layer grown on (0001) oriented mica by vapour epitaxial method at various substrate temperatures.

Sample	Substrate temperature, °C	τ_1, ms	τ_2, ms	τ_3, ms
a	545	0.19	0.90	17.6
b	565	0.15	0.85	18.7
c	662	0.15	0.79	6.60
d	672	0.55	3.20	19.2

The capture efficiency of carriers in the gap states (the recombination associated with chemical impurities or structural defects) depends on the capture cross section, which is a measure of the probability of the capture event. The Shockley-Read-Hall statistics is the basic model used for interpretation the recombination process of the non-equilibrium carriers [6]. The three lifetimes could be explained assuming that τ_1 is due to band-to-band recombination, τ_2 to surface recombination associated with chemical impurities and τ_3 to surface recombination associated with structural defects [10].

The lifetime measured as a function of the substrate temperature is shown in Figure 2.

By increasing the substrate temperature from 545°C to 565°C, the lifetimes τ_1 and τ_2 decrease, while τ_3 increases. Continuing to rise the substrate temperature one remarks that the lifetime τ_1 and τ_2 take constant values, but τ_3 decreases. These data denote a complex correlation between the crystal imperfection and the growth temperature. Thus, the crystal perfection is improved as the growth temperature ranges between 565°C-662°C. At highest investigated (672°C) substrate temperature increased values for all lifetimes are obtained that could be assigned to non-radiative recombination of carriers at defects or impurities.

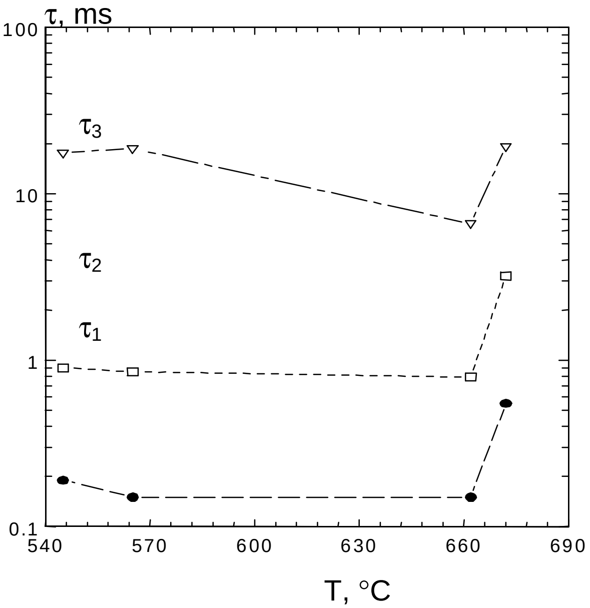

Fig. 2. *The lifetime values as a function of the substrate temperature for CdSe epitaxial layers.*

Conclusions

The paper reports the lifetime distribution for CdSe epitaxial layers using the photoconductivity frequency-resolved spectroscopy (PCFRS). The methods for spectrum fitting are adapted for lifetime determination in the semiconductor compounds. The three lifetimes could be explained assuming that τ_1 is due to band-to-band recombination, τ_2 to surface recombination associated with chemical impurities and τ_3 to surface recombination associated with structural defects. Lifetimes measured as a function of the substrate temperature lead to a complex correlation between the crystal perfection and the substrate temperature.

REFERENCES

1. S. P. Depinna, D. J. Dunstan, Philosophical Magazine B. Vol. 50, pp. 579-597, 1984.
2. S. Grabtchak, M. Cocivera, *Phys. Rev*. B. 50: pp.18219-18225, 1994.
3. S. Grabtchak, M. Cocivera, *Journal of Applied Physics*. 79, pp. 786-793,1996.
4. W. Shockley, W.T. Read, Phys. Rev. 87, 835, (1952).

5. K. P. Homewood, P. G. Wade, D. J. Dunstan, J. Phys. E: Sci. Instrum. 21(1), pp. 84-85, 1988.
6. Y. Rosenwaks, D. Huppert, Y. Shapira, Phys. Rev. B, 44, pp.13097-13100, 1991.
7. G. Cerbanic, S. Simon, P. Gasin, A. Focsha, C. Rotaru, Studia Universitatis Babes-Bolyai, Physica, XLIV, 2, 2000.
8. I. Burda, Rev. Sci. Instrum. Vol. 71, 1, pp. 182-185, 2000.
9. D. Goldfarb, A. Idnani, Math. Programming, 27, pp. 1-33, 1983.
10. R. Krause-Rehberg, H. S. Leipner, T. Abgarjan, A. Polity, Materials Science & processing, pp. 599-614, 1998.

STUDIA UNIVERSITATIS BABEŞ-BOLYAI, PHYSICA, XLVII, 1, 2002

SOLVENT INFLUENCE OF LOCAL MOBILITY OF THE POLYISOPRENE OBSERVED BY NMR METHOD

M. TODICA[1]

ABSTRACT. The correlation time of local dynamics of the polyisoprene - CCl_4 and polyisoprene - $CDCl_3$ solutions was evaluated from the NMR spin-lattice relaxation data. The mobility of the polymeric chain is influenced by the nature of the solvent.

Introduction

The local dynamics of the polymeric segments is a complex processes which is mainly influenced by some factors, the temperature, the temporary or permanent connections between different chains, or by the presence of the solvent molecules in the vicinity of the polymeric chain.

The aim of this work is to observe the influence of some solvents, with very closed molecular structure, the CCl_4 and $CDCl_3$, on the local motion of the polyisoprene chains, by NMR method.

Experimental

Our polymer of interest was the polyisoprene IR307, with the microstructure 92% "cis", and the glass transition temperature, $T_g = 201 \pm 3$ K, in molten state and in solution. We utilized two solvents, CCl_4 and $CDCl_3$ with very similar molecular structure. We prepared polyisoprene-CCl_4 solutions with the polymeric concentration Φ=77%, Φ=59%, and polyisoprene-$CDCl_3$ solution with the concentration Φ=62%.

The samples were enclosed in NMR tubes (diameter 4 mm) and sealed under primary vacuum.

All measurements were performed using a CXP Bruker spectrometer working at 45MHz, in the temperature range 244K to 344K. The spin-lattice relaxation time was measured using the "inversion recovery" method, [1]. The sample temperature was controlled within 1K.

Results and discussion

The most important motions that governs the dynamics of the entire chain are the rotation of the elementary polymeric segments around the local symmetry axis, [2]. Every rotation of C-C and C-H bonds modifies the relative orientation of the nuclear spins and thus the dipolar interaction between the neighboring spins. Now it is very well established that the main

---

[1] *"Babes-Bolyai" University, Faculty of Physics, RO-3400 Cluj-Napoca, Romania*

mechanism that governs the relaxation of the longitudinal magnetization associate to the spin system, is the dipolar interaction [3, 4]. This interaction decrease rapidly with the distance between the interacting spins, $\left(1/r^6\right)$, so that only the neighboring spins are taken into account [5]. But the dipolar interaction, and thus the relaxation processes of the magnetization, is mainly influenced by the local fluctuations of the polymeric segments. At a result it is possible to established a relation between the spin-lattice relaxation ratio, $1/T_1$, and the correlation time of the local fluctuation of the polymeric segments τ_C, [6, 7]. It is possible in these conditions to obtain information concerning the microscopic parameter τ_C, by analyzing another parameter, easy to measure, the spin-lattice relaxation time, T_1. The algorithm for this procedure is described in the reference [8].

This method is based on the model of the passage of a particle over a potential energy barrier, [9, 10]. The correlation time of the local segments fluctuations is given by the relation:

$$\tau_C = B\exp\left(\frac{E_a}{RT}\right) \tag{1}$$

B is a parameter depending on the nature of the sample and E_a is the activation energy required for conformational transition.

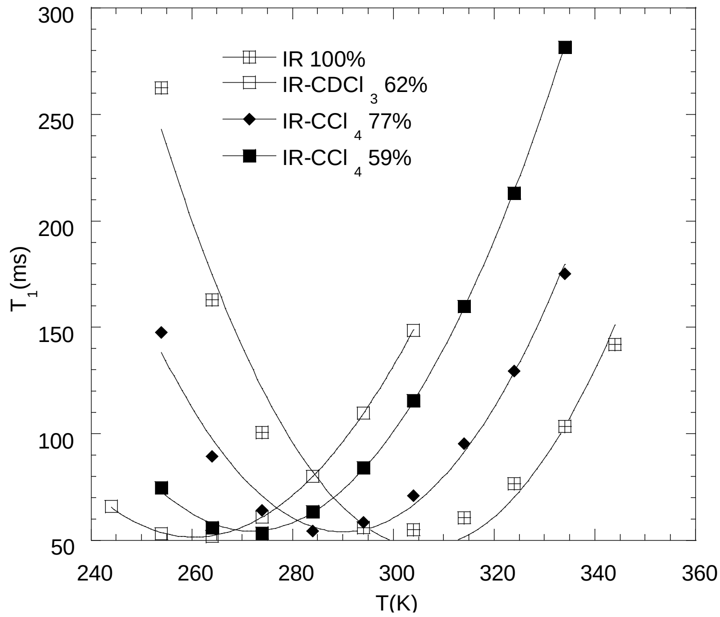

Fig. 1. *Temperature dependence of the spin-lattice relaxation time*

The parameters B and E_a can be obtained by analyzing the temperature dependence of the spin-lattice relaxation data:

$$\frac{1}{T_1} = K\left[\frac{\tau_c}{1+\omega^2\tau_c{}^2} + \frac{4\tau_c}{1+4\omega^2\tau_c{}^2}\right] \tag{2}$$

Two particular situations are of great interest:

-the extreme narrowing limit, $\omega\tau_c <<1$,

- the minimum of the spin-lattice relaxation time, $\frac{\partial T_1}{\partial T} = 0$.

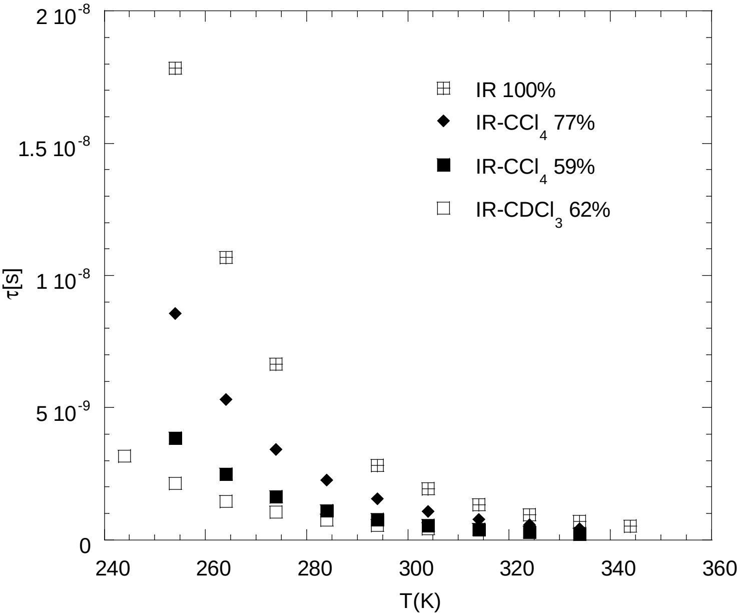

Fig. 2. Temperature dependence of the correlation time of the molten polyisoprene, polyisoprene-CCl_4 and polyisoprene-$CDCl_3$ solutions.

The aim of our work is to evaluate the values of the correlation time of the local polymeric fluctuations, for two different solvents, CCl_4 and $CDCl_3$. The CCl_4 molecule is characterized by a very high symmetry. The presence of deuterium atom in the molecule of $CDCl_3$, has as a effect the modification of the symmetry of this molecule by rapport of molecule CCl_4. It is interesting to observe the modification induced by this difference of solvent molecular symmetry on the local dynamics of the polymer. These solvents do not contain protons, that they do not contribute to the magnetization of the sample so that, in all the cases we observed only the behavior of the protons attached to the polymeric chain.

The temperature dependence of the spin-lattice relaxation, for all the samples, is represented in figure 1. For each sample the minimum of the spin-lattice relaxation time is observed for temperatures higher than the glass transition temperature of the molten polymer. We can observe that polymeric solutions with different solvents, but having concentrations so closed each to other, (i.e., IR-CCl_4 Φ = 59% and IR- $CDCl_3$, Φ =62%), presents relaxation curves very similar. Little differences can be observed in the domain of low temperatures. This behavior suggest, in the first approximation, that the relaxation process is very similar for the solutions containing the two solvents. However, a detailed analyze is based on the observation of the correlation time of the local dynamics of polymeric segments for all the samples.

Using the procedure presented in reference [8], we calculated the parameters E_a and B for each sample, and then the correlation time, (Table 1). The values of the correlation time are presented in figure 2.

We can observe for each sample that the correlation time decrease when the temperature increase, that indicate an increasing of the local mobility of the polymer with the temperature.

Table 1

Sample	**Φ**	**E_a (kj/mol)**	**B[s]**
IR	100%	29.3	$17.1 \cdot 10^{-15}$
IR+CCl_4	77%	26.5	$30.23 \cdot 10^{-15}$
IR+ CCl_4	59%	24.7	$31.4 \cdot 10^{-15}$
IR+$CDCl_3$	62%	20.6	$119.7 \cdot 10^{-15}$

For a given temperature and concentration, we can observe that the correlation time of the polyisoprene in CCl_4 solution is greater that in the $CDCl_3$ solution. That means that the local mobility of the polymer is greater in the presence of $CDCl_3$ molecules. On the other hand, the difference between the values of the correlation time corresponding to the polyisoprene-CCl_4 and polyisoprene-$CDCl_3$ solutions is greater in the domain of low temperatures and decreases for higher temperatures. This situation is illustrated in figure 3, for two temperatures, T=254K and T=294K. We can suppose that the local mobility of the polyisoprene is mainly determined by the thermal fluctuations of the chain segments, in the domain of high temperatures. The little difference which exist between the two solvents, do not induces greater modifications of this dynamics in the domain of high temperatures. The influence of the two solvents is more important in the domain of low temperatures.

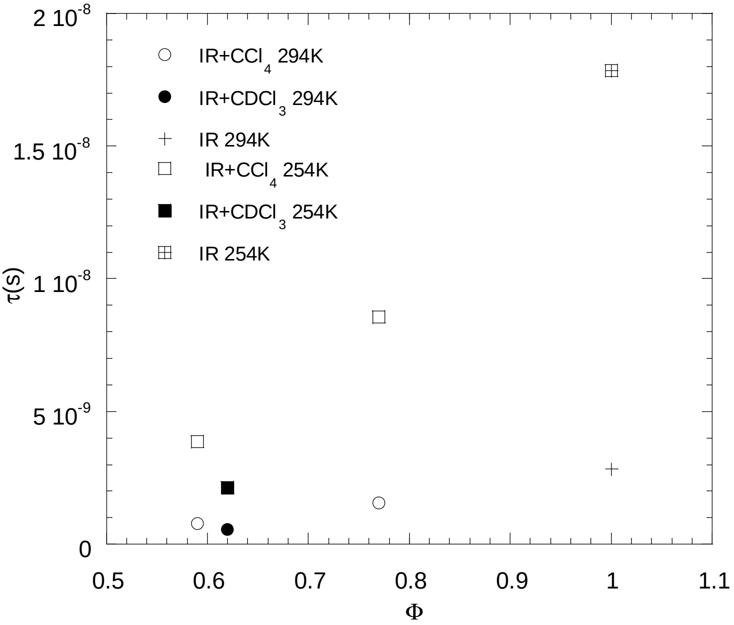

Fig. 3. *Concentration dependence of the correlation time of the molten polyisoprene, polyisoprene-CCl_4 and polyisoprene-$CDCl_3$ solutions for the temperatures T=254K and T=294K*

Conclusion

The correlation time of local dynamics of the polymeric chains can be evaluate by analyzing the temperature dependence of the spin-lattice relaxation of the protons attached to the chain. This correlation time is influenced by the presence of solvent molecules in the vicinity of the polymeric chain.

Little difference between the structure of the solvent molecules can induce modifications of the local dynamics of the polymer. This effect was observed in the case of two solvents, with molecular structures very similar, CCl_4 and $CDCl_3$.

For a given temperature and concentration, the mobility of the polyisoprene is greater in the solution of $CDCl_3$ than in the solution of CCl_4.

The contribution of the solvent to the mobility of the polymeric chain is more important in the domain of low temperatures. At high temperatures the polymer dynamics is mainly determined by the thermal fluctuations of the chain.

Little difference between the structure of the solvent molecules can induce modifications of the local dynamics of the polymer. This effect was observed in the case of two solvents, with molecular structures very similar, CCl_4 and $CDCl_3$.

For a given temperature and concentration, the mobility of the polyisoprene is greater in the solution of $CDCl_3$ than in the solution of CCl_4.

The contribution of the solvent to the mobility of the polymeric chain is more important in the domain of low temperatures. At high temperatures the polymer dynamics is mainly determined by the thermal fluctuations of the chain.

REFERENCES

1. H. Y. Carr, E. R. Purcell, Phys. Rev., 94, 630, (1954).
2. P. G. De Gennes, Scaling concepts in polymers physics, Cornell University Press, Ithaca, New-York, (1979).
3. J. P. Cohen-Addad, Physical properties of polymeric gels, J. Wiley, Chicester, (1996).
4. J. P. Cohen-Addad, NMR and fractal properties of polymeric liquids and gels, Pergamon Press, London, (1992).
5. I. Abragam, The Principles of Nuclear Magnetism, Clarendon Press, Oxford, (1961).
6. J. R. Lyera, High resolution nuclear magnetic spectroscopy, Academic Press, New York, (1980).
7. Ya. Slonim, A. N. Lyubimov, The NMR of polymers, Plenum Press, New York, (1970).
8. M. Todica, S. Simon, C. Cozma, O. Cozar, E. Matei, Talanta, 53, (2000).
9. H. A. Kramers, Physica, 7, 284, (1940).
10. E. Helfand, J. Chem. Phys., 54, 4651, (1971).

STUDIA UNIVERSITATIS BABEŞ-BOLYAI, PHYSICA, XLVII, 1, 2002

ION CURRENT TO A LANGMUIR PROBE IN MULTI-COMPONENT MULTIPLY IONIZED PLASMA

L. KENÉZ*, J. KARÁCSONY*, A. LIBÁL*

ABSTRACT. Based on theories of collisionless sheath and pre-sheath, it was possible to deduce ion current expressions to a Langmuir probe immersed in a magnetized plasma with different ion charge states. Obtained expressions can be used at electron cyclotron resonance (E. C. R.) multiply charged ion source plasma diagnosis.

Introduction

Langmuir probes find widespread use in the field of plasma diagnosis [1,2]. While this technique is relatively simple and convenient, some efforts are required to interpret the probe data in terms of plasma characteristics of electron density n_e, electron and ion temperatures T_e, T_i, plasma potential V_p, etc. [3] In recent years the Langmuir probe was used to measure plasma potential profiles, density gradient and electron temperature in the E. C. R. ion source plasma in various conditions [4,5]. However, theoretical models concerning Langmuir probe data interpretation do not take into account a basic property of the E. C. R. ion source, namely that an E. C. R. plasma contains multiply charged ions. This introduces errors especially in electron density measurements.

Usually, the electron density is determined from the electron saturation current of the Langmuir probe characteristics [3]. In the presence of magnetic fields, however, the electron saturation current is depressed by a large factor compared with a field free situation [6]. The electron saturation reduction factor contains a number of parameters which are generally unknown to the experimentalist attempting to apply the theory to the Langmuir probe data. As a consequence of this departure from the ideal behavior, in case of Langmuir probe usage in strong magnetic fields, it is recommended to use the $V \leq V_f$ region of the characteristics, where V_f is the floating potential, and the electron density to be calculated using the value of the ion saturation current [7,8]. In the $T_i << T_e$ case when ions are singly-charged, the ion saturation current is given by the Bohm current [1,7,8]. In the multi-component

---

*Babeş-Bolyai University Cluj-Napoca. RO-3400, Str. M. Kog¾lniceanu Nr. 1, Romania plasma with multiply charged ion species the simple expression of the Bohm current is not adequate. The aim of this paper is to deduce the expression for the ion current to a Langmuir probe immersed in a multi-component plasma with multiply charged ions.

The Bohm criterion for multi-component plasma

It is well known that if we insert a probe into a plasma, for probe potentials smaller than the plasma potential, most of the applied potential appears as a voltage drop across the thin electrostatic sheath between the collector and the plasma (the sheath thickness is of the same order as the Debye length) [3]. However, this shielding of the plasma from the applied electric field by the sheath is imperfect [2,7]. A pre-sheath penetrates deep into the plasma, attracting ions and repelling electrons. Thus, the ion distribution is strongly perturbed and the ions are accelerated to enter into the sheath with the so-called Bohm velocity – a result which was first derived by Bohm [11], by considering the conditions required for a monotone potential variation within the sheath. The same result, however, can be obtained by considering the limiting conditions for the pre-sheath [12]. In the case when $T_i << T_e$ and ions are singly-charged, the hydrodynamic form of the Bohm criterion can be written as [3,11]

$$v_s \geq \sqrt{\frac{kT_e}{m_i}} \tag{1}$$

where v_s is the ion velocity at the sheath edge, k is Boltzmann's constant and m_i is the ion mass. Since from the pre-sheath analysis for the ion velocity at the sheath edge results that [12]

$$v \leq \sqrt{\frac{kT_e}{m_i}} \tag{2}$$

it is accepted [2,7] that the Bohm velocity for the singly-charged ions (with $T_i = 0$) is [7]:

$$v_B = \sqrt{\frac{kT_e}{m_i}} \tag{3}$$

In order to obtain a generalized form of the Bohm criterion for a multi-component plasma with different charge state ions we will carry out a quasi-neutral pre-sheath analysis. We will consider a magnetized plasma system composed of electrons, several ion species (i), and neutrals. The electron density n_e is assumed to be a function of the electric potential V [3].

$$\mathrm{n_e = n_e\,(V)} \tag{4}$$

To describe the ion dynamics, we start from fluid equations [9]

$$\frac{\partial n_{ij}}{\partial t} + \nabla\left(n_{ij}\vec{v}_{ij}\right) = s_{ij} \tag{5}$$

$$m_i\frac{\partial \vec{v}_{ij}}{\partial t} + m_i\vec{v}_{ij}\nabla\vec{v}_{ij} = e_j\left(\vec{E} + \vec{v}_{ij}\times\vec{E}\right) - \frac{1}{n_{ij}}\nabla p_{ij} - \vec{R}_{ij} \tag{6}$$

where n_{ij} is the number density of the ions of mass m_i and charge $\mathrm{e_j = j \cdot e}$ (j = 1,2,…) characterizes the charge state), v_{ij} is the average flow velocity for these ions, ***E*** = *-∇V* designates the electric field, ***B*** is the magnetic field, s_{ij} represents the source term (production or destruction of the ions of mass m_i and charge e_j) and $\boldsymbol{R}_{ij}$ is an effective ion friction force. To close the system of moments equations, we will use the thermodynamic equation of state relating the pressure p_{ij} of the ions of mass m_i and charge e_j to the number density n_{ij} [10]:

$$\nabla p_{ij} = \gamma_{ij} k T_{ij} \nabla n_{ij} \tag{7}$$

where *k* is Boltzmann's constant, T_{ij} the temperature of the ion component with mass m_i and charge e_j, γ_{ij} is the ratio of specific heat at constant pressure to that at constant volume, that depends on the flow conditions ($\gamma_{ij}=1$ for isothermal ion flow, $\gamma_{ij}=5/3$ for adiabatic flow with isotropic pressure, and $\gamma_{ij}=3$ for one-dimensional adiabatic flow).

Since we are interested with the strongly magnetized plasma, we will analyze the case of a plasma flow along magnetic field lines (oriented along *0z* axis) to a solid surface perpendicular to the ***B*** field. There we can use a one–dimensional, steady-state flow model. The equation of continuity (5) is thus

$$\frac{d}{dz}\left(n_{ij}v_{ij}\right) = s_{ij} \tag{8}$$

and the momentum equation (6) is:

$$m_i v_{ij}\frac{dv_{ij}}{dz} = -e_j\frac{dV}{dz} - \frac{1}{n_{ij}}\frac{dp_{ij}}{dz} - R_{ij} \tag{9}$$

Using the closure condition (7) and combining Eqs. (8) and (9), we obtain

$$\left(m_i v_{ij}{}^2 - \gamma_{ij}kT_{ij}\right)\frac{dn_{ij}}{dz} = e_j n_{ij}\frac{dV}{dz} + n_{ij}R_{ij} + m_i v_{ij}s_{ij} \tag{10}$$

Now, it is convenient to introduce an effective electron temperature based on the generalization of the Boltzmann relation [7]

$$T_e = \frac{e n_e}{k} \frac{\frac{dV}{dz}}{\frac{dn_e}{dz}} \tag{11}$$

(Note that for non-Maxwellian electrons T_e is not the kinetic temperature). Introducing (11) into equation (10) we obtain:

$$\frac{dn_{ij}}{dz} = \left(\frac{e_j n_{ij}}{e n_e} k T_e \frac{dn_e}{dz} + n_{ij} R_{ij} + m_i v_{ij} s_{ij} \right) \left(m_i v_{ij}{}^2 - \gamma_{ij} k T_{ij} \right)^{-2} \tag{12}$$

From the pre-sheath's quasi-neutrality condition, written under the from

$$\sum_{i,j} n_{ij} e_j = n_e e \tag{13}$$

we deduce the relation

$$\sum_{i,j} e_j \frac{dn_{ij}}{dz} = e \frac{dn_e}{dz} \tag{14}$$

Introducing (12) into (14) we obtain:

$$\left(1 - \sum_{i,j} \frac{n_{ij} e_j{}^2}{n_e e^2} \frac{k T_e}{m_i v_{ij}{}^2 - \gamma_{ij} k T_{ij}} \right) \frac{dn_e}{dz} = \sum_{i,j} \frac{e_i}{e} \frac{n_{ij} R_{ij} + m_i v_{ij} s_{ij}}{m_i v_{ij}{}^2 - \gamma_{ij} k T_{ij}} \tag{15}$$

Obviously we have a singularity whenever the bracket on the left side vanishes. In this case the derivative of n_e with respect to z becomes infinite and thus the plasma solution fails (i. e. the quasi-neutral assumption fails). This corresponds physically to the termination of the plasma and the start of the sheath with its large electric field [12]. Thus, the relation

$$\sum_{i,j} \frac{n_{ijs} e_j{}^2}{m_i v_{ijB}{}^2 - \gamma_{ij} k T_{ijs}} = \frac{n_{es} e^2}{k T_{es}} \tag{16}$$

can be accepted as the generalized Bohm criterion, where all quantities with index s are evaluated at the sheath edge and v_{ijB} is the Bohm velocity for the ions with mass m_i and charge e_j.

The ion saturation current

The generalized Bohm criterion, Eq. (16), can be used to estimate the ion current to a negatively biased probe in a strongly magnetized plasma. Although it was assumed that the solid surface is perpendicular to the ***B*** field, it has been shown that at least for non-drifting ion distributions, the angle between the B field and the normal to the surface has little effect on the Bohm criterion [13]. Then, if the probe size exceeds the ion Larmor radius so that the ion flow towards the probe is along the magnetic field lines, one has to take into account that the effective area of the probe is reduced to the projection of the actual area on the plane perpendicular to the magnetic field [2]. If the probe has a projected area A_{pr} and if the ions entering the collisionless sheath have a drift velocity v_{ijB}, then the ion current collected by the probe is

$$I_s^{ion} = A_{pr} \sum_{i,j} n_{ijs} e_j v_{ijB} \tag{17}$$

To determine v_{ijB}, the Bohm velocity of the *j*-charged ion, we will use the generalized Bohm criterion (16) and we will assume a collisionless pre-sheath, a good approximation for a low pressure plasma with $T_i << T_e$. Then, the energy conservation requires:

$$\frac{m_i v_{ijB}^2}{2} + e_j V_s = e_j V_p \tag{18}$$

where we used the cold ions approximation ($T_{ij} = 0$). Combining Eqs. (16) and (18), for the potential drop trough the pre-sheath we obtain:

$$V_p - V_s = \frac{kT_e}{2e} \tag{19}$$

while for v_{ijB}, the expression is:

$$v_{ijB} = \sqrt{\frac{jkT_e}{m_i}} \tag{20}$$

Now, we introduce an empirical factor in Eq. (17) to express the ion saturation current as a function of electron density n_{es}. Denote n_s^+ the average ion density (number of ion per unit volume of the plasma irrespectively of their charge at the edge of the sheath) and α_{ij} a number between 0 and 1 that shows in what percent a certain charge state can be found in the plasma. It is obvious that

$$n_{ijs} = \alpha_{ij} \overline{n}_s^+ \tag{21}$$

From the quasi-neutrality condition (13) we immediately obtain the expression for n_s^+:

$$\overline{n}_s^+ = \frac{n_{es}}{\sum_{i,j} j\alpha_{ij}} \tag{22}$$

Inserting the expressions (20) and (21) into Eq. (17) and using this last equation, we obtain a relation between the ion saturation current and the electron number density at the sheath edge under the form

$$I_s^{ion} = n_{es} A_{pr} e \sqrt{kT_e} \frac{\sum_{i,j} \frac{\alpha_{ij} j^{\frac{3}{2}}}{m_i^{\frac{1}{2}}}}{\sum_{i,j} j\alpha_{ij}} \tag{23}$$

Taking into account that we are only interested in the analysis of the ion current region of the Langmuir probe characteristic, where the electrons feel a retarding electric field, we can assume as a good approximation that the electron density satisfies the Boltzmann relation:

$$n_{es} = n_{e0} \exp\left[\frac{e(V_s - V_p)}{kT_e}\right] \tag{24}$$

which combined with Eq. (19) gives

$$n_{es} = n_{e0} e^{-\frac{1}{2}} = 0.61 n_0 \tag{25}$$

Using this result, we obtain from Eq. (23) the final form for the ion saturation current:

$$I_s^{ion} = 0.61 n_{e0} A_{pr} e \sqrt{kT_e} \frac{\sum_{i,j} \frac{\alpha_{ij} j^{\frac{3}{2}}}{m_i^{\frac{1}{2}}}}{\sum_{i,j} j\alpha_{ij}} \tag{26}$$

Conclusions

Based on the theories of collisionless sheath and pre-sheath it was possible to deduce the expression of the ion saturation current to a Langmuir probe immersed in a strongly magnetized multi-component plasma with different ion charge states. The obtained expression can be used in the diagnosis of an E. C. R. multiply charged ion source. An E. C. R. plasma satisfies, to a good approximation, the conditions that are needed to apply the relation (26) for the ion saturation current. All ions with different charge stages have the same temperature and this common temperature is $T_i << T_e$ [14].

The plasma is confined by magnetic fields of $B \approx 1\ T$, thus it is strongly magnetized. The empirical parameters α_{ij} can be determined experimentally from the extracted beam spectra, since the plasma conditions are well reflected by the extracted beam when plasmas containing mostly lower charge states are considered and the probe is outside the resonant zone.

Acknowledgements

One of the authors (J. Karácsony) would like to thank the Domus Hungarica Scientarum et Artium Foundation for the fellowship held while the investigation in this work was being performed.

REFERENCES

1. N. Herskowitz, In Plasma Diagnostics, vol. I., (ed O. Auciello, D. Flamm) Academic Press, Boston (1988) p. 113.
2. P. C. Stangeby, In Plasma Diagnostics, vol. II., (ed O. Auciello, D. Flamm) Academic Press, Boston (1988) p. 157.
3. F. F. Chen, In Plasma Diagnostic Techniques, (R. H. Huddlestone and S. L. Leonard eds.) Academic Press, New York p. 113.
4. Y. Kato, S. Ishii, Rev. Sci. Instrum. 69, 1176 (1998).
5. L. Kenéz, S. Biri, J. Karácsony, A. Valek, E. C. R. Plasma diagnostic with Langmuir probe, ATOMKI Annual Report 1999 p. 75.
6. P. C. Stangeby, J. Phys. D: Appl. Phys. 15, 1007 (1982).
7. P. C. Stangeby, C. M. McCracken; Nucl. Fusion 30, 1225 (1990).
8. P. C. Stangeby, In Physics of Plasma-Wall Interactions in Controlled Fusion (D. E. Post and R. Behrisch eds.) J. Wiley, New York (1981).
9. W. M. Stacey, Fusion Plasma Analysis, Wiley, New York (1981).
10. F. F. Chen, Introduction to Plasma Physics and Controlled Fusion, Plenum Press, New York (1984).
11. D. Bohm, The Characteristics of Electrical Discharges in Magnetic Fields, Eds. A. Guthrire and R. K. Wakerling, McGraw Hill, New York, Chapt. 3 (1949).
12. P. C. Stangeby, Phys. Fluids 27, 682 (1984).
13. R. Chodura, Phys. Fulds 25, 1628 (1982).
14. G. D. Shrikov, C. Mühle, G. Musiol, G. Zschornak, Nucl. Instr. and Meth. A 302,1 (1991).

STUDIA UNIVERSITATIS BABEŞ-BOLYAI, PHYSICA, XLVII, 1, 2002

EPR STUDIES OF SPIN LABELED NICOTINIC ACID DERIVATIVES IN LIPIDIC BILAYERS

V. MICLAUS[1], G. DAMIAN[2], C.M. LUCACIU[3]

ABSTRACT. 3- and 4-[N-4-(2,2,6,6-tertamethylpiperidinyloxy)]-carboxamide-1-R-(where R=methyl or R=dodecyl)-pyridinium-iodide free radicals were synthesized and investigated as new useful spin labels. X-band EPR spectra of all four compounds were studied in the presence of multilamelar liposomes. The spectra were analyzed by using a computer simulation for obtaining the characteristic magnetic parameters. We investigated the influence on the EPR characteristics of: a) the alkyl chain R and b) the substituent position on the pyridine ring of the nitroxide moieties. Both, the length of the alkyl chain and the substituent positions induce changes in the EPR parameters. The interactions between the compounds and multilamelar liposomes were derived from the magnetic EPR parameters**.**

Keywords: spin label, multilamelar liposomes, EPR

Introduction

The EPR of nitroxide spin labeled biological molecules have been extensively used in the last decades for the study of their interactions, mobility and microenvironment in biological systems [1-3]. The EPR spectra from nitroxide spin-labelled biomolecules are sensitive to rotational motions on the scale of 10^{-11} to 10^{-8} sec, which is determined essentially by the relaxation processes arising from modulation of the ^{14}N-hyperfine and g-value anisotrpies.

Lipids are a diverse group of biological substances made up primarily or exclusively of nonpolar groups. As a result of their nonpolar character, lipids typically dissolve more readily in nonpolar solvents such as acetone, ether, chloroform, and benzene, than in water. This solubility characteristic is of extreme importance in cells because lipids tend to

---

[1] *"Babes-Bolyai" University, Department of Chemistry, RO-3400 Cluj-Napoca, Romania*

[2] *"Babes-Bolyai" University, Department of Physics, RO-3400 Cluj-Napoca, Romania*

[3] *University of Medicine and Pharmacy "Iuliu Hatieganu", Department of Biophysics and Radiopharmacy, RO-3400 Cluj-Napoca, Romania*

associate into nonpolar groups and barriers, as in the cell membranes that form boundaries between and within cells. Besides having important roles in membranes, lipids are stored and used in cells as an energy source. Other lipids form parts of cellular regulatory mechanisms. Lipids link covalently with carbohydrates to form glycolipids and with proteins to form lipoproteins. Their are three major classes of lipids: neutral lipids, phospholipids and steroids[4]. Membrane proteins, residing in highly insulating lipid bilayers, catalyze vital reactions such as solute transport, charge separation and conversion of energy, as well as signal transduction. A contribution to understanding such fundamental vectorial processes at a molecular level requires knowledge of the dymamics of the guest molecules in the lipid bilayer by EPR spectroscopy [5, 6]. Spin label methods have found wide application in the study of mobility of labelled biomolecules in the fluid bilayer lipid [7, 8]. We present in this work results concerning the usefulness as paramagnetic probes in biological systems of some newly synthesized spin labeled nicotinic acid derivatives. The syntheses were performed in order to obtain derivatives with both different lengths of the chain and positions of the substituent [9]. In the same time the moieties of the nitroxid radicals behave as quaternary ammonium salts too.

EPR spectra were recorded for the spin labeled compounds in artificial lipidic bilayer membranes. Using spin label nicotinic acid derivatives labelled by the paramagnetic group at diferent positions in aromatic ring, it becomes possible to study the influence of the the position of nitride group on the magnetic parameters and molecular mobility [10].

Materials and methods

3-and 4-[N-4-(2,2,6,6-tetramethylpiperidinyloxy)]-carboxamide -1-R-(where R=methyl or R=dodecyl)-pyridinium-iodide free radicals (Fig. 1) were investigated as new useful spin labels.

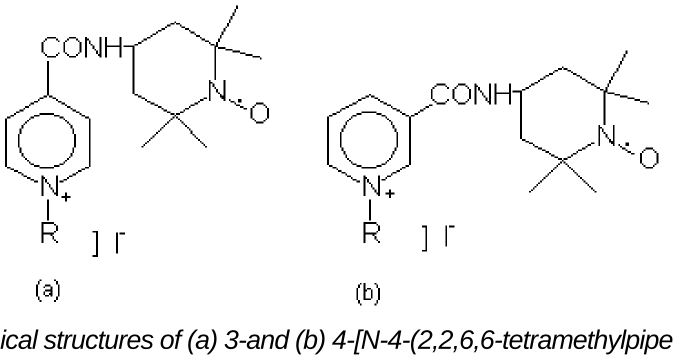

Fig. 1. *Chemical structures of (a) 3-and (b) 4-[N-4-(2,2,6,6-tetramethylpiperidinyloxy)]-carboxamide -1-R-(where R=methyl or R=dodecyl)-pyridinium-iodide free radicals.*

Multilamelar liposomes were obtained by simply hydrating a lecithin film (Lecithin ex soja, purum Serva) obtained after the evaporation under nitrogen of an organic solvent solution of lipids at final concentration of 50 mg/ml.

EPR spectra were recorded at room temperature with a JEOL-JES-3B spectrometer, operating in the X-band, equipped with a computer acquisition system. The computer simulation analysis of the spectra was made by using a program that is available to the public through the Internet (http://alfred.niehs.nih/LMB) for obtaining the magnetic characteristic parameters.

Results and discussion

The ESR spectra of labelled nicotinic acid derivatives molecules consist of two components, one of which represents the fluid bilayer lipid environment in the membrane, and the other in aqueous environment. The best fit for all four compounds were simulated by using two paramagnetic species both having magnetic characteristics of the nitroxide radicals but with different A and g tensors (Table 1).

Table 1.

EPR parameters of studied samples.

Sample	**Species**	**g_0**	**A_0** (gauss)
3-[N-4-(2,,6,6-tetramethylpiperidinyloxy)]-carboxamide -1- dodecyl -pyridinium-iodide spin label	1	2.0018	8.96
	2	2.0021	16.89
4-[N-4-(2,2,6,6-tetramethylpiperidinyloxy)]-carboxamide -1- dodecyl -pyridinium-iodide spin label	1	2.0023	9.15
	2	2.0022	16.98
3-[N-4-(2,2,6,6-tetramethylpiperidinyloxy)]-carboxamide -1- methyl -pyridinium-iodide spin label	1	2.0019	8.85
	2	2.0024	16.94
4-[N-4-(2,2,6,6-tetramethylpiperidinyloxy)]-carboxamide -1- methyl-pyridinium-iodide spin label	1	2.0023	8.42
	2	2.0023	16.91

The shapes of the EPR spectra, presented in Fig. 2 and Fig. 3, are isotropic for both types of the paramagnetic centers. One of the two species has an unusual low hyperfine constant ($\langle A \rangle \simeq 9$ G) and is due to the delocalization of the nitrogen unpaired electron, probably caused by an intermediate spin exchange interaction due to the association of spin probe in multilamelar liposomes. For intermediate exchange interaction, the outer hyperfine lines move in the towards the central line by an amount which is given by efective reduction in the nitrogen hyperfine splitting constant [7]. At the 9.5-GHz microwave frequency and 3500 G field of conventional EPR spectroscopy with nitroxide spin labels, anisotropic contributions to the spectra are dominated by nitrogen hyperfine structure. This interaction may be due either to a local association of two or more labeled molecules or to the presence of a biradical structure. The rotational correlation time calculated from the magnetic data, assuming a brownian diffusion model, is about $5*10^{-10}$s, corresponding to a weakly increased viscosity of the environment.

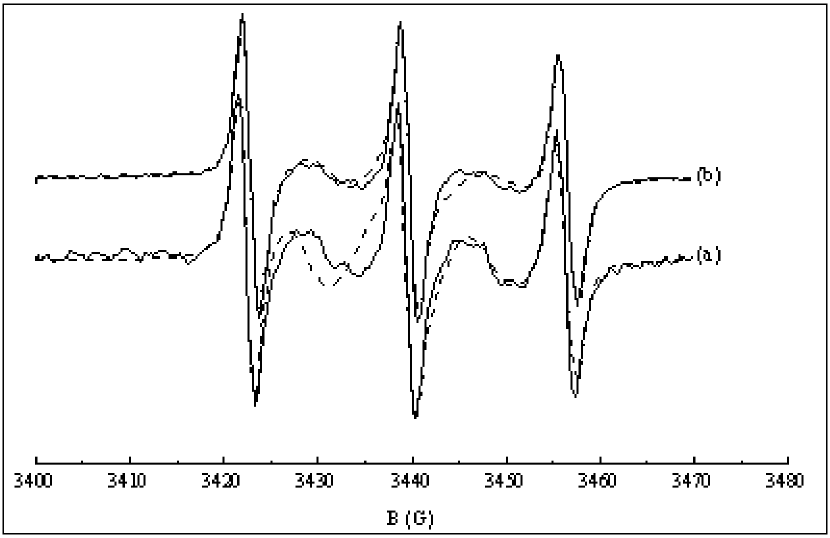

Fig. 2. *Experimental (continuum line) and simulated (doted line) EPR spectra of (a) 3- and (b) 4-[N-4-(2,2,6,6-tetramethylpiperidinyloxy)]-carboxamide -1- dodecyl-pyridinium-iodide free radicals in in multilamelar liposomes water solutions.*

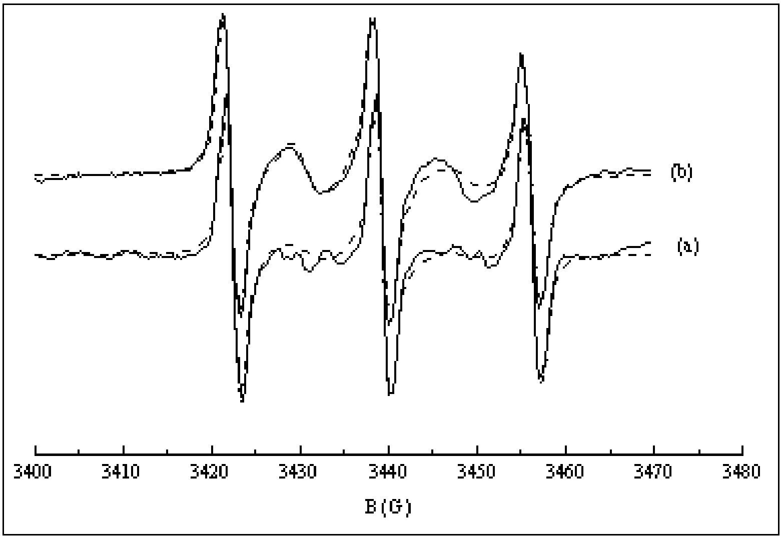

Fig. 3. *Experimental (continum line) and simulated (doted line) EPR spectra of (a) 3- and (b) 4-[N-4-(2,2,6,6-tetramethylpiperidinyloxy)]-carboxamide -1- methyl-pyridinium-iodide free radicals in multilamelar liposomes water solutions.*

The other species having the hyperfine constant of about 17 G, very close to the usual value for labeled organic molecules in isotropic media with low viscosity. The calculated rotational correlation time (about $4*10^{-11}$s) is due to the free brownian motion of the molecule.

Replacing the methyl with the dodecyl group leads to an expected change in the mobility of the molecules.

In the present study we observed that for membranes (multilamelar liposomes), the signal corresponding to the lower A value species is more pronounced as compared to the preliminary test involving the BSA and human blood plasma media.

Conclussion

The EPR study of the mobility of 3-and 4-[N-4-(2,2,6,6-tetramethylpiperidinyloxy)]-carboxamide-1-methyl-pyridinium-iodide and 3- and 4-[N-4-(2,2,6,6-tetramethylpiperidinyloxy)]-carboxamide-1-dodecyl-pyridinium-iodide free radicals in multilamelar liposomes water solutions, show that there are two populations of spin probe in multilamelar liposomes layers moities: one well exposed on the water environment, and the other immersed into the fluid liposomes layers. The low value of the hyperfine constant of the immersed species due to the intermediate spin exchange interaction, show a relative high association of the spin probe in multilamelar liposomes.

REFERENCES

1. Brown, L. R. and Wüthrich, K. *Biochim. Biophys. Acta* 468, 356 (1977).
2. de Jongh, H. H. J., Ritsema, T. and Killian,J. A. *FEBS* Lett. 360, 255 (1995).
3. Vanderkooi, J., Erecinska, M. and Chance, B*. Arch.Biochem, Biophys*. 157, 531 (1973).
4. Rothfield, L.I., ed. *Structure and Function of Biological Membranes*, Academic Press, New York, (1971).
5. N. Kocherginsky, H.M. Swartz*, Nitroxide Spin Labels, Reactions in Biology and Chemistry*, CRC Press, New York, 1995.
6. M.A. Hemminga, P.A. de Jager, in: L.J. Berliner, J. Rueben (Eds.), Biological Magnetic Resonance, vol. 8, *Spin Labeling. Theory and Applications*, Plenum Press, New York, 1989.

7. Marsh D. *Experimental methods in spin-label spectral analysis*, in: *Biological Magnetic Resonance,* Berliner L.R. & Ruben J. (Eds), Plenum Publishing corp., New York, 1989.
8. Meirovitch, E., A. Nayeem, and J. H. Freed, *J. Phys. Chem.* 88:3454 –3465 (1984).
9. (a) Snel, M. M. E., de Kruijff, B. and Marsh, D. *Biochemistry* 33, 7146 (1994).
   (b) Snel, M. M. E., de Kruijff, B. and Marsh, D. *Biochemistry* 33, 11150 (1994).
   (c) Snel, M. M. E. and Marsh, D, *Biophys. J.* 67, 737 (1994).
10. L.J. Berliner (Ed.), *Spin Labeling: Theory and Applications*, Academic Press, New York, 1976.

STUDIA UNIVERSITATIS BABEŞ-BOLYAI, PHYSICA, XLVII, 1, 2002

CALLIBRATION OF BETA SPECTRA BY COMPTON ELECTRONS

L. DARABAN[1]

ABSTRACT. One of must important problem is the calibration of the multichannel analysers in terms of beta ray energy. Is described a very simple method for this callibration adapted from the fast neutrons spectra processing with the plastic scintillators by using the Compton electron distribution.

Introduction

In the last time the plastic scintillator beta spectroscopy was applied to the beta spectra processing. Was prepared special programs for processing these spectra as the *Adriana* program and was used special approximation of the Fermi functions.

Large plastic scintillator characteristics study

A large area (45x48.5x4 cm) plastic scintillator, sideways coupled to a single photomultiplier tube type Canberra, with preamplifier type 2007 B, and acqusition system (Acquspec-board and Acquspec-software, incorporated in Pentium II computer, type Hewlett Packard) were used.

The detector dependence on the beta radiation energy was inspected. The energy-calibration has been made with Compton electrons and the end-point method from beta known spectra.

2.1. The *Compton electron method* is based on producing some spectra of Compton electrons (as in Fig.1) with the help of gamma radiation inside the plastic scintillator, which has a very low average atomically number Z.

When the gamma radiation energy is well known, the Compton edge value can be calculated with a classical formula [1] in which the condition θ is set to 180°:

$$E_{emax} = \frac{E_\gamma}{1+\frac{mc^2}{2E_\gamma}} \quad \text{or} \quad E_{emax} = \frac{2E_\gamma^2}{0.511+2E_\gamma} \qquad (1)$$

---

[1] *Faculty of Physics, University Babes-Bolyai 3400 Cluj-Napoca, Romania*

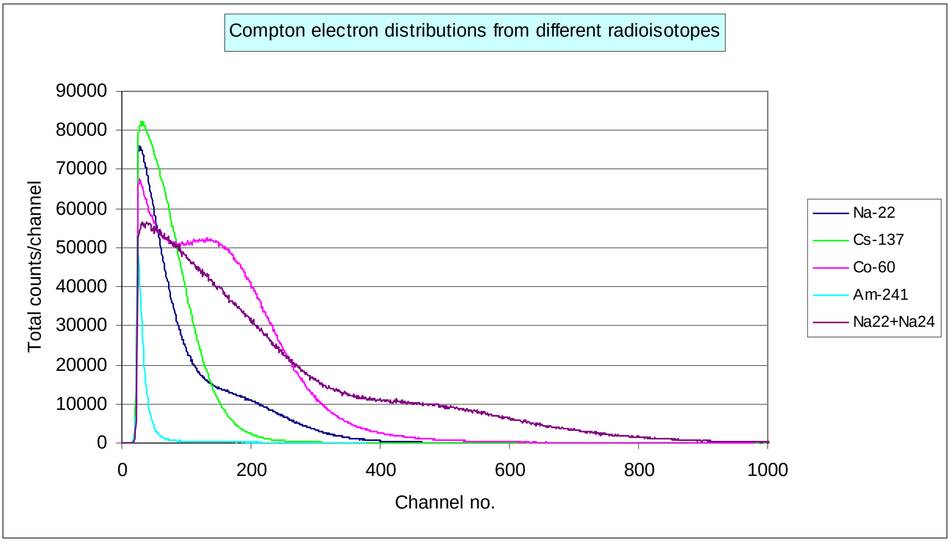

Fig.1. *Different Compton electron spectra*

The values calculated for different radionuclides and presented in Table no.1 were used for energy-calibration of the analyzer.

Table No.1

Radioisotope	**E_{γ}(MeV)**	**E_{emax} (Compton electrons) (MeV)**
^{22}Na	0.511	0.341
	1.275	1.07
^{137}Cs	0.662	0.478
^{60}Co	1.17 *	0.96 *
	1.33 *	1.12 *
	* average value: 1.25	*average value: 1.04
^{24}Na	1.37	1.15
	2.75	2.52
^{56}Mn	0.85	0.65
	1.81	1.59
^{38}Cl	1.64	1.42
	2.17	1.94
^{116m}In	0.42 (32.4)	0.26
	1.097 (55.7)	0.89
	1.29 (85.0)	1.08
	1.51 (10.0)	1.29
	2.112 (115.0)	1.88
	0.24 (6.95%)	0.11

Radioisotope	**E_γ(MeV)**	**E_{emax} (Compton electrons) (MeV)**
^{152}Eu	0.72 (20.2%)	0.59
	0.96 (10.2%)	0.76
	1.08 (17.2%)	0.88
	1.274 (35%)	0.9
^{57}Co	0.122	0.040
	0.136	0.0475
^{241}Am	0.060	0.011

In the first tests, it has been noticed that the large plastic scintillator has a weak energetical resolution and it’s not able to make the difference of ~0.2 MeV energy between the two Compton edges enclosed in the Compton electrons distribution of Co-60. Nevertheless the detector has a good linear energy-dependence up to 2 MeV. In publications in this domain there are many discussions about the technique of the E_{emax} edge positioning on the Compton electrons spectra as those from the Fig. 1, [2-5].

A new method of differential-type [6] was applied by which a program, *Ducir* smooths the spectrum and performs a differentiation for locating the Compton edge on the most abrupt descendent part of the spectrum. The following calibration curve was obtained: (Fig.2).

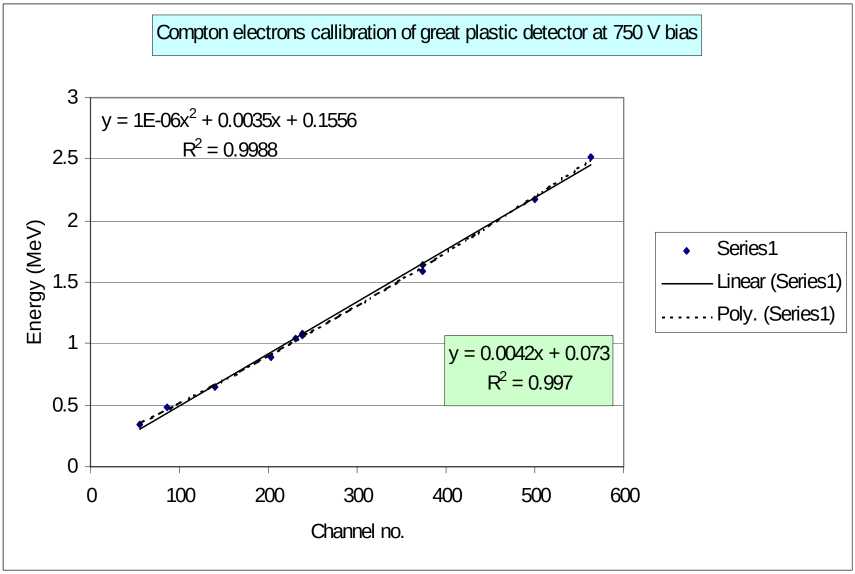

Fig.2. *Energy-calibration curve of the large plastic scintilator with the Compton electrons*

This method of calibration is in good agreement with the results obtained by others techniques from literature [7] for the position of the Compton edge localisation.

2.2. For the calibration in electron energies of the analyzer channels by *end-point method*, a criterion (or rule) has been settled for finding the beta spectra extremity, E_{max} in the semilogarithmical scale (Fig.3). We discovered that this E_{max} is the point, where the background spectrum intersects the beta spectrum (measured in similar conditions) (Fig.3). By fitting polynominal or exponential functions throught the spectra, the end-points are obtained by calculations and used to construct the calibration curve (Fig.4).

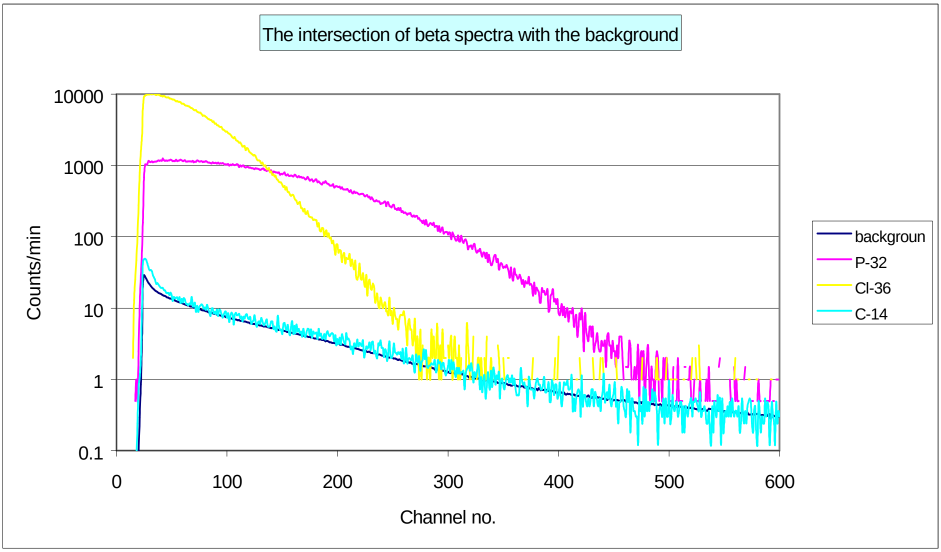

Fig 3. *Determination of end-point on the spectra of some pure beta radionuclides*

The validity of the energy calibration obtained by the end-point-method combined with the Compton-electon method was verified by applying it to the beta spectra processing (*Adriana* program) for some well-known radionuclides.

With this *Adriana* program these spectra, corrected for the secondary effects, were processed to obtain the Fermi-Kurie curves [7-10], which extrapolated to zero, give in fact the spectrum end-point for each curve (that is to say the maximum energy of beta radiation).

The values obtained using these calibration methods coincide with those indicated in literature for those radioactive isotopes (see Fig.5).

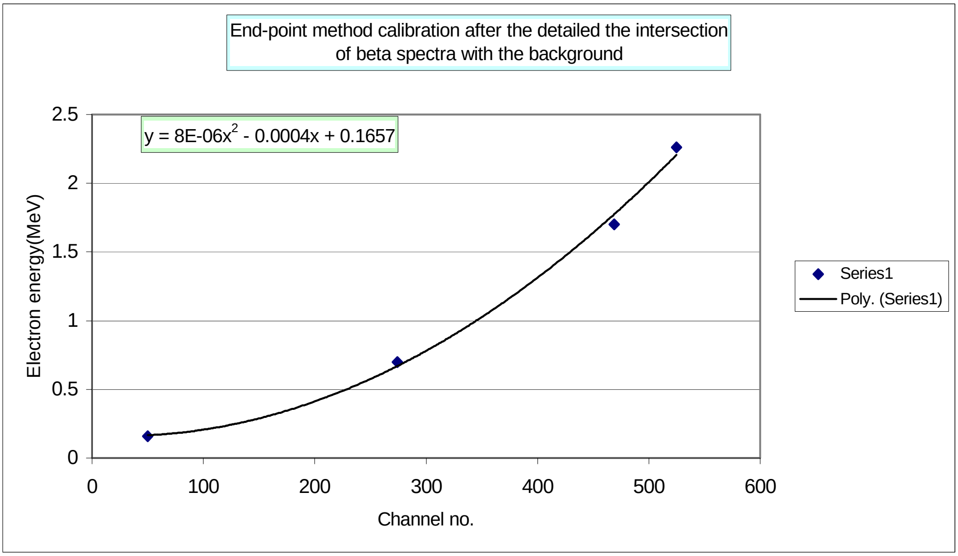

Fig. 4. *Calibration curve by the end-point method*

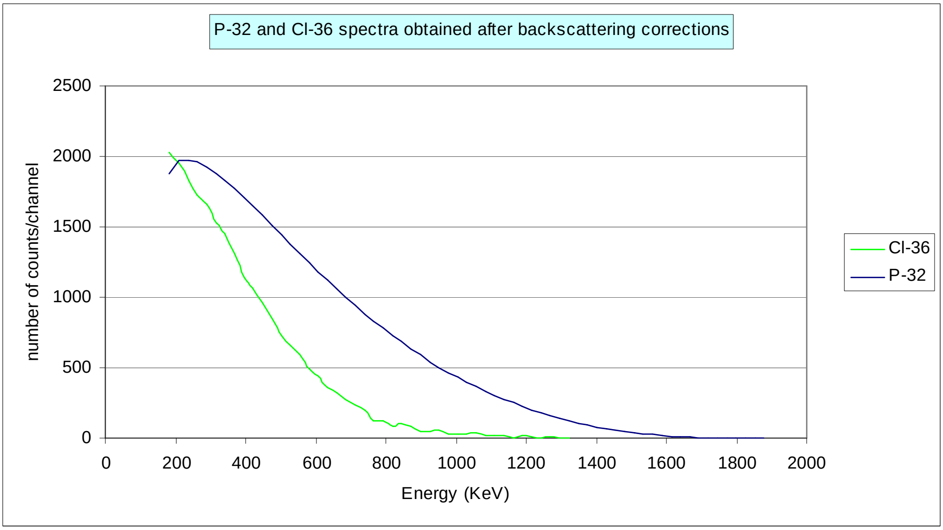

Fig.5. *Beta spectra obtained after backscattering corrections and deconvolution of the Fermi-Kurie curves with the Adriana program.*

Conclusions

The method, which uses detectors with plastic scintillators, is a beta-spetrometry type measurement for wast management and environmental studies.

It can be adapted to measure in ROI. (regions of interest) for beta-pure emitting known radionuclides with different energies from the large radioactive waste samples.

REFERENCES

1. E. Segrè et al*., Experimental Nuclear Physics*, p.280, ed. John Willey &Sons, N. Y.
2. E. Nardi, *Gamma ray measurements with plastic scintillators*, Nucl. Instr. Meth., **95**, 229-232 (1971).
3. I. T. Grissom, D.R. Koehler, Nucl. Instr. Meth., **37**, 336 (1965).
4. V. V. Verbinscki et al., Nucl. Instr. Meth., **65**, 8 (1968).
5. K. F. Flyn et al., Nucl. Instr. Meth., **27**, 13, (1964).
6. L. Daraban et al., Proc. Of the 2-nd Nat. Symp. *"Methods, Models and Techniques in Physics and Related Fields",* pp. 101-104, oct. 11-15, Cluj-Napoca, Romania, (1984).
7. F.K. Wohn, J. R. Clifford, G. H. Carlson, W. L. Tabert, Jr*., A plastic scintillation detector for beta-ray spectrum measurements*, Nucl. Instr. Meth., **101**, 343-352 (1972).
8. N. Tsoulfanidis, B. W. Wehring and M. E. Wyman, *The use of an analitical response function for unfolding beta spectra,* Nucl. Instr. Meth., **73**, 98-102, (1969).
9. P. C. Rogers, G. E. Gordon, *Computer analysis of beta-ray and conversion electron spectra observed with low-resolution detectors*, Nucl. Instr. Meth., **37**, 259-264 (1965).
10. A. H. Wapstra, G. J. Nijgh, R. Van Lieshout, *Nuclear Spectroscopy Tables*, (in russian ed. pp.58-76), edit.: North-Holland Publ. Comp., Amsterdam (1959).

STUDIA UNIVERSITATIS BABEŞ-BOLYAI, PHYSICA, XLVII, 1, 2002

EPR AND ENDOR INVESTIGATION ON A GAMMA-IRRADIATED SINGLE CRYSTAL OF L-TYROSINE-HCL

V. CHIŞ[1], A. L. MANIERO[2], M. BRUSTOLON[2], O. COZAR[1], L. DAVID[1]

ABSTRACT. X-band cw-EPR and ENDOR spectroscopies are used to investigate the tyrosyl radical produced in a gamma-irradiated single crystal of L-Tyrosine-hydrochloride, at room temperature. The radical, formed by hydrogen abstraction from the hydroxyl group attached to the aromatic ring of the Tyrosine molecule is found to exists in two slightly different conformations. Both of them are very close to the original position of the parent molecule in the crystal. Six hyperfine coupling tensors have been obtained by usual first order analysis of the ENDOR frequencies, three for each conformation of the radical in the host crystal. One of the β-methylene proton coupling is used to derive the conformation of the CH_2 group with respect to the aromatic ring of the radical.

Introduction

Tyrosine is involved in many protein oxidations, being one of the most easily oxidized amino acids and the tyrosyl radicals and related species are of considerable importance in biochemistry. They have been identified in enzymes such as ribonucleotide reductase (RNR), prostaglandin H synthase and the water splitting enzyme in plant photosynthesis[1-4]. Possible activity of further tyrosine radicals in RNR, plant photosynthesis and other biological systems has been suggested[5, 6]. Tyrosine derived radicals have been identified in galactose oxidase and amine oxidase[7, 8]. Recently, a tyrosyl radical has been reported as a heme catalase intermediate[9, 10].

The tyrosyl radicals in RNR and photosystem II (PSII) are extremely stable despite their high oxidizing potential. In the case of PSII the situation is more intriguing since the stable tyrosyl radical Tyr-D· does not participate in the electron transfer process, while the second tyrosyl radical, Tyr-Z· is a short-lived electron carrier. Moreover, current structural models of PSII place these tyrosyl radicals in symmetry related positions, one on each subunit of

---

[1] *Babeş-Bolyai University, Faculty of Physics, 1 Kog¾lniceanu, RO-3400 Cluj-Napoca, Romania*

[2] *Universita Degli Studi di Padova, Dipartimento di Chimica Fisica, Via Loredan 2, I-35131 Padova, Italy*

the PSII reaction center heterodimer[11]. Hence, the local environment must play an important role in determining the stability of these tyrosines and their functions.

The tyrosyl radicals have been studied extensively in proteins and model systems. The 9GHz EPR spectra of these radicals are remarkably varied[12] in principal, due to the fact that a strong β-proton hyperfine coupling, whose magnitude is determined by the orientation of the β-proton to the phenyl ring plane, dominates the appearance of the spectra. The EPR spectra of the RNR and PSII tyrosyl radicals are completely different from each other for this reason. Variations in the EPR spectra of tyrosyl radicals in mutants of PSII and RNR[13, 14] have been reported and attributed to changes in proton hyperfine couplings, reflecting structural changes. The electronic spin density distribution of tyrosyl radicals has been measured by ENDOR and by pulsed-EPR[15-17]. In PSII, these techniques have characterized the proximal protons to Tyr-D· which are likely candidates as hydrogen-bond donors[18].

For obtaining more information about the character and structure of these protein-bound radicals, comparison with the unperturbed model system is essential. By probing the hyperfine interactions of the unpaired electron with a particular nucleus with nonzero nuclear spin, electron paramagnetic resonance (EPR) and electron nuclear double resonance (ENDOR) spectroscopies are powerful tools for a detailed study of the electronic and nuclear structure of the in vitro tyrosyl radicals. From the obtained hyperfine coupling tensors, the spin density distribution of the unpaired π-electron can then be mapped. Also, determination of the electronic and nuclear structure of the tyrosine radicals is necessary to gain insight into the molecular mechanism of participation of protein-attached tyrosine-based radicals in enzyme catalyses. In principle, also the g-tensor would yield detailed information on the structure of the oxidized or reduced cofactors, but this information is much more difficult to extract because of the generally small anisotropies of the g-tensor of organic radicals.

The characterization by EPR and ENDOR spectroscopies of a model system containing a tyrosyl radical in a precisely known environment and orientation is of interest as it can help in interpreting the data collected for biological samples.

In this work we report a detailed X-band cw-EPR and ENDOR study on the tyrosyl radical produced by γ-irradiation of a single crystal of L-Tyrosine-Hydrochloride.

A model tyrosine radical obtained in γ-irradiated L-tyrosine hydrochloride single crystals has been studied by Fassanella and Gordy[19]. However, in that study only X-band EPR has been used, whereas only ENDOR can allow to obtain all the hyperfine tensors of the radical, and therefore to completely characterise the radical.

Material and Methods

Single crystals of L-Tyrosine-HCl were grown at room temperature by slow evaporation of a saturated solution of L-Tyrosine in concentrated HCl. The dimensions of the crystals used in this study were about 2x2x 4 mm. When the crystal was rotated about c axis six faces were observed (Fig. 1).

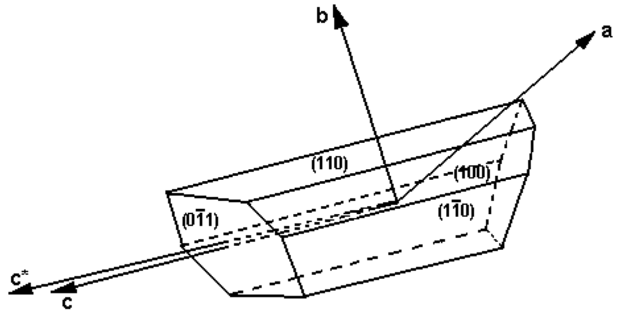

Fig.1. *Diagram of a single crystal of L-Tyrosine-HCl*

The angles between the faces (100), (110) and (110), (0$\bar{1}$1) were calculated from the unit cell dimensions and the values (129. 2° and 111. 4°, respectively) were compared with the ones measured by an optical goniometer.

The crystal structure has been obtained using X-ray diffraction methods[20] and then was subsequently refined using neutron diffraction methods[21].

L-Tyrosine-HCl crystallizes in the monoclinic space group $P2_1$, with cell parameters a=11. 083Å, b=9. 041Å, c=5. 099Å, β=91. 82° and two molecules per unit cell. The crystals were irradiated at room temperature by γ-rays from a ^{60}Co source with a dose of 6MRad.

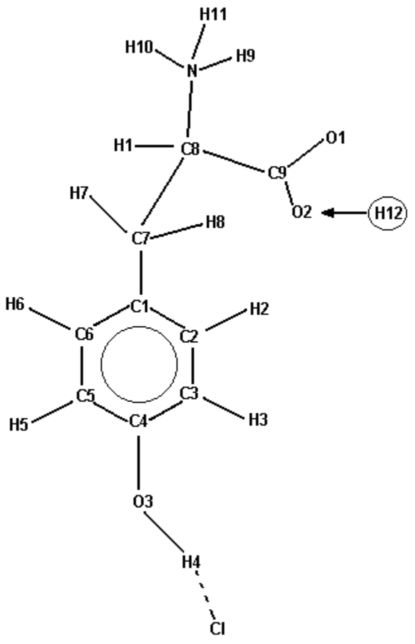

Fig.2. *Schematic drawing of the L-Tyrosine-HCl molecule*

The L-tyrosine hydrochloride molecule is shown schematically in Fig. 2. Detailed structural information about the L-Tyrosine-HCl molecule has been obtained from the neutron diffraction study[21] and it is summarized in Table I which lists vectors, interatomic distances, bond and dihedral angles which will be compared with the magnetic resonance data.

X-band EPR spectra were recorded at a frequency of 9. 4 GHz using a conventional Bruker ER200D spectrometer interfaced with a Bruker data system ESP1600 and equipped with a Bruker variable temperature unit.

Table 1

Direction cosines, bond lengths, bond angles and dihedral angles in L-Tyrosine-HCl molecule

Bond	a	b	c*	R(Å)
C1-C2	0.750	0.604	-0.271	1.393
C2-C3	0.862	0.012	0.507	1.394
C3-C4	0.110	-0.588	0.802	1.382
C4-C5	-0.741	-0.609	0.283	1.393
C5-C6	-0.853	-0.019	-0.522	1.391
C6-C1	-0.128	0.594	-0.794	1.393
C4-O3	0.835	-0.009	0.550	1.374
O3-H4	0.689	0.648	-0.325	0.988
C2-H2	-0.117	0.598	-0.793	1.074
C3-H3	0.747	0.598	-0.291	1.091
C5-H5	0.121	-0.591	0.798	1.086
C6-H6	-0.732	-0.617	0.288	1.091
C1-C7	-0.846	-0.021	-0.532	1.509
C7-C8	-0.793	0.349	0.499	1.536
C7-H7	-0.210	-0.934	-0.289	1.085
C7-H8	0.118	0.539	-0.835	1.080

Bond angles	
C8C7C1	113.5
C8C7H8	108.4
C8C7H7	107.7
H8C7C1	109.8
H8C7H7	106.6
C1C7H7	110.6
C7C1C2	120.2
C7C1C6	121.2
C2C1C6	118.5
C1C2H2	119.2
C1C2C3	121.0
C1C6C5	120.8
C1C6H6	120.1
C2C3C4	119.6
C6C5C4	119.7
C3C4C5	120.2

Dihedral angles	
C4C3C2C1	1.2
C5C4C3C2	1.2
C6C5C4C3	0.1
C7C1C6C5	179.3
C8C7C1C2	113.7
O3C4C5C6	179.8
NC8C7C1	178.1
H2C2C1C6	179.9
H3C3C4C5	179.0
H5C5C4C3	179.4
H6C6C1C2	179.7
H7C7C1C6	53.1
H8C7C1C2	7.9

Direction	a	b	c*	R(Å)
C1-C4	0.858	0.017	0.514	2.796
C2-C6	-0.361	-0.697	0.619	2.395
C3-C5	-0.366	-0.690	0.624	2.406
C1-H7	-0.701	-0.487	-0.521	2.146
C1-H8	-0.543	0.258	-0.800	2.133
PER(C4C3,C4C5)	-0.322	0.625	0.502	
PER(C1C4,C3C5)	0.365	-0.724	-0.586	
PER(PER(C4C3,C4C5),O3C4)	-0.348	-0.597	0.519	
PER(PER(C1C4,C3C5),C3H3)	0.561	-0.331	0.759	
PER(PER(C1C4,C3C5),C5H5)	-0.923	-0.362	-0.128	
PER(C5C6,C5C4)	0.323	-0.628	-0.506	
PER(PER(C5C6,C5C4),C5H5)	-0.800	-0.319	-0.115	
PER(C3C4,C3C2)	0.307	-0.635	-0.508	
PER(PER(C3C4,C3C2),C3H3)	0.488	-0.290	0.658	

Results and Discussions

On the basis of the comparison of our results with those derived from different studies in the tyrosyl radical[1, 15, 19, 22-27] we identified the free radical detected in γ-irradiated single crystal of L-Tyrosine-HCl with the phenoxyl radical reported in Fig. 3. This radical is formed by loss of the hydrogen atom from the hydroxyl group attached to the aromatic ring of the Tyrosine molecule.

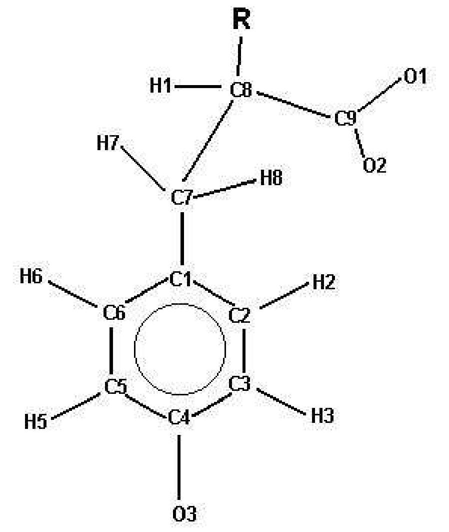

Fig. 3.*Tyrosyl radical formed in gamma-irradiated single crystal of L-Tyrosine-HCl.*

X-band cw-EPR

Due to the monoclinic structure of L-Tyrosine-HCl, two magnetically nonequivalent sites are present. Therefore, for any orientation of the crystal in the magnetic field, the spectrum is given by the superposition of the spectra due to the radicals in the two sites.

However, when the magnetic field is along a crystallographic axis or when it is in the crystallographic plane perpendicular to the binary axis, the two sites become magnetically equivalent.

The X-band cw-EPR spectra for the orientation of the magnetic field parallel to the b axis is given in Fig. 4. The dominant feature of this spectrum is a quintet spread over about 30G, with the amplitude distribution of the five lines in the 1:2:1:2:1 ratio, which can be interpreted in fact as a doublet of triplets, due to the interaction of the unpaired electron with three protons, two of them being almost equivalent. The spectral pattern vary little with angle, the intensity distribution of the five lines changing from 1:2:2:2:1 to 1:2:1:2:1 for certain orientations. The spectrum given in Fig. 4 shows also weaker resonance features in addition to those forming the basic quintet. These signals must be due to a second free radical formed by γ-irradiation of L-Tyr-HCl, as was also detected by Fasanella and Gordy who concluded that this species is unstable. This radical could be formed by hydrogen atom addition at a position ortho to the phenolic group of the tyrosine moiety, as it has been observed by Mezzetti et al. in N-Acetyl-L-Tyrosine[28].

In order to estimate the contribution of the second radical to the total EPR spectrum we have simulated the spectrum corresponding to B||b orientation (see Figure 4). The best agreement between the experimental and simulated spectrum in this case is obtained for a mixture of two radicals, whose concentrations are in the ratio 7. 3/1. The simulation parameters used for the first radical were obtained from the ENDOR results (see Table 2): A_1=12. 95G, A_2=A_3=5. 12G, ΔB_{pp}=3. 4G. In the second one, the unpaired electron is assumed to interact with four protons with isotropic hyperfine couplings: A_1=A_2=32G, A_3=5. 8G, A_4=10. 6G and ΔB_{pp}=3. 5G. The second set of parameters is attributed to a radical formed by hydrogen addition to the aromatic ring and it is comparable with that reported by Mezzetti et al. [28] for the neutral cyclohexadienyl radical in N-Acetyl-L-Tyrosine.

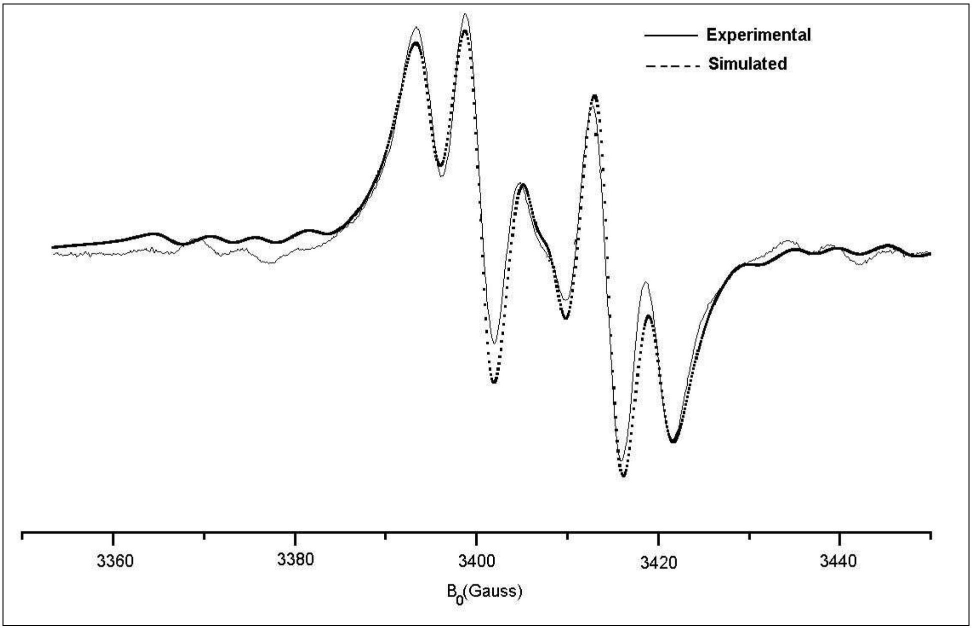

Fig.4. *X band cw-EPR spectrum of a L-Tyrosine-HCl single crystal oriented with the magnetic field parallel to the b axis.*

ENDOR

The ENDOR investigation has been done in the frequency range 2-35MHz, at 150K temperature.

We will consider in the following only proton ENDOR transitions. We will call high high-frequency ENDOR transitions ν_+ those given by $\nu_+=|A/2|+\nu_H$, where A is approximately the hyperfine splitting and ν_H the free proton frequency, and low-frequency ENDOR transitions ν_- are the ones given by $\nu_-=||A/2|-\nu_H|$. To attribute an ENDOR line to a ν_+ or ν_- frequency, we observed its radiofrequency shift corresponding to different values of the fixed external magnetic field. Depending on the positive or negative sign of the hyperfine coupling, the lines at frequency (ν_+, ν_-) will correspond respectively to the (m_s=-1/2, m_s=+1/2) or to the (m_s=+1/2, m_s=-1/2) electron spin manifolds. The ENDOR spectrum corresponding to the B||b orientation is given in Fig. 5 and the angular dependencies of the ENDOR lines observed in the 18-35MHz range by locking the external magnetic field in the center of the EPR spectrum are shown in Fig. 6.

Table 2.

Hyperfine coupling tensors for the phenoxyl radical in single crystals of L-Tyrosine-HCl γ-irradiated at room temperature and measured at 150K

Tensor	Principal values (MHz)	Isotropic value (MHz)	Dipolar principal values (MHz)	Direction cosines		
				a	b	c*
Tensor A'	-7.2		+9.5	0.0207	-0.6337	0.7733
(H5)	-18.2	-16.7	-1.5	0.3503	-0.7198	-0.5993
	-24.8		-8.1	0.9364	0.2832	0.2071
Tensor A	-7.5		+9.8	0.0154	-0.6634	0.7481
(H5')	-18.7	-17.3	-1.5	0.3410	-0.6999	-0.6276
	-25.5		-8.3	0.9399	0.2647	0.2154
Tensor B'	-6.9		+10.2	0.6379	0.6578	-0.4004
(H3)	-19.3	-17.3	-2.1	0.3497	-0.7107	-0.6104
	-25.6		-8.3	-0.6861	0.2494	-0.6434
Tensor B	-7.9		+9.9	0.6452	0.6750	-0.3579
(H3')	-19.1	-17.8	-1.3	0.3518	-0.6783	-0.6451
	-26.4		-8.6	-0.6782	0.2903	-0.6751
Tensor β	44.0		+3.9	-0.7504	-0.4884	-0.4454
(H7)	38.7	40.1	-1.4	-0.4227	0.8726	-0.2448
	37.6		-2.5	0.5082	0.0046	-0.8612
Tensor β'	39.2		+3.9	-0.7700	-0.4869	-0.4124
(H7')	33.8	35.3	-1.5	-0.3978	0.8717	-0.2863
	32.9		-2.4	0.4989	-0.0564	-0.8648
Tensor <A>	-7.35		9.63	0.0181	-0.6490	0.7606
	-18.43	-16.98	-1.45	0.3454	-0.7098	-0.6139
	-25.16		-8.18	0.9383	0.2738	0.2113
Tensor <B>	-7.42		10.11	0.6416	0.6664	-0.3792
	-19.19	-17.53	-1.66	0.3508	-0.6945	-0.6278
	-25.99		-8.46	-0.6822	0.2699	-0.6793
Tensor <β>	35.30		3.84	-0.7439	-0.5187	-0.4214
	36.66	37.89	-1.24	-0.4420	0.8548	-0.2718
	41.73		-2.60	0.5012	-0.0159	-0.8652

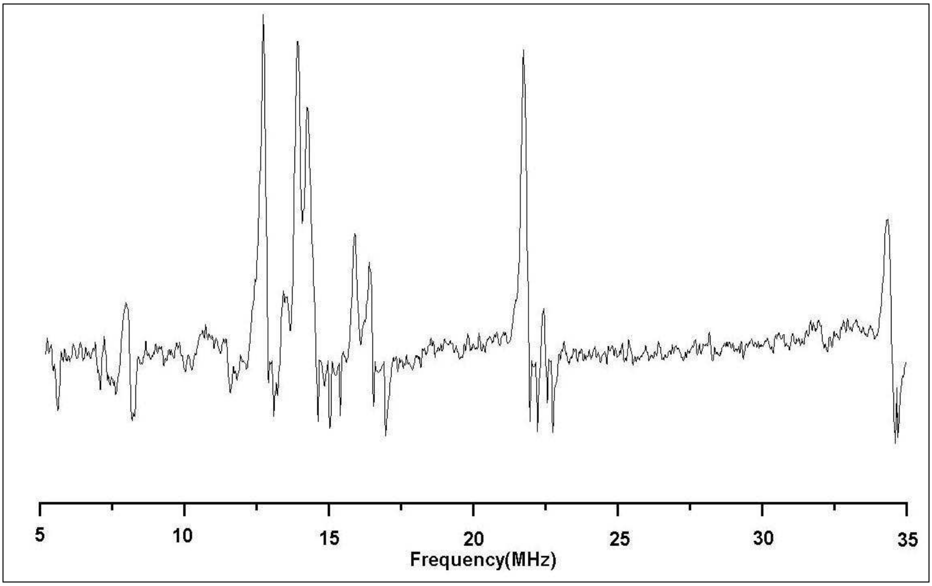

Fig. 5. *ENDOR spectrum of a L-Tyrosine-HCl single crystal oriented with the magnetic field parallel with the b axis and fixed to the centrum of the EPR spectrum.*

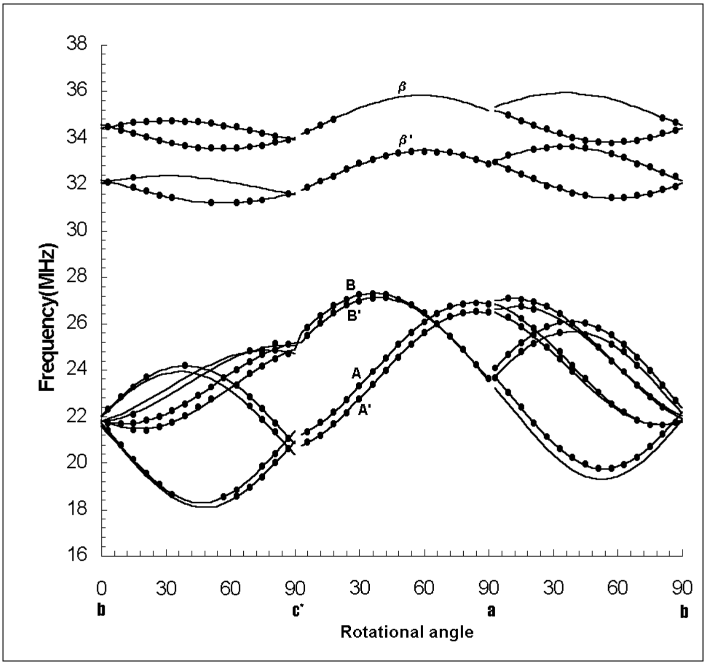

Fig. 6. *Angular dependencies of ENDOR frequencies in the three crystallographic planes: bc* plane; c*a plane; ab plane.*

They correspond to the rotation of the L-Tyrosine-HCl single crystal in the *bc**, *c*a* and *ab* planes, respectively. As it easily can be seen in Figure 6, the ENDOR lines in the 18-30 MHz radiofrequency range appear in closely matched pairs. This situation was not observed previously by Box and coworkers[26] in theirs ENDOR study on a γ-irradiated single crystal of Tyrosine-HCl at 4. 2 K. However, this doubling of the lines is clearly observed in our study in all the three planes and it could be a consequence of the absence in L-Tyrosine-HCl at 150K, of the crystallographic inversion center present at room temperature. Hence, there are essentially two molecules per unit cell, which are almost but not quite related by a center of symmetry and so, two identical free radicals, in slightly different conformations are found. A similar site doubling has been observed by McCalley and Kwiram in an ENDOR study at 4. 2K of the free radicals in malonic acid single crystals[29].

By usual first order analysis of the angular dependencies of the frequencies corresponding to the A, A’, B and B’ lines in the three crystallographic planes (Fig. 6) we have obtained a set of 6 hyperfine coupling tensors, reported in Table 2. The antiaxiality of the dipolar principal values of all these four tensors is typical for α protons. However, both their dipolar values and isotropic hyperfine coupling constants are smaller than those for an α-proton bonded to a carbon atom with spin density $\rho=1$ in a π-radical (about -30, -60 and -90 MHz). The small principal values of the dipolar tensors are explained by the unpaired spin delocalization on a conjugated π-system.

On the basis of the comparisons of the principal directions of the tensors A-B with C3-H3 and C5-H5 directions in the undamaged molecule, we attributed to the ring proton 5 the tensors A and A' and to the ring proton 3 the tensors B and B'. For α-protons, both experimentally and by molecular orbital calculations it was demonstrated that for the three principal absolute values of the hyperfine coupling tensors, the minimum ${}^{\alpha}A_x$ occurs when the external magnetic field H_0 is parallel to the ${}^{\alpha}$H-C bond, the intermediate ${}^{\alpha}A_z$ occurs when H_0 is parallel to the lone electron orbital (LEO) symmetry axis and the maximum ${}^{\alpha}A_y$ occurs when H_0 is normal to the ${}^{\alpha}$H-C bond and to the LEO axis. The isotropic component ${}^{\alpha}a$ is negative and therefore, the corresponding dipolar elements B_x, B_y and B_z are such that the B_x is most positive and B_y is most negative. In Table 3 are given the calculated angles between the principal directions of the four hyperfine tensors with selected directions in L-Tyrosine-HCl molecule as obtained from neutron diffraction data (see Table 1). From these data it can easily be seen that both conformations of the phenoxyl radical formed in γ-irradiated L-Tyrosine-HCl at the C3 and C5 carbon sites are very close to the original conformation of the parent molecule.

On the basis of the comparisons of the principal directions of the tensors A-B with C3-H3 and C5-H5 directions in the undamaged molecule, we attributed to the ring proton 5 the tensors A and A' and to the ring proton 3 the tensors B and B'. For α-protons, both experimentally and by molecular

orbital calculations it was demonstrated that for the three principal absolute values of the hyperfine coupling tensors, the minimum $^{\alpha}A_x$ occurs when the external magnetic field H_0 is parallel to the $^{\alpha}$H-C bond, the intermediate $^{\alpha}A_z$ occurs when H_0 is parallel to the lone electron orbital (LEO) symmetry axis and the maximum $^{\alpha}A_y$ occurs when H_0 is normal to the $^{\alpha}$H-C bond and to the LEO axis. The isotropic component $^{\alpha}a$ is negative and therefore, the corresponding dipolar elements B_x, B_y and B_z are such that the B_x is most positive and B_y is most negative. In Table 3 are given the calculated angles between the principal directions of the four hyperfine tensors with selected directions in L-Tyrosine-HCl molecule as obtained from neutron diffraction data (see Table 1). From these data it can easily be seen that both conformations of the phenoxyl radical formed in γ-irradiated L-Tyrosine-HCl at the C3 and C5 carbon sites are very close to the original conformation of the parent molecule.

The hyperfine coupling tensors of the protons bonded to the C2 and C6 atoms have not been determined due to the overlap of their ENDOR lines with those of the matrix proton.

The hyperfine coupling tensors with the largest isotropic coupling constants (tensors β and β' in Table 2) have been attributed to one of the methylene protons of the radical. These tensors are typical for β-protons, attached to a carbon atom one bond length away from the carbon atom bearing the unpaired electron. The direction corresponding to the largest dipolar part of a β-proton hyperfine coupling tensor should lie parallel to the C_{α}-H_{β} direction. The angle between $\langle\beta_x\rangle$ and C1H7 direction in the undamaged molecule is 6. 5° (5. 2 and 7. 4 for β_x and β'_x, respectively).

In radicals of the type Ar-CH_2-R the couplings of the β-methylene protons are angle dependent. The isotropic part of a β-proton tensor is given[30] by:

$$A_{iso}=\rho_{\pi}Q_{\beta}(\theta)=\rho_{\pi}(B_0+B_2\cos^2\theta) \quad (1)$$

where ρ_{π} is the unpaired spin density on the carbon atom bearing the odd electron (C_{α}), θ is the dihedral angle between the plane containing the C_{β}-H_{β} bond and the plane containing the symmetry axis of the p_{π} orbital of the C_{α} atom (each plane also contains the Cα-Cβ bond).

B_2 constant represents the isotropic coupling resulting from the maximum exchange of the unpaired spin density with H_{β} through hyperconjugation of the C_{α} p_{π}-orbital and C_{β} p-orbital component involved in the C_{β}-H_{β} bonding orbital. Maximum hyperconjugative coupling occurs when the dihedral angle between C_1-C_{β}-H_{β} and the p_{π}-orbital is 0°. As θ increases, the component of the C_{β}-H_{β} bonding orbital along the p_{π}-orbital axis decreases. Subsequently, the degree of the hyperconjugation coupling, and hence the isotropic interaction, decreases as $\cos^2\theta$. In the calculations, a value of 162MHz is assumed for B2 constant, which was estimated from the isotropic coupling of freely rotating β-methylene protons in aliphatic radicals in solution[30].

Table 3.

Orientation of the principal axes of tensors A-B with respect to the same selected directions in the undamaged molecule

Directions*	Angle
A_x,C5H5	7.9
A_z,Pr	3.0
A_y,Prb5	7.6
A_x',C5H5	6.4
A_z',Pr	1.0
A_y', Prb5	6.5
B_x,C3H3	8.3
B_z,Pr	4.3
B_y,Prb3	8.7
B_x',C3H3	9.5
B_z',Pr	1.7
B_y',Prb3	17.2
$<A_x>$,C5H5	7.1
$<A_z>$,Pr	2.0
$<A_y>$,Prb5	7.0
$<B_x>$,C3-H3	8.9
$<B_z>$,Pr	3.2
$<B_y>$,Prb3	9.2

* Pr is the direction perpendicular to the ring, defined as the perpendicular to the C1C4 and C3C5 directions (PER(C1C4,C3C5) in Table 1).
Prb5 is the direction perpendicular to the ring and to the C5H5 direction (PER(PER(C1C4,C3C5),C5H5) in Table 1).
Prb3 is the direction perpendicular to the ring and to the C3H3 direction (PER(PER(C1C4,C3C5),C3H3) in Table 1).

The B_0 term includes the small non-hyperconjugative contributions, its value being about 4-7% of B_2. Therefore, B_0 is commonly neglected in practical applications of equation (1), leading to the following expression:

$$A_{iso}=\rho_\pi B_2\cos^2\theta \qquad (2)$$

The unpaired spin density pattern of the phenoxyl type radicals is almost independent of the environment so that it is usually assumed a value of 63 MHz for the $\rho_\pi B_2$ quantity[28]. With this value, from equation (2) we found the dihedral angles corresponding to the two conformations of the radical: 37. 1^o and 41. 5^o (average 39. 3^o). These values are very close to the dihedral angle defined by the C_7H_7, C_1 and the perpendicular direction to the phenolic ring in the undamaged molecule, which is 36. 9^o (see Fig. 7).

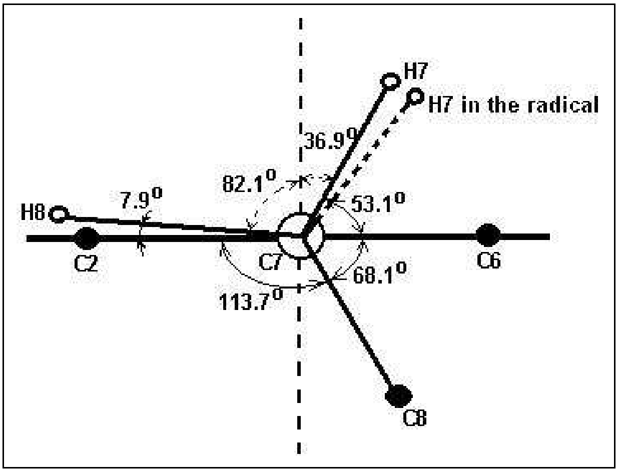

Fig.7. *Dihedral angles involving the methylene protons in L-Tyrosine-HCl molecule*

On the other hand, because the isotropic hyperfine coupling constant of the other β-methylene proton of the radical must be very small because it is not detectable in the ENDOR and EPR spectra, the corresponding dihedral angle formed by the C_7-$H_{\beta 2}$ (C_7-H_8 in the molecule) bond must be close to 90^o. In fact, in the undamaged molecule this dihedral angle is 82. 1^o. This means that also this bond direction is almost not affected when the free radical is formed. On the basis of these comparisons we can conclude that the conformation of the radical and that of the undamaged molecule at the C1 and C7 sites are nearly the same.

It is possible now to estimate the C1-H7 distance in the point dipole approximation. The largest anisotropic component of the β proton coupling tensor is given by[31]:

$$B^{H_\beta}_{max}(\text{MHz}) = 157.8\rho^{\alpha}_{\pi}/r^3(\text{Å}) \qquad (3)$$

Using the value 0. 38 for the unpaired spin density on C_1 atom, from the above equation the distance C_1-H_7 is found to be 2. 499Å, which means that in the radical this distance is 0. 35Å lengthened with respect to the undamaged molecule.

Conclusions

Immediately after irradiation, the EPR spectra of the γ-irradiated single crystal of L-Tyrosine-HCl show the presence of two different radicals. One of them gives rise to an EPR spectral pattern which vary little with angle, the dominant feature being the five center lines spread over 25-30G according to the orientation. These signals are due to the tyrosyl radical which, by ENDOR analysis at 150K, was found to be present in two slightly different conformations.

The α and β proton hyperfine couplings tensors of the tyrosyl radical suggest very small changes in the geometry and conformation with respect to the undamaged molecule.

The other EPR signals are due to a second radical which disappeared after a few days. This kind of radical has been also observed in other systems and it is supposed that the radical responsible for these features could be a neutral cyclohexadienil radical, as found in similar systems.

Acknowledgements

This work has been possible due to a research fellowship performed under the CNR-NATO Outreach Fellowships programme of the Italian National Council of Research and it has been performed at the "Universita Degli Studi di Padova, Dipartimento di Chimica Fisica.

REFERENCES

1. R. J. Hulsebosch, J. S. van den Brink, S. A. M. Nieuwenhuis, P. Gast, J. Raap, J. Lugtenburg, A. J. Hoff, *J. Am. Chem. Soc.,* **119**, 8685-8694 (1997).
2. P. Reichard, A. Ehrenberg, *Science*, **221**, 514-519 (1983).
3. R. Karthein, R. Dietz, W. Nastainczyk, H. H. Ruf, *Eur. J. Biochem*, **171**, 313-320 (1988).
4. B. A. Barry, G. T. Babcock, *Proc. Natl. Acad. Sci. USA*, 84, 7099-7103 (1987).
5. P. Allard, A. L. Barra, K. K. Anderson, P. P. Schmidt, M. Atta, A. Graslund, *J. Am. Chem. Soc.,* 118, 895-896 (1996).
6. R. J. Boerner, B. A. Barry, *J. Biol. Chem.,* **269**, 134-137 (1994).
7. M. M. Whittaker, J. W. Whittaker, *J. Biol. Chem.,* **265**, 9610-9613 (1990).
8. S. M. Jones, D. Mu, D. Wemmes, A. J. Smith, S. Kaus, D. Maltby, A. L. Burlingame, J. R. Kinman, *Science*, **248**, 981-987 (1990).
9. A. Ivancich, H. M. Jouve, J. Gaillard, *J. Am. Chem. Soc*., **118**, 12852-12853 (1996).

10. A. Ivancich, H. M. Jouve, B. sartor, J. Gaillard, *Biochemistry*, **36**, 9356-9364 (1997).
11. S. V. Ruffle, D. Donnelly, T. L. Blundell, J. H. A. Nugent, *Photosyn. Res.,* **34**, 287-300 (1992).
12. C. Galli, M. Atta, K. K. Anderson, A. Graslund, G. W. Brudwig, *J. Am. Chem. Soc.,* **117**, 740-746 (1995).
13. C. Tommos, C. Madsen, S. Styring, W. F. J. Vermas, *Biochemistry*, **33**, 11805-11813 (1994).
14. M. Ormo, K. Regnstrom, Z. Wang, Q. Lawrence, M. Sahlin, B. M. Sjoberg, *J. Biol. Chem.,* **270**, 6570-6576 (1995).
15. S. E. J. Rigby, J. H. A. Nugent, P. J. O'Malley, *Biochemistry,* **33**, 1734-1742 (1994).
16. C. J. Bender, M. Sahlin, G. T. Babcock, B. A. Barry, T. K. Chandrashekar, S. P. Salowe, J. Stubbe, B. Lindstrom, L. Petersson, A. Ehrenberg, B. M. Sjoberg, *J. Am. Chem. Soc*., 111, 8076-8083 (1989).
17. K. Warncke, G. T. Babcock, J. McCracken, *J. Am. Chem. Soc.,* **116**, 7332-7340 (1994).
18. X. S. Tang, D. A. Chisholm, G. C. Dismukes, G. W. Brudvig, B. A. Diner, *Biochemistry*, **32**, 13742-13748 (1993).
19. E. L. Fasanella, W. Gordy, *Proc. Natl. Acad. Sci. USA*, **62**, 299-304 (1969).
20. R. Srinivasan, Proc. Indian Acad. Sci., A50:19-26, 1959.
21. M. N. Frey, T. F. Koetzle, M. S. Lehman, W. C. Hamilton, *J. Chem. Phys.,* **58**, 2547-2556 (1973).
22. C. W. Hoganson, N. Lydakis-Simantiris, X. S. Tang, C. Tommos, K. Warncke, G. T. Babcock, B. A. Diner, J. McCracken, S. Styring, *Photosynth. Res.,* **46**, 177-184 (1995).
23. C. Tommos, X. S. Tang, K. Warncke, C. W. Hoganson, S. Styring, J. McCracken, B. A. Diner, G. T. Babcock, *J. Am. Chem. Soc.,* **117**, 10325-10335 (1995).
24. S. A. M. Nieuwenhuis, R. J. Hulsebosch, J. Raap, P. Gast, J. Lugtenburg, A. J. Hoff, *J. Am. Chem. Soc.,* **120**, 829-830 (1998).
25. S. Un, M. Atta, M. Fontecave, A. W. Rutherford, *J. Am. Chem. Soc.,* **117**, 10713-10719 (1995).
26. H. C. Box, E. E. Budzinski, H. G. Freund, *J. Chem. Phys.,* **61**, 2222-2226 (1974).
27. K. Warncke, J. McCracken, *J. Chem. Phys.,* **103**, 6829-6840 (1995).
28. A. Mezzetti, A. L. Maniero, M. Brustolon, G. Giacometti, L. C. Brunel, *J. Phys. Chem. A,* **103**, 9636-9643 (1999).
29. R. C. McCalley, A. L. Kwiram, J. Phys. Chem., 97, 2888-2903 (1993).
30. R. W. Fessenden, R. H. Schuler, *J. Chem. Phys.,* **9**, 2147-2195 (1963).
31. J. Hutterman, G. Schmidt, D. Weimann, J. Mag. Res., 21, 221 (1976).

STUDIA UNIVERSITATIS BABEŞ-BOLYAI, PHYSICA, XLVII, 1, 2002

NUCLEAR MAGNETIC RESONANCE INVESTIGATION OF BISMUTH-BORATE GLASSES

S. SIMON[1], M. VASILESCU[1]

ABSTRACT. Bismuth-borate glasses belonging to $x\mathrm{Bi_2O_3}\cdot(100-x)\mathrm{B_2O_3}$ system, $0 \le x \le 93$, doped with 0.5 mol % MnO are investigated by magic angle spinning nuclear magnetic resonance (MAS NMR). The ^{11}B MAS NMR results indicate the presence of tetra coordinated boron in all investigated bismuth borate glasses, with a large maximum in the range $20 \le x \le 60$. The mean values of the NMR parameters like chemical shift, asymmetry parameter and quadrupolar coupling constant are less influenced by the bismuth/boron ratio, showing that boron structural units are relatively stable on entire investigated composition range.

Introduction

Glasses containing bismuth attracted much attention due to their physical properties that make them important candidates for applications in high-energy physics [1-3] and nonlinear optics [4, 5]. In order to synthesize glasses suitable for such applications it is necessary to correlate the local structure of these glasses with their macroscopic behaviour.

Because of the small field strength of $\mathrm{Bi^{3+}}$ ions bismuth oxide cannot be considered as vitreous network former, despite the fact that the polymorphism of $\mathrm{Bi_2O_3}$ [6] is an indication that $\mathrm{Bi^{3+}}$ ions are easy to be integrated in disordered systems. However bismuthate glasses without conventional glass formers, can be obtained in large composition ranges [7], this behaviour being attributed to the high polarisability of $\mathrm{Bi^{3+}}$ cations [8].

Taking into account that boron has the nuclear spin $I = 3/2$ and as consequence of its quadrupolar moment it is a very efficient source of information by means of nuclear magnetic resonance (NMR) [9] about the local order around the glass network former.

In order to understand the role of bismuth in glasses formed with unconventional glass network formers it is important to know its role in systems with conventional glass network formers like boron oxide.

Oxide systems containing transition metal ions like manganese ions are interesting because of their possible applications in threshold and memory switching [10-12] and can be studied also by electron paramagnetic resonance [13–15].

---

[1] *Babes-Bolyai University, Faculty of Physics, 3400 Cluj-Napoca, Romania*

Experimental

The investigated bismuth-borate system $99.5[xBi_2O_3\cdot(100\text{-}x)B_2O_3]$ 0.5MnO (mol%) was explored in the composition range $0 \le x \le 93$. The glasses were obtained by mixing $Bi(NO_3)_3\cdot H_2O$, H_3BO_3 and MnO of reagent grade purity, in desired proportion, melting in alumina crucibles at 1100°C for 10 minutes, followed by quickly undercooling at room temperature by pouring onto stainless steel plates.

The ^{11}B MAS-NMR measurements were carried out at room temperature on Chemagnetics Infinity 600 MHz spectrometer equipped with a solid-state accessory, with MAS frequency of 15 kHz.

Results and discussion

^{11}B MAS NMR spectra of investigated bismuth borate glasses are presented in Figure 1. For all samples, excepting pure boron oxide glass, there are contribution from both boron species: planar three-coordinated boron that gives the peak centered around 12 ppm and pyramidal coordinated boron that gives the peak at about –1 ppm.

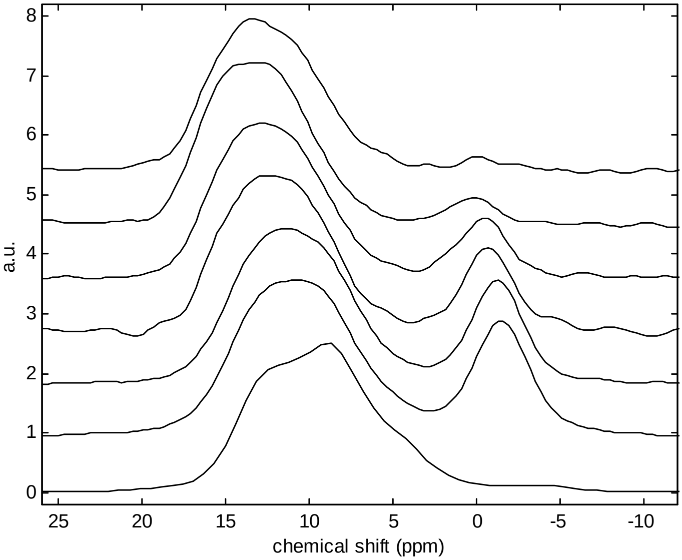

Fig. 1. *^{11}B MAS NMR spectra of glass samples*

In order to determine the NMR parameters and the fraction of tetra-, respectively of three coordinated species the experimental ^{11}B MAS NMR spectra were simulated by using a MATLAB NMR program. Figure 2 shows the result of simulating procedure for MAS NMR spectrum of $99.5[60Bi_2O_3\cdot 40B_2O_3]0.5MnO$ sample. A good agreement between experimental and simulated spectra for all samples containing bismuth were obtained by taking into account only two types os sites for boron: three-coordinated and tetra-coordinated.

In the case of sample without bismuth (x =0) for which only the peak around 11 ppm appears, it was necessary to consider two three coordinated species.

The composition dependence of NMR parameters as chemical shift (δ), asymmetry parameter (η) and quadrupolar coupling constant (Q_{cc}) are given in Figures 3, 4 and 5 respectively. The lines are guides to eye.

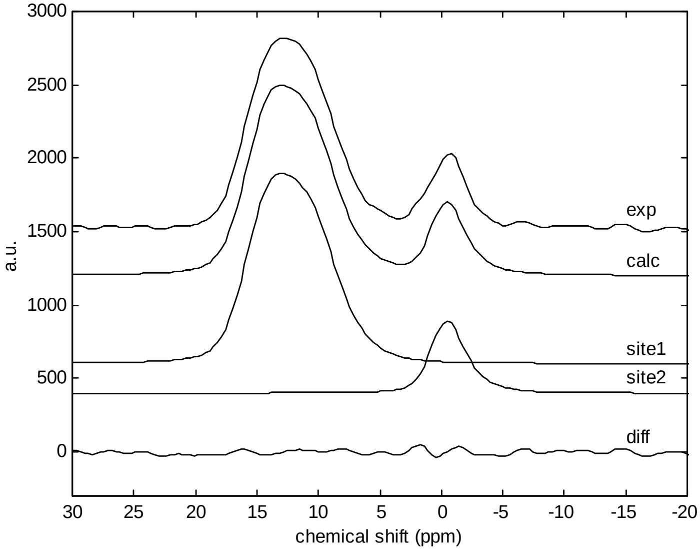

Fig. 2. *Deconvolution of ^{11}B MAS NMR spectrum for the glass sample with x = 67.*

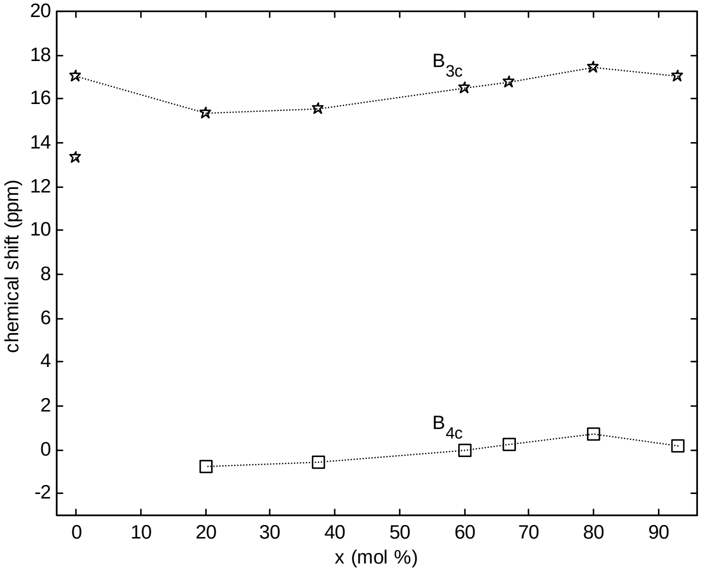

Fig. 3. *Composition dependence of the chemical shift.*

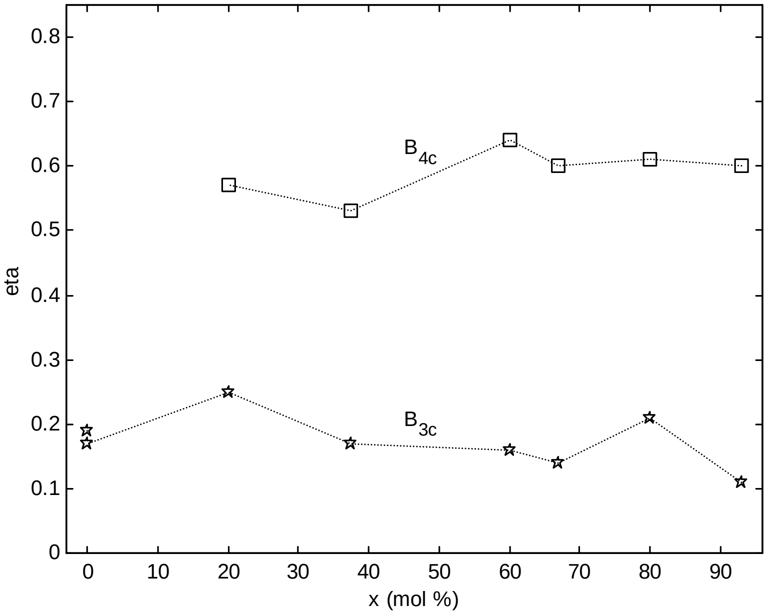

Fig. 4. *Composition dependence of the asymmetry parameter.*

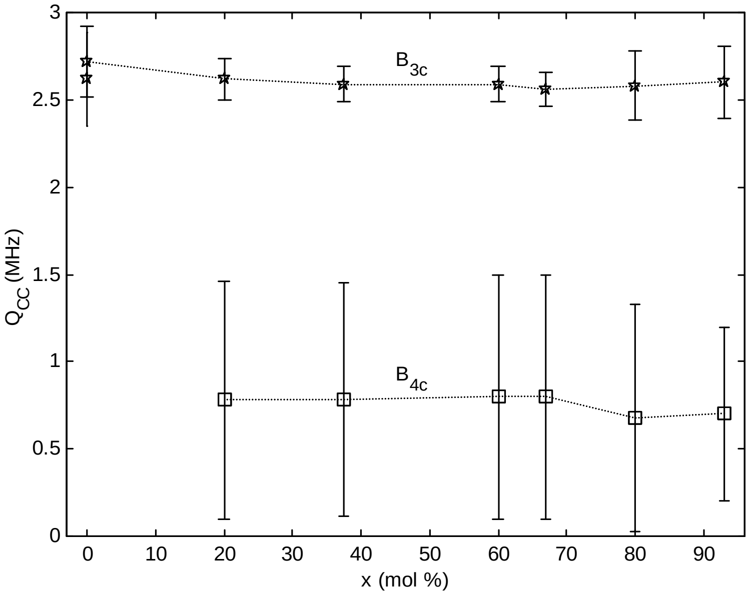

Fig. 5. *Composition dependence of the quadrupolar coupling constant.*

One remarks that due to the contrary shift effect of quadrupolar interaction on the peak position [16] the real values of chemical shift parameter are larger than those directly extracted from the peaks position in the MAS NMR spectra, particularly for the three-coordinated species.

As a general feature it is observed that the values of all three NMR parameters are weekly dependent on the glass composition denoting that the surrounding of the boron atoms is relatively stiff. From Figure 5 is observed that there is a larger distribution of quadrupolar coupling constant around tetra coordinated species (≈1.4 MHz) than around three coordinates ones (≈0.4 MHz), in agreement with the much softer arrangement of oxygens belonging to the tetra coordinated borons [17].

The composition dependence of the relative intensity of the two boron species is presented in Figure 6. The lines are guides to the eye. As expected there is an increase of the fraction of tetra-coordinated species by adding bismuth oxide to the borate matrix. The addition of oxygen to the pre-existing three coordinated boron units yields a conversion to the tetragonal forms [9]. Our results show a broad maximum for the relative intensity of the line assigned to the tetra coordinated boron, extended above the compositional region investigated by continuous wave NMR [17]. It was suggested, based on infrared spectroscopy results [18], that for x > 60 mol% there are only three-coordinated species. Even at very low concentration of boron oxide (7 mol %) the tetra coordinated species are still present in the glass sample. Having in view the results obtained in this study the proposed structural characteristics of the bismuth borate glasses in the high bismuth region must be reconsidered and a tetra-coordinated boron have to be included.

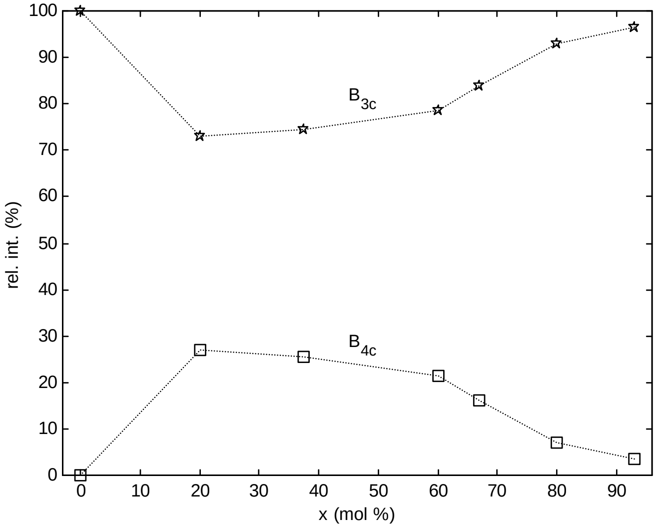

Fig. 6. *Composition dependence of the relative intensities of the peaks asigend to three-and tetra-coordinated boron atoms.*

Conclusions

^{11}B MAS NMR spectra of the studied bismuth-borate glasses show that up to 93 mol % Bi_2O_3 both three-coordinated boron the tetra-coordinated boron units are present. The composition dependence of tetra-coordinated boron fraction exhibits a large maximum in the region between 20 and 60 mol % Bi_2O_3. The NMR parameters obtained by simulation of recorded spectra confirm the relative stability of the boron surroundings in all investigated samples. The planar three-coordinated boron units seems to be less affected by the bismuth content than pyramidal tetra-coordinated boron units. For these species the range of coupling constant distribution are much larger than for the triangular units denoting that the tetra coordinated boron surrounding is much easier to be distorted and accommodated with the matrix structure.

The structural modeling to be developed for the bismuth borate glasses should take into account the presence of tetra-coordinated boron on entire composition range where the glasses are formed by quickly undercooling of the oxide melts.

Aknoledgements

The authors are greatful to Professor A. P. M. Kentgens from University of Nijmegen, The Netherlands, for access to 600 MHz spectrometer for MAS-NMR measurements.

REFERENCES

1. S. E. van Kirk, S. W. Martin, J. Am. Ceram. Soc., 75, 4, 1028 (1992).
2. N. Ford, D. Holland, Glass Technol., 28, 2, 106 (1987).
3. C. Stehle, C. Vira, D. Hogan, S. Feller, M. Affatigato, Phys. Chem. Glasses, 39, 2, 836 (1998).
4. W. H. Dumbaugh, Phys. Chem. Glasses, 27, 3, 119 (1986).
5. D. W. Hall, M. A. Newhouse, N. F. Borelli, W. H. Dumbaugh, D. L. Weidman, Appl. Phys. Lett., 54, 1293 (1989).
6. H. A. Harwig, Z. Anorg. Allg. Chem., 444, 151 (1978).
7. Y. Dimitriev, R. Iordanova, D. Klissurski, M. Milanova, Proc. Int. Congr. Glass, Edinburgh, Scotland, 1-6 July 2001, vol. 2, p. 883.
8. K. Fajans, N. Kreidl, J. Am. Ceram. Soc., 31, 105 (1948).
9. P. E. Stallworth, P. J. Bray, in Glass Science and Technology, Eds. D. R. Uhlman and N. J. Kreidl, vol. 4B, Academic Press, Boston, 1990, p. 77-145.
10. P. H. Gaskell, Mineral. Mag,. 64, 3, 425 (2000).

11. J. Livage, J. P. Jolivet, E. Tronc, J. Non-Cryst. Solids, 121, 35 (1990).
12. A. Gosh, J. Appl. Phys., 64, 2652 (1988).
13. I. Ardelean, M. Peteanu, S. Simon, V. Simon, F. Ciorcas, C. Bob, S. Filip, Indian J. of Physics, 74A, 5, 467 (2000).
14. I. Ardelean, M. Peteanu, S. Filip, V. Simon, G. Gyorffy, Solid State Commun. 102, 4, 341 (1997).
15. R. Stefan, S. Simon, Mod. Phys. Lett. B, 15, 3, 111 (2001).
16. S. Simon, G. J. M. P. van Moorsel, A. P. M. Kentgens, E. de Boer, Solid State NMR, 5, 163 (1995).
17. S. Greenblatt, Doctoral Thesis, Brown University, 1965.
18. N. Mochida, K. Takahashi, J. Ceram. Soc. Jpn, 84, 9, 413 (1976).

STUDIA UNIVERSITATIS BABEŞ-BOLYAI, PHYSICA, XLVII, 1, 2002

EPR AND MAGNETIC SUSCEPTIBILITY STUDIES OF $70TeO_2 \cdot 25B_2O_3 \cdot 5SrO$ GLASSES CONTAINING Cr^{3+} IONS

I. ARDELEAN[1], M. PETEANU[1], N. MUREŞAN[1]

ABSTRACT. Electronic paramagnetic resonance and magnetic susceptibility measurements revealed the chromium ions distribution and interactions involving them in $xCr_2O_3 \cdot (100-x)[70TeO_2 \cdot 25B_2O_3 \cdot 5SrO]$ glasses within $0 < x \leq 10$ mol %. The only detected valence state was Cr^{3+}. Depending on the Cr_2O_3 content of samples the preponderance of Cr^{3+} ions identified as isolated in strongly distorted octahedral symmetric sites, or associated in exchange coupled pairs was pointed out.

Introduction

Tellurite galsses containing transition metal ions are subject of study due to their interesting properties having number of applications [1-5]. There are tehnological reasons for which the local order in such vitreous systems is to be taken into account. Paramagnetic ions used as probes in EPR experiments supply information about the local site symmetry, the fine structure parameters of the EPR absorption spectra being very sensitive to the local structure. Data concerning the EPR of Cr^{3+} ions in tellurite vitreous systems are relatively poor and may explain our interest to complete them [6-8]. The available data reporting EPR of Cr^{3+} ions concern mainly borate [9, 10], boro-sulphate [11], phosphate [12, 13], bismuth-germanate [14] or fluoride [15-18] glasses. Depending on the Cr_2O_3 content of the glass, the Cr^{3+} ions were detected as isolated in strongly distorted octahedral symmetric sites subjected to strong crystal field effects, or associated in exchange coupled pairs. In some vitreous materials Cr^{5+} species were also detected [10, 19-22].

This paper aims to present our results obtained by means of EPR and magnetic susceptibility measurements on TeO_2-B_2O_3-SrO glasses containing chromium ions.

Experimental

Glasses of the system $xCr_2O_3 \cdot (100-x)[70TeO_2 \cdot 25B_2O_3 \cdot 5SrO]$ were obtained from reagent grade purity Cr_2O_3, TeO_2, H_2BO_3 and $SrCO_3$ used as starting material. The melting was performed in electric furnace at 1000^oC, during 6 min., using sintered corundum crucibles. The quenching at room

---

[1] *Faculty of Physics, Babes-Bolyai University, 3400 Cluj-Napoca, Romania*

temperature was achieved by pooring the molten material on stainless-stell plate. The samples structure was tested by means of X-ray diffraction, selecting the range of concentration for which the difractograph did not reveal any crystalline phase. Typical glasses were obtained for $0 \leq x \leq 10$ mol % Cr_2O_3.

EPR absorption spectra were recorded at room temperature using a JEOL-type spectrometer, in the X frequency band (9. 4 GHz) and 100 kHz field modulation.

Magnetic susceptibility measurements were obtained using a Faraday-type balance, in the 80-300 K temperature range.

Results and Discussion

EPR data

All the investigated samples show EPR absorption spectra due to $Cr^{3+}(3d^3)$ paramagnetic ions. Some representative spectra are presented in Fig. 1 to reveal the spectrum structure dependence upon concentration. Mainly, the absorption line consists in two signals centered at $g \approx 4.8$ and $g \approx 1.97$ respectively. Accidental Fe^{3+} impurities give the narrow signal at $g \approx 4.3$ (Fig. 1). According to theory [14] the low field resonances may be attributed to isolated Cr^{3+}ions in distorted sites characterized by large zero field splitting of the ground state energy level. Consequently, we explain the $g \approx 4.8$ absorptions in our spectra as arising from isolated Cr^{3+} ions subjected to strong orthorhombic crystalline field in a distorted octahedral environment. Due to the fine structure parameters distribution the signal is broadened showing the superposition of contributions from sites with slightly different axial distortions. As a background of this signal there is a broadener one, centered at a $g \approx 4.0$ due to Cr^{3+} ions in sites with a predominantly axial character. Both signals are components of an anisotropic absorption line, with corresponding signals at $g \approx 2.0$ too. Therefore, at least for small concentrations, the high-field absorption line show the superposition of signals at $g \approx 2.0$ and $g \approx 1.97$ (Fig. 1). As the Cr^{3+} ions concentration increases, the isolated ion vicinity is progressively altered and looses its well defined symmetry. Consequently, the structural units involving Cr^{3+} ions in sites of strong crystalline field become less represented, the corresponding absorption intensity decreases and the line progressively vanishes.

The main feature of the spectrum for samples with $x \geq 1$ mol % Cr_2O_3 is the high-field resonance signal at $g \approx 1.97$. Its evolution was followed in the concentration dependence of the EPR parameters, i. e. the peak-to-peak line-width ΔB, and the intensity approximated by $I = a \cdot (\Delta B)^2$ where a denotes the line-amplitude (height). These dependencies are presented in Figs. 2 and 3. In contrast with low-field signal, the intensity of the $g \approx 1.97$ one gradually increases with the Cr_2O_3 sample's content (Fig. 2). The line-width decreases showing exchange interaction narrowing as result of cluster association of Cr^{3+} ions. One may notice that the linewidth reaches smaller values than those corresponding to $xCr_2O_3{\cdot}(100\text{-}x)$ $[70TeO_2{\cdot}25B_2O_3{\cdot}5SrF_2]$ glasses prepared in similar conditions [23]. This suggests more intense interactions between Cr^{3+} ions for glasses containing oxygen ligand ions than those corresponding to matrices where oxygen was partially replaced by fluorine.

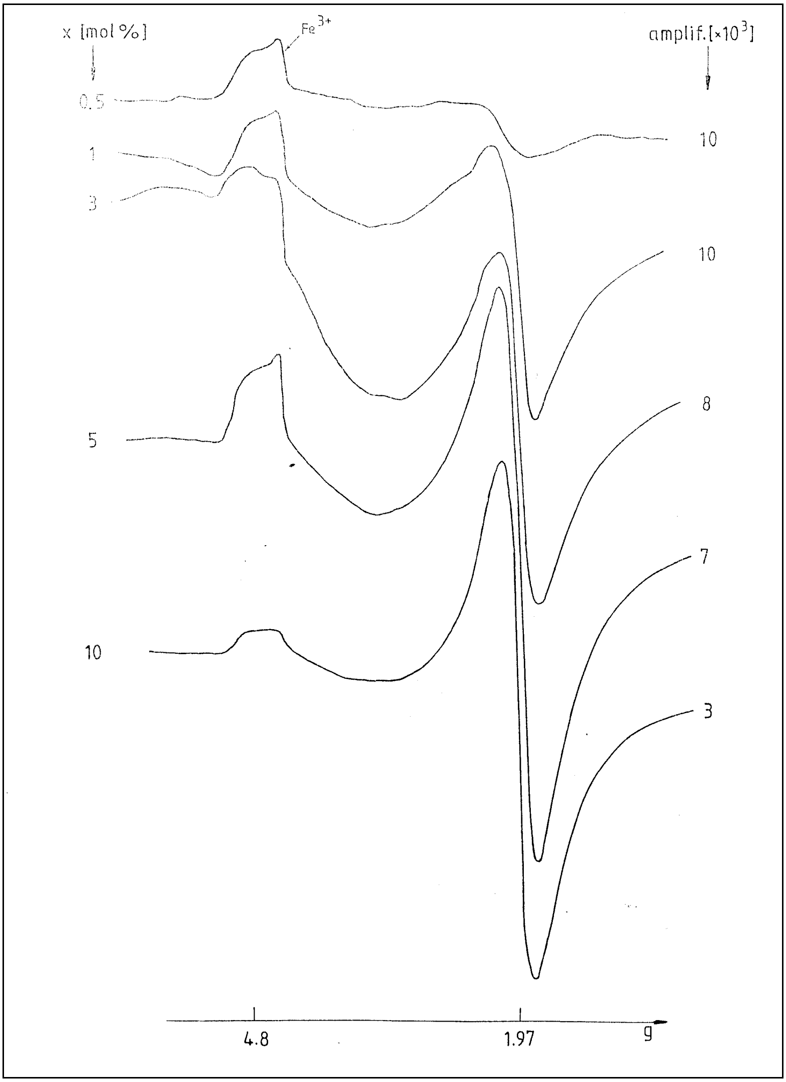

Fig. 1. *EPR absorption spectra of Cr^{3+} ions in $xCr_2O_3{\cdot}(100\text{-}x)[70TeO_2{\cdot}25B_2O_3{\cdot}5SrO]$ glasses.*

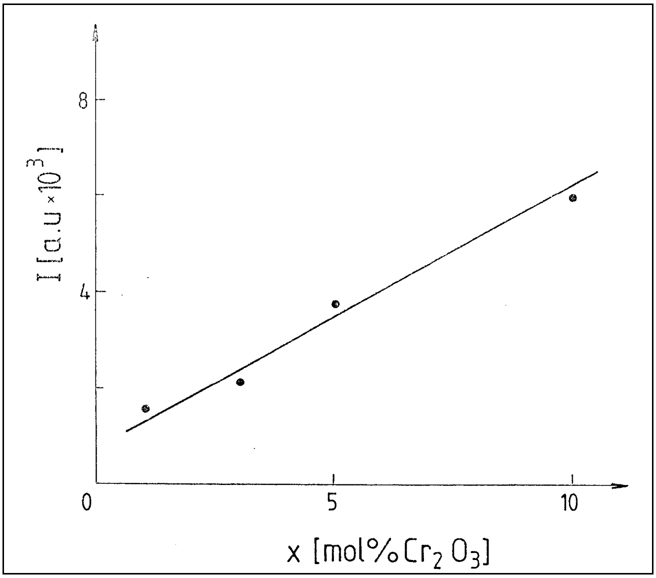

Fig. 2. *Concentration dependence of the g ≈ 1. 97 line-intensity in $xCr_2O_3 \cdot (100-x)[70TeO_2 \cdot 25B_2O_3 \cdot 5SrO]$ glasses.*

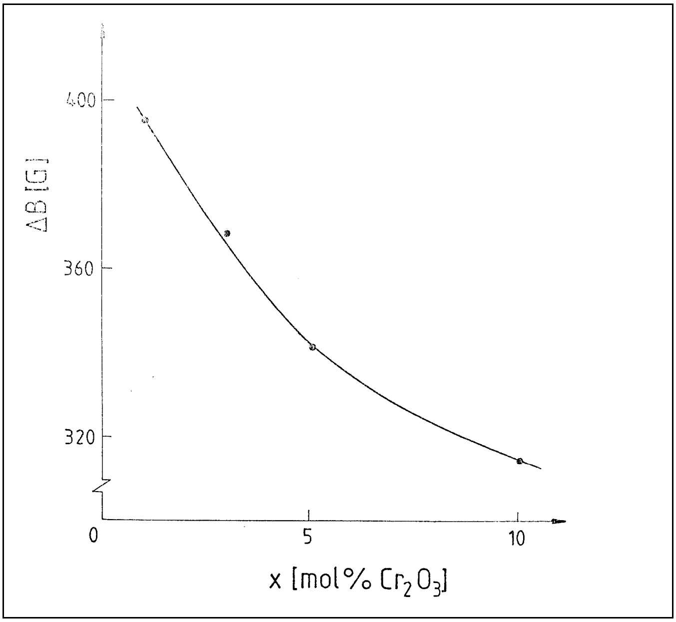

Fig. 3. *Concentration dependence of the g ≈ 1. 97 line-width in $xCr_2O_3 \cdot (100-x)[70TeO_2 \cdot 25B_2O_3 \cdot 5SrO]$ glasses.*

Magnetic susceptibility data

The reciprocal magnetic susceptibility of glasses of the studied system depends on temperature according to the graphs in Fig. 4. For glasses containing $x \leq 1$ mol % Cr_2O_3 the dependence obeys a Curie law, characteristic for magnetically isolated chromium ions. For $x > 1$ mol % Cr_2O_3 the Curie-Weiss law is obeyed. The values of the paramagnetic Curie temperature, θ_p, suggest antiferromagnetic coupling of ions. The concentration dependence of θ_p is given in Fig. 5. The specific structure of the vitreous oxide solids imposes the short-range character of magnetic interactions and enhances the structural image of ionic clusters. The results confirm the EPR data, explaining the $g \approx 1.97$ line narrowing as result of superexchange mechanisms involving ions in cluster structure. According to Fig. 5 the absolute value of θ_p increases for $x > 1$ mol % with the magnetic ions concentration of the sample, in accord to theoretical data [24]. The absolute values of θ_p are larger than those corresponding to $xCr_2O_3{\cdot}(100\text{-}x)[70TeO_2{\cdot}25B_2O_3{\cdot}5SrF_2]$ glasses [23], result which support the EPR linewidth data, comparativelly pointed out for the two vitreous systems.

The estimated values of the molar Curie constant, C_M, in Table 1, are proportional with the Cr^{3+} ions concentration. The experimental values of the effective magnetic moment, μ_{eff}, are very close to the magnetic moment of Cr^{3+} in the free ion state: $\mu_{Cr^{3+}} = 3.87\ \mu_B$ [25] attesting the preponderance of this valence state of chromium ions for all the studied glasses (Table 1).

Table 1.

Molar Curie constant and magnetic effective moment values
for some representative glasses of the system
$xCr_2O_3{\cdot}(100\text{-}x)[70TeO_2{\cdot}25B_2O_3{\cdot}5SrO]$.

x [mol % Cr_2O_3]	**C_M [emu/mol]**	**μ_{eff} [μ_B]**
1	0. 037289	3. 86
3	0. 11190	3. 86
5	0. 18676	3. 87
10	0. 37340	3. 86

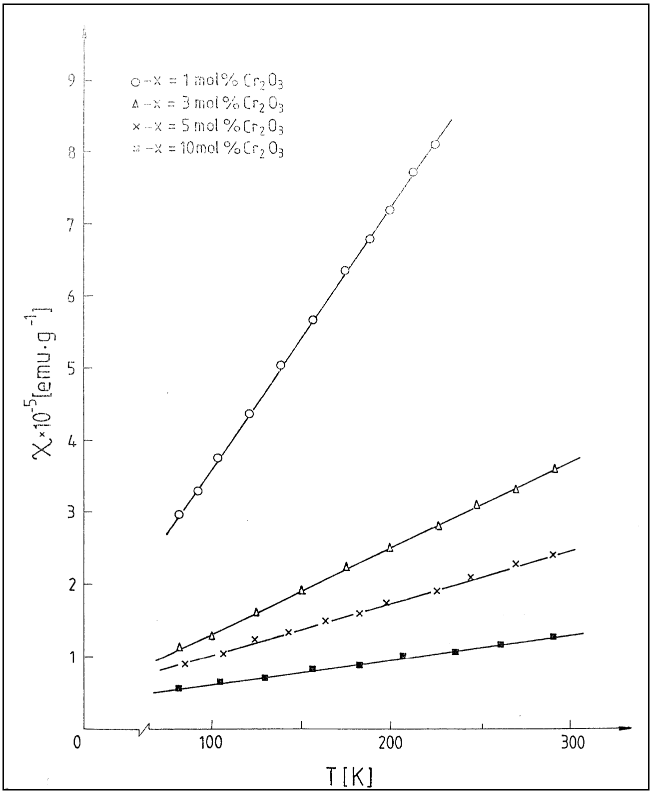

Fig. 4. Temperature dependence of the reciprocal magnetic susceptibility of several glasses, representative for the $xCr_2O_3\cdot(100\text{-}x)[70TeO_2\cdot 25B_2O_3\cdot 5SrO]$ *system.*

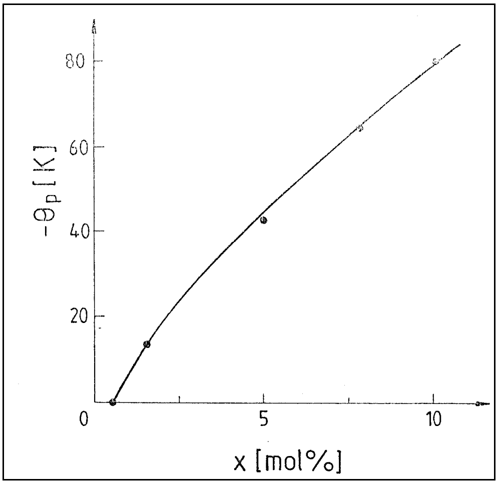

Fig. 5. *Concentration dependence of the paramagnetic Curie temperature, characteristic for chromium containing* $70TeO_2\cdot 25B_2O_3\cdot 5SrO$ *glasses.*

Conclusions

Homogeneous, stable glasses of the system $xCr_2O_3 \cdot (100-x)[70TeO_2 \cdot 25B_2O_3 \cdot 5SrO]$ were obtained within $0 \leq x \leq 10$ mol %. Only Cr^{3+} ionic species were detected by means of EPR spectrometry and magnetic susceptibility measurements. For samples containing $0 < x \leq 1$ mol % Cr_2O_3 isolated Cr^{3+} ions were detected in octahedral symmetric sites subjected to distortions. For strongly distorted sites EPR absorption signals were detected for all concentrations attributed to Cr^{3+} ions in sites subjected to strong crystal field effects, having a predomninantly rhombic ($g \approx 4.8$) or axial ($g \approx 4.0$) character. Besides these ions there are Cr^{3+} ions involved in cluster structures, giving rise to absorbtions at $g \approx 1.98$ which, for $x > 1$ mol % are magnetically coupled by superexchange mechanisms, as magnetic susceptibility measurements demonstrate.

REFERENCES

1. J. Moncoujoux, J. Faurie, K. Kohlmüller, Verres Refract. 31, 47 (1968).
2. H. Harper, P. F. James, P. W. McMillan, Discuss. Faraday Soc. 50, 382 (1970).
3. J. Dimitriev, V. Dimitrov, M. Arnaudov, J. Mater. Sci. 18, 1353 (1983).
4. J. Dimitriev, V. Dimitrov, A. Gatev, E. Kashechieva, J. Non-Cryst. Solids 95/96, 937 (1987).
5. H. H. Qui, H. Mori, H. Sakata, T. Hirayama, Ceram. Soc. Jpn. Int. Ed. 103, 32 (1995).
6. I. Ardelean, M. Peteanu, V. Simon, S. Filip, N. Muresan, Studia Univ. Babes-Bolyai, Physica XLI, 2 (1996).
7. M. Peteanu, V. Simon, N. Muresan, I. Ardelean, J. Mat. Sci. Technol. 13, 374 (1997).
8. I. Ardelean, M. Peteanu, S. Simon, S. Filip, V. Simon, C. Bob, N. Muresan, Rom. Rep. Phys. 51 (5-6), 505 (1999).
9. D. Loveridge, S. Parke, Phys. Chem. Glasses 12, 19 (1971).
10. I. Ardelean, Gh. Ilonca, M. Peteanu, E. Barbos, E. Indrea, J. Mat. Sci. 17, 1988 (1982).
11. A. Shriniwasa Rao, J. Lakshama Rao, J. S. V. Lakshman, Solid State Commun. 85 (6), 529 (1993).
12. R. J. Landry, J. T. Fournier, C. G. Young, J. Chem. Phys. 46, 1285 (1967).
13. V. K. Zacharov, D. M. Yudin, Soviet. Phys. Solid State 7, 1267, (1965).
14. I. Ardelean, M. Peteanu, S. Filip, V. Simon, C. Bob, J. Mater. Sci. 33, 357 (1993).
15. G. Fuxi, D. He, L. Huiming, J. Non-Cryst. Solids 52, 135 (1982).

16. M. Dance, J. J. Videau, J. Portier, J. Non-Cryst. Solids 86, 88 (1986).
17. E. A. Harris, Phys. Chem. Glasses 28, 196 (1987).
18. C. Leign, J. Y. Buzare, J. Emery,C. Jacoboni, J. Phys. Condens. Mat. 7, 3853, (1995).
19. N. S. Garifyanov, Soviet. Phys. Solid State 4, 1975 (1963).
20. J. Wong, C. A. Angell, Appl. Spectr. Revs. 4 (2), 155 (1971).
21. R. Brückner, N. Sammet, H. Shockhorts, J. Non-Cryst. Solids 40, 273 (1980).
22. O. Cozar, I. Ardelean, I. Bratu, Gh. Ilonca, S. Simon, Solid State Commun. 86, 569, (1993).
23. I. Ardelean, M. Peteanu, V. Ioncu, N. Muresan, Modern Phys. Letters B, 15(22), 941 (2001).
24. E. J. Friebele, N. C. Koon, L. K. Wilson, D. L. Kinser, J. Amer. Ceram. Soc. 57, 237, (1974).
25. L. M. Mulay, Magnetic Susceptibility, Interscience, New York, 1973, p. 1773.

STUDIA UNIVERSITATIS BABEŞ-BOLYAI, PHYSICA, XLVII, 1, 2002

DETERMINATION OF ELECTRICAL PARAMETERS OF CCP AT ATMOSPHERIC PRESSURE

S. D. ANGHEL[1]

ABSTRACT. In this work a method of determination of electrical parameters of an air rf capacitively coupled plasma at atmospheric pressure is presented. The method is based on the direct measurement of oscillation frequency of rf oscillator and on the simulation of the behaviour of the equivalent circuit using a computer program. The results are in accordance with those obtained by other authors.

Introduction

Electrical measurement methods don't always permit the direct measurement of high radiofrequency (rf) currents and voltages. To understand the physical behaviour of rf plasmas, the various models were developed. The modelling of the plasma has proved to be valuable for industrial and analytical applications, such as lighting, gas discharge lasers and spectral source [1]-[7]. This work combine the advantages of electrical modelling of capacitively coupled plasma (CCP) with direct electrical measurements to determinate the capacitance of a CCP at atmospheric pressure and the voltage on the plasma sustaining electrode.

Electrical models for CCP

The plasma was generated with an rf generator described in a previous work [8]. It was generated in air at atmospheric pressure at a consumed power of 38 W. A particularity of the plasma is that it is the intrinsic part of the resonant circuit of the rf oscillator. Plasma is struck on a sharp tip of a metallic electrode that is connected of the coil of the resonant circuit (Fig. 1).

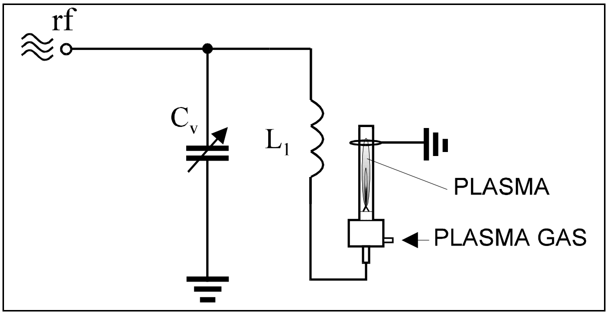

Fig. 1. – *Resonant circuit of the rf oscillator in which the plasma is ignited.*

---

[1] *"Babes-Bolyai" University, Faculty of Physics, 3400 Cluj-Napoca, Romania*

As a consequence, the electrical parameters of the oscillator (consumed power, oscillation frequency, the amplitude of the rf voltage on the plasma sustaining electrode) have different values in the absence of the plasma and in the presence of its. According to other authors [2], [7], if the plasma is in contact with both electrodes (Fig. 2a) it can be modelled as an analog circuit that is presented in Fig. 2b.

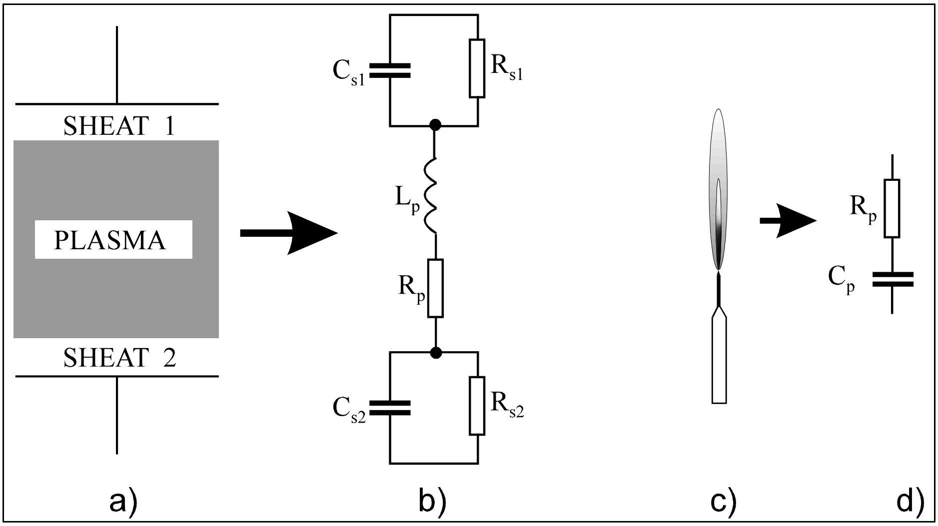

Fig. 2. *– Analog circuits for plasmas.*

In that circuit C_{s1} and C_{s2} are the capacitances of the sheaths that are presented close to the electrodes, R_{s1} and R_{s2} are the resistances of the sheaths, L_p and R_p are respectively the collisional inductance and the resistance of the plasma. The studied CCP being in contact with a single electrode (Fig. 2c), only one sheath is present. Because this sheath is lacked of electrons, its resistance is very high and it can be omitted ($R_{s2}>>1/\omega C_{s2}$). On the other hand, because the electron collision frequency (ν_c) under atmospheric pressure is very high, the inductance of the plasma (R_p/ν_c) is very small and, as a consequence, $R_p>>\omega L_p$. Considering the above suppositions, the electrical model of our CCP is that on Fig. 2d, where C_p represents the total capacitance of the plasma.

Under these considerations on the analog model of the plasma, the equivalent circuit of the diagram presented in Fig. 1 is given in Fig. 3 (Fig. 3a - in the absence of the plasma and Fig. 3b - in the presence of its).

The capacitance C_v was neglected because it don’t influence the behaviour of the circuit under resonant conditions ($Cv >> C_1, C_2, C_p$).

In the circuits shown in Fig. 3 r_1 and C_1 represent the loss resistance and the capacitance of the coil L_1, and C_2 is the capacitance between the plasma sustaining electrode and the ground in the absence of the plasma. The parameters of the coil (L_1, r_1, C_1), were measured with a Q-metric method. The resistance of the plasma (R_p) was determined with a substitution method [8]. It is in the range of 50 – 150 kΩ, depending on the anodic voltage of the oscillator. The oscillation frequencies (in the absence and presence of the plasma) were measured with a frequency-meter, via a coil inductively coupled with the coil of the resonant circuit of the oscillator.

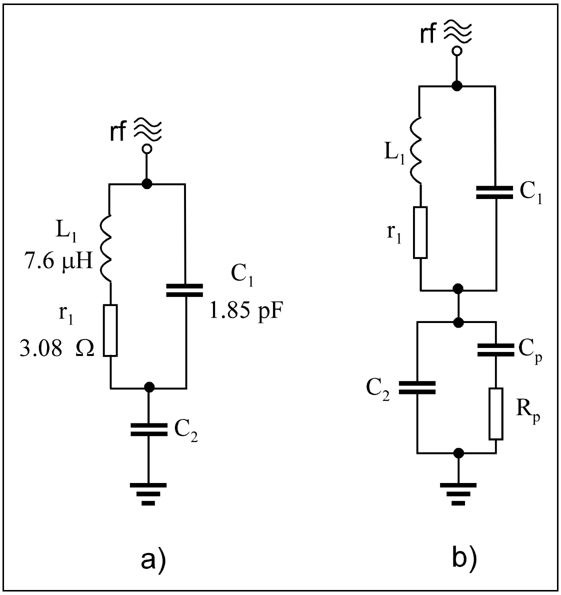

Fig. 3. *– Equivalent circuits for the diagram presented in Fig. 1: (a) - in the absence of the plasma; (b) - in the presence of its.*

Results and discussions

The behaviour of the above circuits was analyzed using a computer simulation program (Electronics Workbench). Thus, in Fig. 4a are plotted the Bode diagrams (voltage and phase) of the circuit in the absence of the plasma. The measuring point is the plasma sustaining electrode. One can be see there are two values of the frequency for which the circuit is under resonant conditions:

$$f_{01} = \frac{1}{2\pi\sqrt{L_1(C_1 + C_2)}} = 19.76\,\text{MHz} \tag{1}$$

and

$$f_{02} = \frac{1}{2\pi\sqrt{L_1 C_1}} = 42.46\,\text{MHz} \tag{2}$$

The plasma can be struck at the frequency f_{01} because only at this frequency the rf voltage on the sustaining electrode is sufficient high to initiate the ignition of the discharge at atmospheric pressure. For capacitance C_2 has been chosen that value (6. 67 pF) for which the oscillation frequency done by simulation has the same value as the measured one.

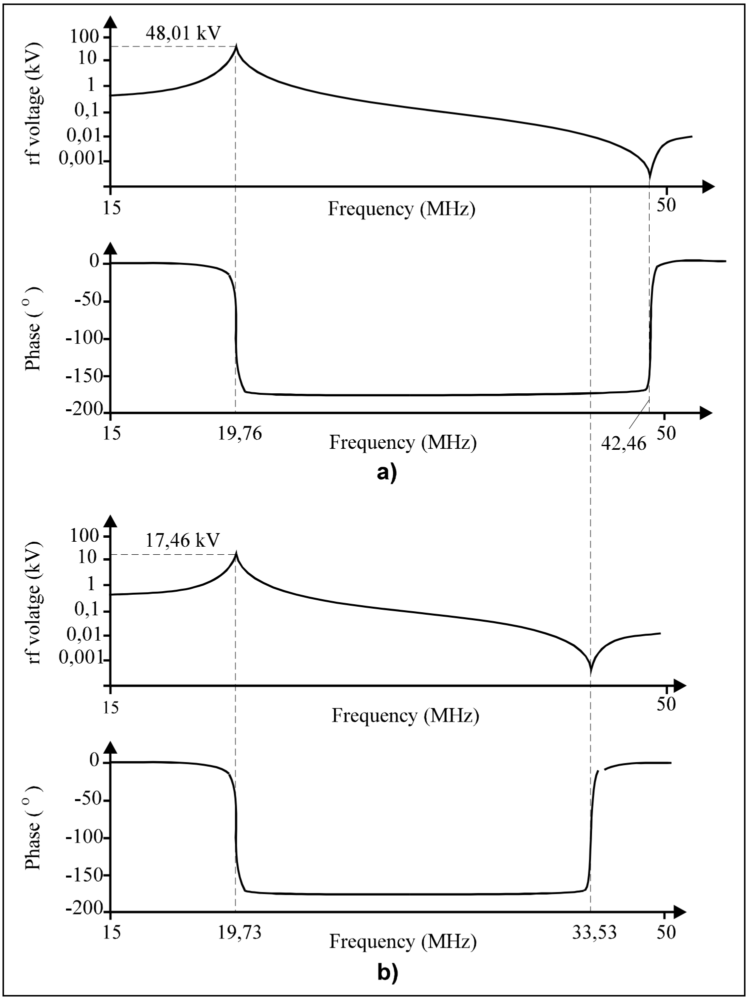

Fig. 4. *– Bode diagrams for circuits shown in Fig. 3. (a) – in the absence of the plasma; (b) – in the presence of its.*

The presence of the plasma determines the modification both of the oscillation frequency and the voltage on the sustaining electrode (Fig. 4b). In those plots, for R_p has been chosen the value of 100 kΩ [8]. For C_p has been chosen that value (0. 1 pF) for which the oscillation frequency done by simulation has the same value as the measured one (16. 73 MHz).

In Fig. 5 are given the dependencies of the oscillation frequency (a) and the rf voltage of the plasma sustaining electrode (b) on the plasma capacitance for a value of the plasma resistance of 80 kΩ. One can be see that the oscillation frequency has a minimum at 0. 1 pF and the rf voltage on the sustaining electrode continuously decrease.

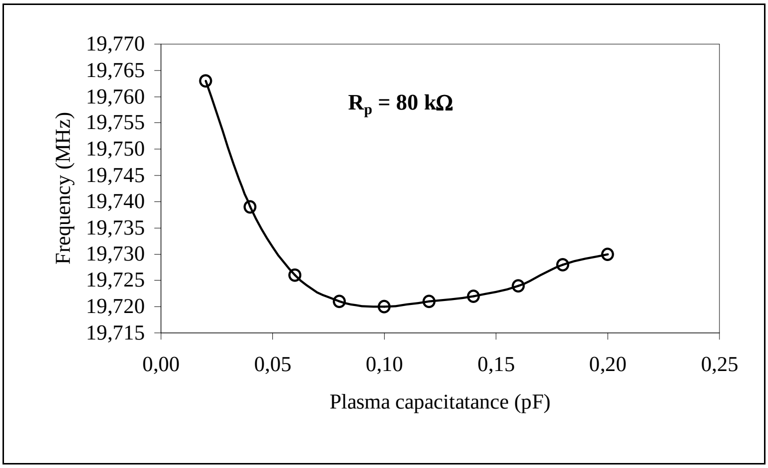

a)

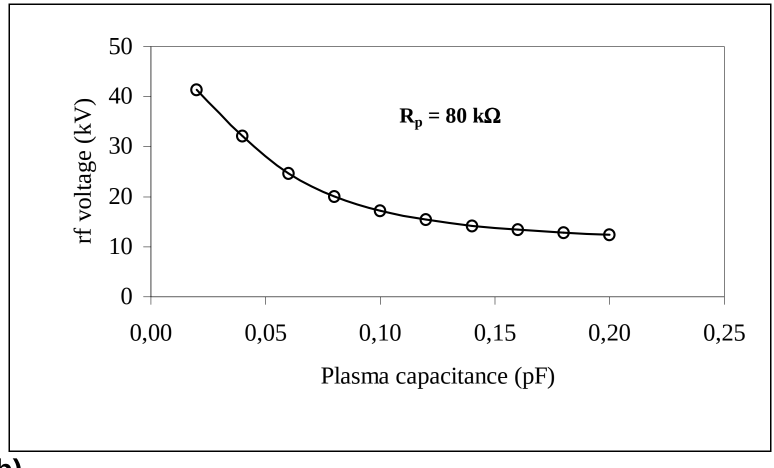

b)

Fig. 5. *– The dependence of the oscillation frequency (a) and the rf voltage of the plasma sustaining electrode (b) on the plasma capacitance.*

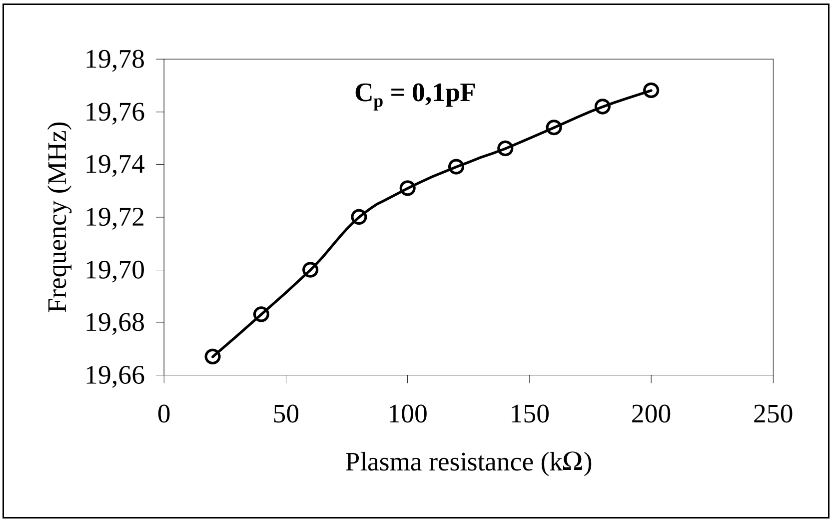

a)

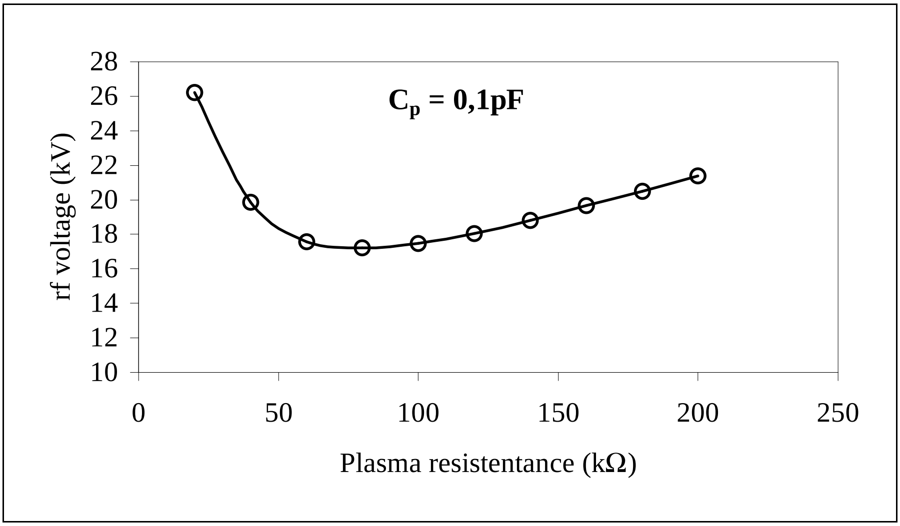

b)

Fig. 6. *– The dependence of the oscillation frequency (a) and the rf potential of the plasma sustaining electrode (b) on the plasma resistance.*

In Fig. 6 are shown the dependencies of the oscillation frequency (a) and the rf voltage of the plasma sustaining electrode (b) on the plasma resistance for a value of the plasma capacitance of 0. 1 pF. The oscillation frequency has a minimum at 80 kΩ and the rf voltage on the sustaining electrode continuously increase.

Experimental observations have shown that the working point of the oscillator is that for which the plasma capacitance is minimum.

As a conclusion, we can affirm that the electrical parameters of the analog circuit of the capacitively coupled plasma maintained in air at atmospheric pressure are: C_p = 0. 1 pF and R_p = 80 kΩ. This result is in accordance with that of Cristescu [9]. Using other measuring methods, he concluded that a 71 W CCP in air at atmospheric pressure has a capacitance of 0. 1 pF and a resistance of 58 kΩ.

This research was supported by Research Grant 34/1260, CNCSIS/2002.

REFERENCES

1. P. A. Miller, Proc. SPIE ***1594***,179-188 (1991).
2. G. G. Lister, J. Phys. D: Appl. Phys. ***25***, 1649-1680 (1992).
3. M. A. Sobolevski, J. Vac. Sci. Technol. ***10***, 3550-3562 (1992).
4. M. A. Sobolevski and J. R. Whetstone, Proc. SPIE ***1803***,309-320 (1992).
5. M. A. Sobolevski, J. Res. Natl. Inst. Stand. Technol. ***100***, 341351 (1995).
6. L. P. Bakker, G. M. W. Kroesen and F. G. de Hoog, IEEE Trans. Plasma Sci. ***26***, 1017-1021 (1998).
7. M. A. Lieberman and A. J. Lichtenberg, "Principles of plasma discharges" J. Whiley & Sons, New York 1994.
8. E. Tataru, S. D. Anghel and I. I. Popescu, Rev. Roum. Phys. ***39***, 29-44 (1991).
9. G. D. Cristescu and R. Grigorovici, Rev. Roum. Phys. ***1***, 103 (1956).

STUDIA UNIVERSITATIS BABEŞ-BOLYAI, PHYSICA, XLVII, 1, 2002

ROTATIONAL TEMPERATURES OF THE OH BAND (A $^2\Sigma^+$, $\nu = 0 \rightarrow$ X $^2\Pi$, $\nu' = 0$, AT 306. 357 NM) IN A VERY LOW RF POWER CAPACITIVELY COUPLED PLASMA

ALPAR SIMON[1]*, SORIN DAN ANGHEL[1], SIMION SIMON[1], TIBERIU FRENTIU[2], ERNA CZIRJAK[2], EMIL A. CORDOS[2]

ABSTRACT. The very low power radiofrequency capacitively coupled plasma could be used as spectral source for the analysis of pneumatically nebulised liquid samples or non-conductive solid samples via atomic emission spectroscopy technique. The plasma could be easily sustained at atmospheric pressure in Ar, air or their mixtures. In the present paper, this new spectral source was characterized from physical point of view, by means of rotational temperatures of the OH band (A $^2\Sigma^+$, $\nu = 0 \rightarrow$ X $^2\Pi$, $\nu' = 0$, at 306. 357 nm). The rotational temperatures (1900 – 2900 K) were measured as function of radiofrequency power, observation height, radial position, gas flow-rate and gas composition. The experimental spectra was compared to the computer simulated syntethic spectra. The temperatures determined from the OH (0, 0) spectra are in good agreement with temperatures obtained for other plasma spectral sources.

1. INTRODUCTION

1. 1. Brief history of capacitively coupled plasmas

The principle of capacitive coupling to generate radiofrequency (RF) plasmas has been known since the late 20's [1]. The first spectroscopic study was reported by Asami and Hori [2] by enumerating the molecular bands and atomic lines. Probably one of the most cited historical reference about capacitively coupled plasmas (from now on referred to as CCPs) is that of Cristescu and Grigorovici [3]. Babat carried out the first systematic investigation on capacitively coupled plasmas in 1942 [4]. Further studies and developments of CCP were shadowed in the early 60's by the works of Reed [5], Greenfield et al. [6], Wendt and Fassel [7] about the inductively coupled plasma (ICP). Because of the very good results and the versatility of

---

[1] *Babes-Bolyai University, Faculty of Physics, Department of Electricity, Magnetism and Electronics RO-3400 Cluj-Napoca, Kogalniceanu 1, ROMANIA*

* *corresponding author*

[2] *Babes-Bolyai University, Faculty of Chemistry and Chemical Engineering, Department of Analytical Chemistry RO-3400 Cluj-Napoca, Kogalniceanu 1, ROMANIA*

the ICP, the CCP has been largely ignored by the spectroscopic community, but found an important role in the field of plasma material processing.

Later, in the mid 80's, the capacitively coupled radiofrequency plasma, in several different electrode geometries, used as spectral sources for atomic emission spectroscopy, was studied in the last fifteen years from both physical and analytical points of views [8-23]. This type of plasma become a fairly good spectral source: it could be ignited and maintained with several electrode geometries (annular, parallel-plate, coaxial), in different gas atmospheres (Ar, He, air or Ar-air mixtures), at various RF frequencies and RF power levels (from 13. 56 or 27. 12 MHz up to 150 MHz and from 10-200 W up to a few kilowatts) and run with low gas consumption (flow-rates usually less than or around 1 $l\cdot min^{-1}$). The most important advantage of using a CCP as spectral source is mainly an economical one: low operational and maintenance costs versus fairly good analytical performances.

The historical milestones of CCP becoming a spectral source are presented in Table 1.

In the present paper, the very low RF power CCP is characterized from physical point of view by means of rotational temperature of the OH band ($A\ ^2\Sigma^+$, $\nu = 0 \rightarrow X\ ^2\Pi$, $\nu' = 0$, at 306. 357 nm). The rotational temperatures (in the range of 1900 – 2900 K) were measured as function of RF power, observation height, radial position, gas flow-rate and gas composition. The temperatures determined from the (0, 0) band spectra are in good agrement with the temperatures obtained for other low power plasmas.

1. 2. The very low RF power capacitively coupled plasma

With respect to the consumed RF power, the capacitively coupled plasmas sustained at atmospheric pressure could be classified in three main categories: (i) *very low power CCP*s with RF powers less than 100 W; (ii) *medium power CCP*s obtained with RF powers usually 100-500 W and (iii) *high power CCP*s, which are needing more then 500 W for ignition and maintenance.

The construction of the RF generator, used for sustaining the very low power capacitively coupled plasma at atmospheric pressure, is described in details elsewhere [24].

The plasma was generated by means of a CCP torch (Fig. 1) at a frequency of 13. 56 MHz and absorbed RF powers in the range of 5-70 W. The plasma is the intrinsic part of the resonant circuit of a free-running oscillator. It is sustained on a kanthal tip (composition: 20. 5–23. 5 % Cr, 5. 3 % Al, max. 0. 08 % C, max. 0. 7 % Si, max. 0. 4 % Mn and Fe to balance; density: 7. 15 $g\cdot cm^{-3}$; electrical resistivity at 20 ^oC: 1. 39 Ωmm^2m^{-1}; melting point: 1850 ^oC).

Table 1.

Historical milestones of capacitively coupled plasmas

Year	Scientists	Historical event
1928-1929	S. J. Zilitineewisch, K. Baxter, K. Heinrich	- first (accidental) observation of an RF torch-like discharge
1933-1935	M. Neimann, L. Rohde, H. Schwarz	- electrical equivalent circuit for the torch
1939	Y. Asami, T. Hori	- first spectroscopical investigations (listing of the most proeminent molecular bands and atomic lines)
1941	G. Cristescu, R. Grigorovici	- capacitively coupled discharge between two plate-parallel discharges (lower plate with a sharp tip)
1942	G. I. Babat	- the very first systematic investigation
1949-1956	G. Cristescu, R. Grigorovici	- study of the very high frequency torch (voltage-current characteristics, dissipated power, spectral investigations)
1961	G. Cristescu, M. Giurgea	- tandem discharge: RF torch + DC discharge
1969-1971	H. A. Schwab	- study of a capacitively coupled discharge with electrodes in contact with the discharge
1970-1980	In the shadow of the ICP	
1980	R. J. Winslow	- the ideea to use a low pressure, plate-parallel oxygen discharge to spectrochemical analysis
1988-1989	D. C. Liang, D. Huang, M. W. Blades	- plasma with plate-parallel electrodes for atomic absorption and /or chromatography
1989	M. W. Blades / R. E. Sturgeon	- FAPES (Furnaces Atomisation Plasma Excitation Spectrometry)
1990-1991	The first commercial FAPES	*Aurora Instruments Ltd.*, Vancouver, British Columbia, CANADA
1991-2001	S. D. Anghel, E. A. Cordoș, T. Frențiu, A. Simon, A. Popescu	- capacitively coupled plasmas in various electrode geometries (tip, tip-ring, tube-ring) and RF power levels (medium: 185-275 W, very low: 10-100 W) for the analysis of pneumatically nebulised liquid samples, for the direct analysis of conductive or non-conductive solid samples via atomic emission technique

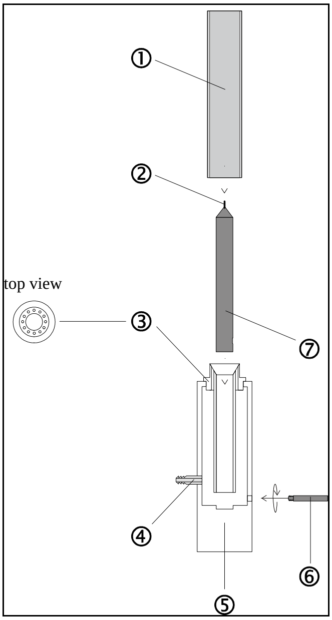

Fig. 1. *– The CCP torch*

The main parts of the CCP torch (Fig. 1) are: the quartz tube (①: 14 mm i. d., 16 mm o. d., 70 mm length); the kanthal tip (②: 0. 8 mm in diameter, 4 mm length); the electrode holder made out of PTFE (③: 12 concentric holes, 1 mm in diameter for providing the sample entrance to the plasma); the plasma gas and sample introduction inlet (④); the PTFE mixing chamber (⑤: volume = 10 ml); the brass RF connector (⑥) and the brass electrode as support for the tip (⑦).

The plasma gas could be Ar (spectral purity), air or their mixture, and it flows in a laminar motion through the quartz tube with flow-rates between 0. 1-2. 0 $l\cdot min^{-1}$. The plasma has a candle flame-like shape (Fig. 2). If it is sustained in Ar, it has a sparking yellow superficial luminescence which surrounds the tip and it is followed by the plasma core which has two different zones: one having the shape of an upside down letter Y and being colored in purple and another one above, a white-yellow plasma core in the shape of an upside down, elongated egg. All this parts are surrounded by a white-bluish mantle. These zones are characteristic for a torch like capacitively coupled plasma [25-27] and are separated from each other by very thin dark spaces (one between the superficial luminescence and the rest of the plasma, right above the tip, and the other one right above the white-yellow plasma core). The presence of air in the discharge gives an orange like colour to the plasma. The spatial dimensions of the plasma and its characteristic zones are function of the plasma power and gas flow-rate.

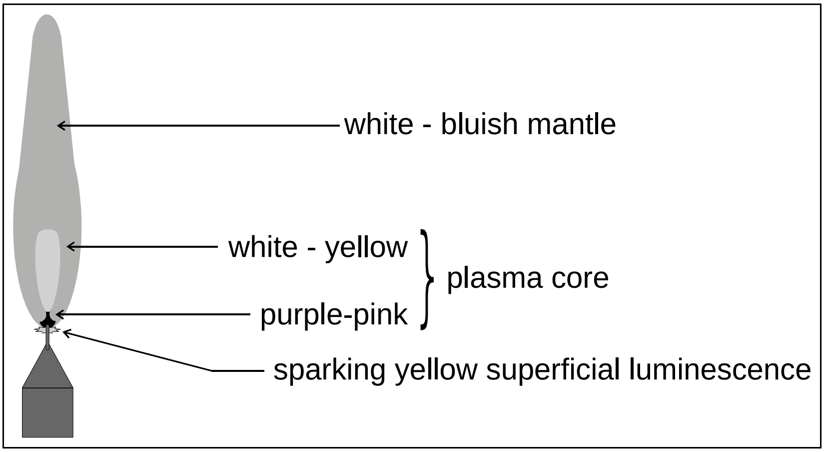

Fig. 2. *– The very low power capactively coupled plasma*

The plasma emission intensity increases with RF power and the plasma length and diameter increase with the Ar flow-rate. The addition of air changes both size and shape of each region of the diagram. The colour of each region is also affected (orange like tint).

At Ar flow-rates below 0. 1 l·min^{-1} (independently of RF power level) and RF powers below 6 W (independently of Ar flow-rate), the plasma could not be ignited.

For RF powers between 6-70 W and Ar flow-rates between 0. 1-0. 3 l·min^{-1} a highly unstable, randomly moving, lightning like purple-pink multifilamentary discharge is obtained. The discharge is moving around the surface of the electrode, being impossible to focus it onto the entrance slit of the spectrometer.

For Ar flow-rates of 0. 3-0. 4 l·min^{-1} and RF powers from 15-20 W to 70 W a bluish, unstable plasma is obtained. Its diameter was around 3 mm, with a plasma height between 30 and 40 mm. Due to its unstable aspect, this plasma is not suitable for spectroscopic investigations or applications.

A well formed and well defined, highly stable plasma is obtained for RF powers varying from 15-20 W up to 60 W and for Ar flow-rates from 0. 3-0. 4 l·min^{-1} up to 1 l·min^{-1}. The plasma has the well known candle flame-like shape, the dimensions and colours of its characteristic zones being function of RF power and/or Ar flow-rate.

Thus, for an Ar flow-rate of 0. 7 l·min^{-1}, the plasma aspect and dimensions as function of RF powers are listed in Table 2. For an RF power of 60 W, the plasma aspect and dimensions as function of Ar flow-rate are listed in Table 3.

Table 2.

CCP aspect and dimensions for Ar flow-rate of 0. 7 l·min^{-1}, as function of RF power

RF power [W]	CCP aspect and dimensions
20 and 30	~50-55 mm length and 4 mm diameter (no purple-pink core, ~3 mm in height white yellow core)
40	~50-55 mm length and 5 mm diameter (~1-2 mm purple-pink core, ~3 mm white yellow core)
50	~55 mm length and 5 mm diameter (~5 mm purple-pink core, ~10 mm in height white yellow core)
60	~55 mm length and 5-6 mm diameter (~6-7 purple-pink core, ~15 mm in height white yellow core)

Table 3.

CCP aspect and dimensions for an RF power of 60 W, as function of Ar flow-rates

Flow-rate [l·min^{-1}]	CCP aspect and dimensions
0.3	~35 mm length and ~3 mm diameter (no purple-pink and white yellow core)
0.4	~40 mm length and ~ 4 mm diameter (no purple-pink core, ~4 mm in height white yellow core)
0.5	~45-50 mm length and 5 mm diameter (~1 mm purple-pink core, ~3 mm in height white yellow core)
0.6	~50 mm length and 5 mm diameter (~2-3 mm purple-pink core, ~5 mm in height white yellow core)
0.7 ÷ 1.0	~55 mm length and 5-6 mm diameter (~6-7 purple-pink core, ~15 mm in height white yellow core)

The most stable plasma, used for spectroscopic applications, is that obtained at 60 W and 0. 7 l·min^{-1} Ar.

At flow-rates above 0. 3 l·min^{-1} and RF powers in the range of 6-15 W, a very thin (~ 2-3 mm) and very small (~ 10-25 mm) bluish, unstable and unifilamentary plasma is obtained. It is not suitable for spectroscopic investigations.

For Ar flow-rates of 0. 4-1. 0 l·min^{-1} and RF powers higher than 60 W, and for RF powers of 15-70 W at flow-rates between 1. 0-2. 0 l·min^{-1} the plasma has a similar size and shape with that obtained at 60 W and 0. 7 l·min^{-1}. In these ranges, random instabilities due to the overheating of the tip (at higher than 60 W RF powers) or mechanical fluctuations of the plasma (at higher flow-rates than 1 $l \cdot min^{-1}$) could jeopardize the spectroscopic investigations, therefore it would be wise to avoid these operating conditions.

1. 3. Rotational temperature for the OH (0, 0) band

The study of the physical characteristics of a plasma source is a very important preliminary step toward understanding the mechanisms and processes that occur within a plasma used as spectral source and in the same time it has a major role in the development, optimization and comparison of plasmas as sources for atomic emission spectroscopy.

The electron number densities and the temperatures in the active regions of the plasma spectral sources (i. e., plasma core) are relatively small and it is quite difficult to use atomic emission spectroscopy as diagnostic technique [28, 29]. Molecular emission spectroscopy is an efficient diagnosis method to monitor temperatures in low temperature plasmas, because of their special characteristics, and can successfully give information in a quite large temperature interval (from a few hundreds K up to 8000 K) where atomic spectra are not strong enough to ensure a good sensitivity.

The molecular rotational energy levels have a special characteristic: compared with excited electronic state exchanges, the exchange rate between excited rotational states of molecules or radicals is very fast (Boltzmann distribution could be assumed [30]). As we will see immediately, the energy differences between the rotational levels is relatively low, the rotational relaxation is very fast, which leads the excited rotational energy states to be in equilibrium with the kinetic energy of the molecules [30].

Usually the rotational electronic transitions in near UV and visible range of the electromagnetic spectrum are employed where the molecular species have excitation energy levels around 4 eV, which is with at least 10 eV lower than the excitation energies for the plasma sustaining gas (around 14-15 eV for Ar).

The OH UV spectrum could be frequently observed in many kind of flames and plasmas. The rotational temperature of this radical has a value, which is generally close to the gas temperature. This temperature can be determined using the most studied OH band: A $^2\Sigma^+$, $\nu = 0 \rightarrow$ X $^2\Pi$, $\nu' = 0$, at 306. 357 nm. This band can be easily isolated in order to give useful information.

The intensity of an individual spectral line of a rotational structure of a band depends on the line strength ($S_{JJ'}$) for that particular line, the population of molecules in the initial state and a factor C (same for all lines of the same band).

The intensity of a particular line of rotational fine structure of the band is: $I_{JJ'} = C \cdot S_{JJ'} \cdot \sigma_{JJ'}^4 \cdot \exp(-E_J / k_B T_{rot})$, where $I_{JJ'}$ is the relative intensity of a particular line in the molecular band, $\sigma_{JJ'}$ is the wavenumber of the transition,

E_J is the rotational energy of the initial level of the line and T_{rot} is the rotational temperature.

One may assume that in rotational relaxation, collisions with molecules are dominant. If no self-absorption or superposition of line occurs, T_{rot} can be determioned from line intensities using the well known Boltzmann plot method: $\ln(I_{JJ'} / S_{JJ'} \cdot \sigma_{JJ'}^4)$ vs. E_J.

This plot will have a negative slope ($tg\alpha < 0$), thus the rotational temperature would be equal to $-1/(k_B \cdot tg\alpha)$ [29].

These temperatures, as function of operating parameters (gas flow-rates and gas composition, RF power levels) and experimental conditions (viewing directions and positions), together with the plasma spectra for OH could lead us towards useful conclusions about some physical characteristics of our plasma.

2. EXPERIMENTAL DETAILS

The experimental arrangement is presented in Fig. 3. and the operating conditions are described in Table 4.

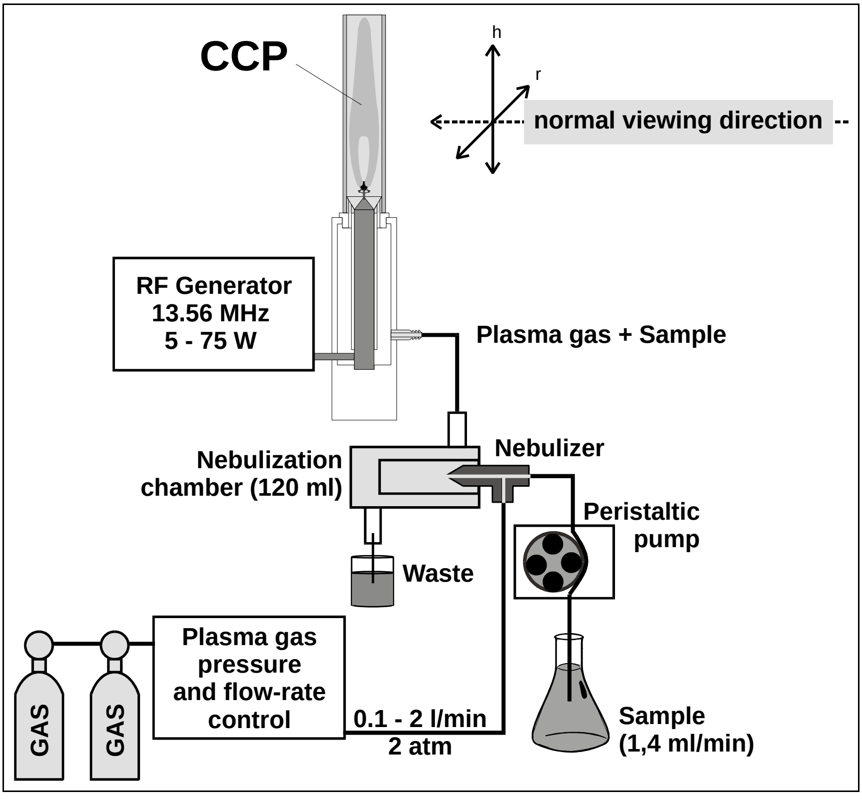

Fig. 3. *– The experimental arrangement*

Table 4.

The summary of the experimental equipment

Plasma power supply: RF oscillator with inductive reaction and grid tuned circuit (13. 56 MHz, adjustable RF power levels up to 100 W) [*Babes-Bolyai University, Faculty of Physics, laboratory constructed*] using for anodic voltage (U_a = 600-1000 V) a BS 452 E type stabilized power supply (2 × 500 V, max. 400 mA) [*TESLA, Czech Republic*] and for grid voltage (U_g = 150-200 V) a I 4104 type stabilized power supply (40 V, max. 5 A) [*IEMI, Bucharest, Romania*]
Plasma torch: Capacitively coupled type (details in Fig. 1) [*Babes-Bolyai University, Faculty of Physics, laboratory constructed*]
Sample introduction system: Meinhard type, concentric pneumatic nebulizer, 4 roller peristaltic pump; desolvation: 120 cm^3 glass chamber [*Research Institute for Analytical Instrumentation, Cluj, Romania*]
Monochromator: Computer driven scanning type (1 step = 0. 002 nm) with Czerny-Turner mount (working in first order, 1 m focal length, diffraction grating with 2400 groves/mm, slit height 20 mm, slit width 27 μm) [*Research Institute for Analytical Instrumentation, Cluj, Romania*]
Detector: 9781 R photomultiplier tube operated at 700 V [*Thorn EMI Ltd., England*]
Data acquisition and data processing: Digital data acquisition and monochromator driving carried out by an IBM-PC equipped with a laboratory constructed interface (64 μs data acquisition time); data processing with an appropriate in-house software [*Research Institute for Analytical Instrumentation, Cluj, Romania*]

The plasma emission is focused onto the entrance slit of the scanning monochromator by means of fused-silica lens (110 mm focal length, 30 mm in diameter). Internal calibrations were performed with an Al hollow cathode lamp and the corrections for the spectral response of the spectrometric system (optics and photomultiplier) were made with a spectral irradiance standard lamp (EPI 1604).

3. RESULTS AND DISCUSSIONS

The rotational temperature was determined using the OH band (A $^2\Sigma^+$, $\nu = 0 \rightarrow$ X $^2\Pi$, $\nu' = 0$) at 307. 357 nm. This temperature was calculated with four molecular lines from this band: $R_2$14 (307. 114 nm); $R_2$15 (307. 303 nm); $R_2$4 (307. 437 nm) and $R_2$3 (307. 703 nm) from the slope of the Boltzmann plot, using spectral data taken from [31].

A typical Boltzmann plot for the superficial luminescence surrounding the tip is presented in Fig. 4. It was obtained by nebulizing deionized, bidistilled water into the plasma at an Ar flow-rate of 0. 7 $l \cdot min^{-1}$ and 60 W RF power ($tg\alpha$ = - 0,000523, T_{rot} = 2700 K).

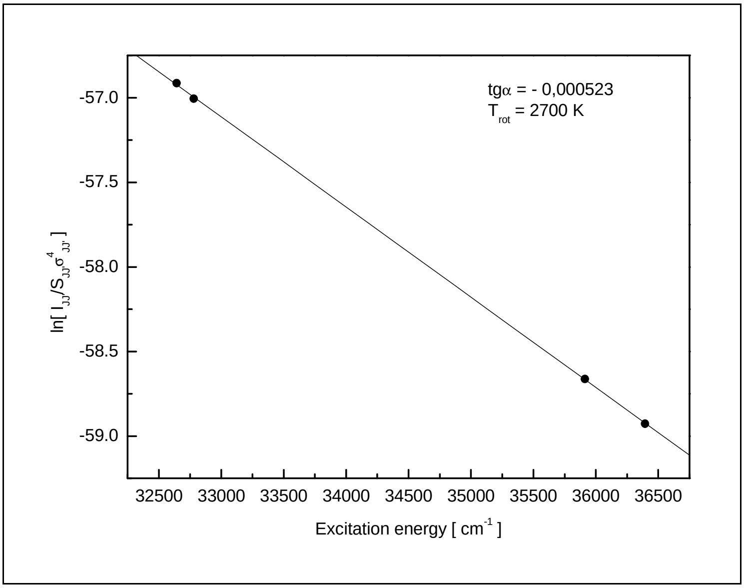

Fig. 4. *– Typical Boltzmann plot for T_{rot} measurements for OH in the very low power Ar plasma*

The influence of RF power, Ar flow-rate, observation height (distance relative to the tip) and radial position on the rotational temperature were investigated for both normal and axial viewing modes for the stable plasma region. The dependencies are presented in Figs. 5-8.

The influence of observation height, at a given RF power and an Ar flow-rate of 0. 7 $l\cdot min^{-1}$, is presented in Fig. 5. Observing these plots, one can tell that, at every RF power level there is a value of the observation height that yields to a minimum in T_{rot}. Usually, this value corresponds to dark space, which separate the white yellow core from the rest of the mantle. Due to the limitations of the experimental set-up, the spectroscopic observations were made at every 6 mm. Therefore the minimums in T_{rot}, of 2150 K and 2249 K respectively, were not plotted for 21 W and 27 W, being around 3 mm above the tip (see Table 2.). For higher RF power levels, at which the plasma is well formed and its zones are well defined, the minimum temperatures are: 2305 K (for 38 W), 2200 K (for 47 W) and 2299 K (for 60 W). From this position upward, the rotational temperature shows an increase towards the plasma tail.

The influence of RF power (at 0. 7 $l\cdot min^{-1}$ Ar flow-rate) and of the Ar flow-rate (at 60 W RF power) on the rotational temperature on T_{rot} in the superficial luminescence zone is given in Fig. 6.

The maximum value for T_{rot} could be obtained for 0. 6-0. 7 $l\cdot min^{-1}$.

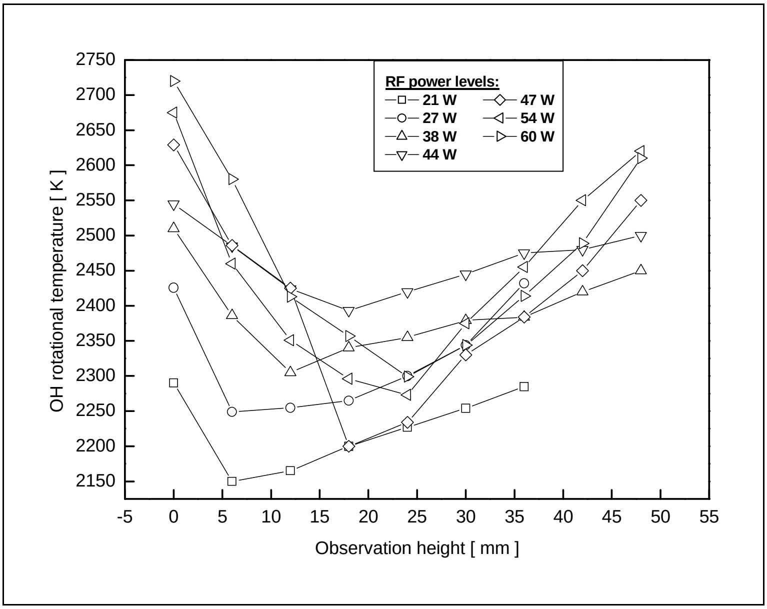

Fig. 5. *– Influence of observation height on T_{rot} (OH) for different RF power levels*

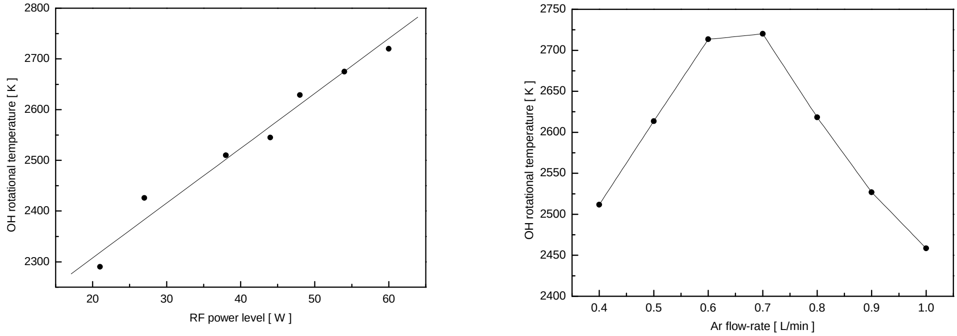

Fig. 6. *– Influence of RF power (a) and Ar flow-rate (b) on T_{rot} (OH)*

The aspect of this dependence could be explained by means of particle entrance and residence time of hydroxyl radical in plasma. Namely, for flow-rates below 0. 6 l·min^{-1} the concentration of entering OH radicals, which could be excited, is relatively low because of less nebulization efficiency. For optimum working conditions (0. 7 l·min^{-1} gas flow-rate), the nebulization efficiency is about 10 % with a liquid intake rate of 0. 09 ml·min^{-1}. At flow-rates higher than 0. 7 l·min^{-1} the residence time of the same radicals in the plasma will be not enough to be excited properly and the rotational temperature will be lower. From the point of view of rotational temperature, the ideal value of the Ar flow-rate is around 0. 6-0. 7 l·min^{-1}. This range corresponds to the most stable plasma at the optimum RF power (60 W), too. The aspect of the rotational temperature dependency on gas flow-rate is similar to that in Fig. 6b for other observation heights and RF power levels, too.

The influence of the radial distance, relative to the symmetry axis of the plasma, on the rotational temperature for viewing the superficial luminescence or the plasma at different observation heights is presented in Fig. 7.

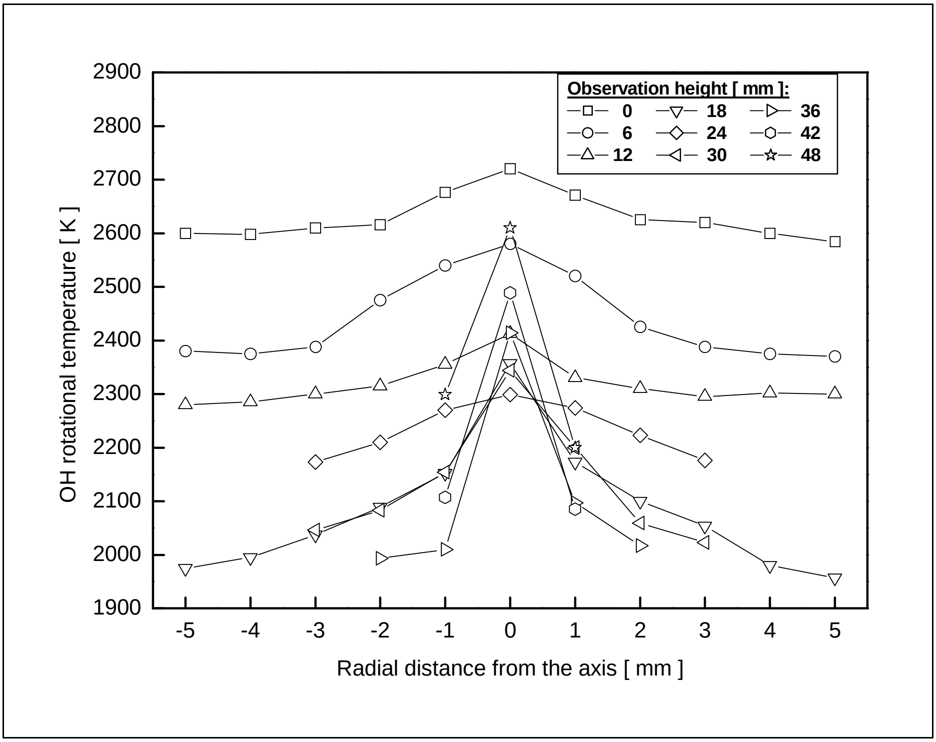

Fig. 7. *– Influence of radial distance on* T_{rot} *(OH)*

These dependencies prove good plasma symmetry relative to the vertical axis of the CCP. Fig. 7 also gives useful information about the real shape of the plasma. The very low power CCP is wider than it seems to be after a visual observation. In addition, it can be concluded that, the plasma mantle is always colder then the plasma core.

Both modelling [32] and experimental measurements [32, 33] concerning the excitation of OH species in a plasma suggest that, in the excitation mechanism, collisional excitation from one rovibrational level to another by heavy species has a major role against electron or ion impact processes, which will have a negligible impact on the rovibrational population distribution.

As it was proved by Dilecce et al. [33], whenever N_2 is present in a discharge, the OH (A $^2\Sigma^+$) excitation will be produced mainly by the reaction:

$$N_2\,(A\ ^3\Sigma^+_u,\ v) + OH\,(X\ ^2\Pi) \longrightarrow N_2\,(X\ ^1\Sigma^+) + OH\,(A\ ^2\Sigma^+_u,\ v')$$

In order to investigate more the excitational aspects, we have increased the amount N_2 present in the plasma by introducing purified (filtered) compresed air along with Ar. The influence of the air content (in %) on the rotational temperature is given in Fig. 8 (60 W RF power, 0. 7 l·min^{-1} gas flow-rate, 12 mm above the tip).

As can be seen, this dependence depicts the variation of T_{rot} from pure Ar plasma to pure air plasma. The plot exhibits an increase in the rotational temperature (from 2434 K to 2877 K) due to an increase in air content (more and more OH radical excited by collision with the entering N_2 molecules). This plot has a particular aspect: at contents higher than 60 % air in Ar it presents saturation in T_{rot} (around 2880 - 2890 K). The most reasonable explanation seems to be this: the amount of N_2 entering the plasma will excite almost all the OH radicals originating from the nebulised water, resulting a higher value of the rotational temperature than the value of T_{rot} (2720 K) in the most hottest place in the plasma (superficial luminescence around the tip, 60 W RF power, 0. 7 l·min^{-1} gas flow-rate).

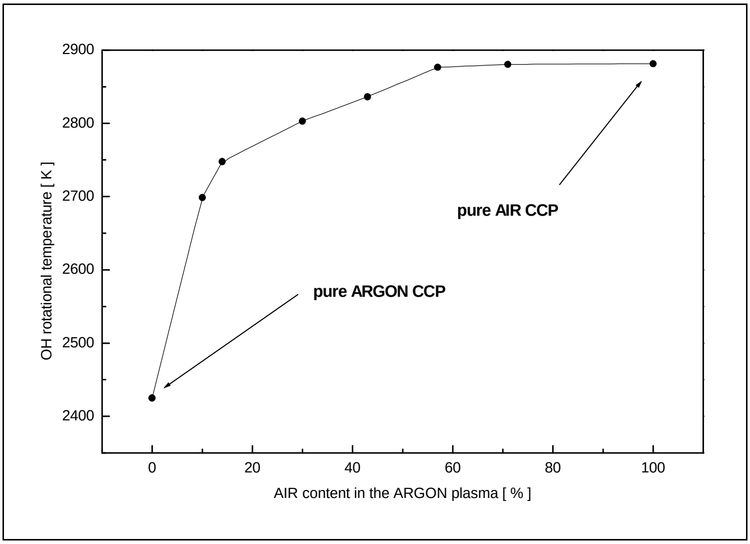

Fig. 8. *– Influence of air content in the plasma on T_{rot}(OH)*

One can say that in our Ar CCP the excitation of the OH radical is due to collisions with Ar atoms or N_2 molecules present as trace impurities.

This statement is supported by T_{rot} dependency on Ar flow-rate: as the Ar flow-rate increases the rotational temperature will increase due to the collision between more and more Ar atoms and OH radical, which lead to a higher number of excited OH radicals. Starting from a critical value of the flow-rate (which seems to be around 0. 6-0. 7 $l{\cdot}min^{-1}$) the higher flow speed of both Ar atoms and OH radicals will obstruct this type of collisions (the particles will not stay sufficiently long time in the plasma). In this situation, the rotational temperature will decrease.

The superficial luminescence zone was tested to see if easily ionisable elements (Na, Li, K, Ca) have any influence on the rotational temperature. The experimental conditions were: 60 W, 0. 7 0. 7 $l{\cdot}min^{-1}$ Ar flow-rate, 10 ppm liquid solution of the easily ionisable element nebulised into the plasma. It was found that the plasma becomes "colder", the relative changes in T_{rot} were found to be: 1.29 % (Li), 1.7 % (Ca), 1.8 % (K) and 2.9% (Na). One can see that the presence of any of these elements will not cause significant lowering of the rotational temperature. The highest decrease (2.9 %, 78 K) in the case of Na represents the most important change in the temperature.

The spectrum of the very low power RF CCP was investigated in various experimental conditions in the wavelength region of 306-323 nm, with a major focus on the OH bands.

Thus, at an observation heigth of 12 mm, at an RF power of 50 W and gas flow-rate of 0.7 $l{\cdot}min^{-1}$ the plasma spectra are presented in Fig. 9. Fig. 9a presents the 100 % Ar plasma spectrum with deionised, bidistilled water nebulised into the plasma, corresponding to a rotational temperature of 2425 K. In Fig. 9b the spectra of a 100 % air plasma is presented in two different conditions: with (2752 K) and without (2690 K) deionised, bidistilled water nebulised into the plasma. The Ar plasma was found to be cooler, but with more intense lines and noisier background than in the air plasma. Naturally, water entrance into the air plasma caused an increase in T_{rot}.

The OH spectrum for the 100 % Ar plasma without deionised, bidistilled water nebulised into the plasma is missing. This situation is due to the fact that, the Ar plasma is very unstable and noisy without water introduction into the plasma. The influence of plasma gas content on the OH spectrum is presented in Fig. 10 (12 mm above the tip, 50 W RF power and 0. 7 $l{\cdot}min^{-1}$ gas flow-rate) with the following features: 100 % Ar - 2425 K; 57 % Ar + 43 % air - 2877 K; 100 % air - 2881 K.

Synthetic OH spectra were obtained via computer simulation using *simOH* [33]. The computer simulated and experimental spectra are presented in Fig. 11 (Ar CCP 2720 K, superficial luminescence, 60 W, 0. 7 $l{\cdot}min^{-1}$, Gaussian apparatus function with full width at 1/e of the maximum of 30 pm, all line relative intensities were normalized to the most intense line in the band, denoted Q_19, at 309. 2394 nm).

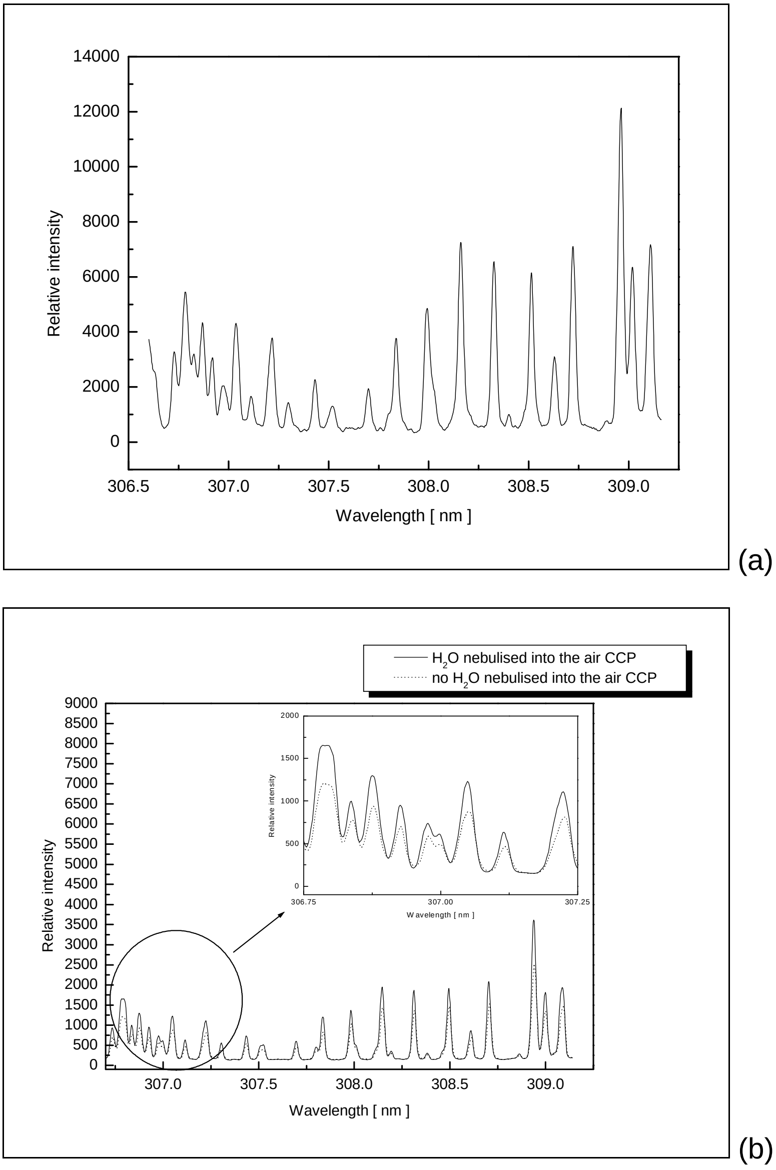

Fig. 9. *– OH spectrum: Ar plasma with H_2O (a), air plasma with and without H_2O (b)*

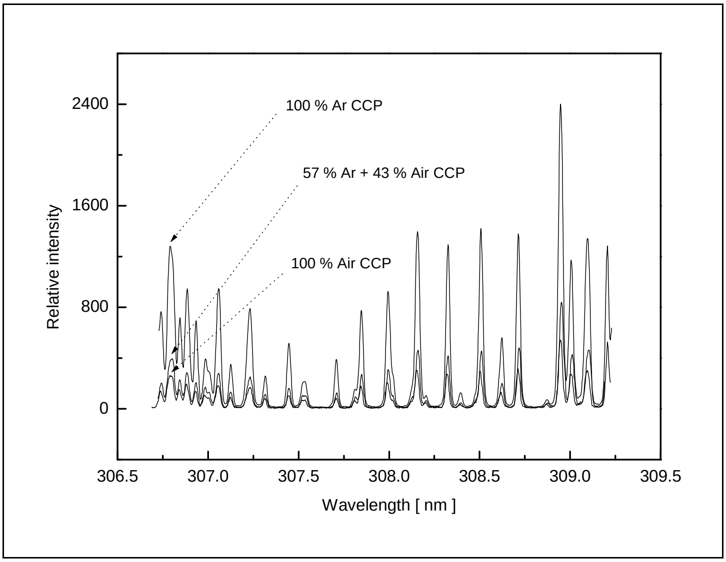

Fig. 10. *– Influence of plasma gas content on the plasma spectrum*

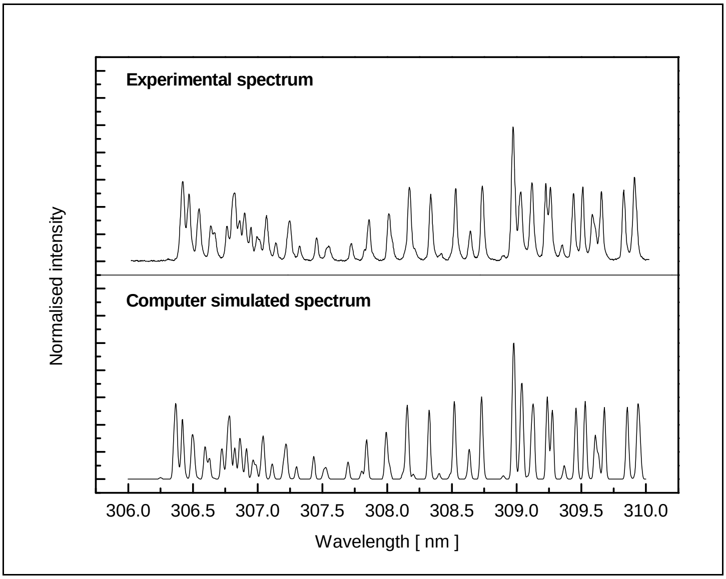

Fig. 11. *Experimental and computer simulated spectra for* $T_{rot} = 2720K$

The experimental and computer simulated synthetic spectra are similar in shape, with two major differences: a noisier background and broadened lines for the experimental spectra. These "imperfections" of the experimental spectra are due to the ideal character of the synthetic spectra:

noises are not included (the relative value of the background being equal to 0) and the lines (Dirac impulses) are broadened only by the apparatus function, the basic physical phenomena (motions, collisions, etc.) being ignored. The good agreement between experiment and simulation supports the calculated values of T_{rot} and make applicable the simulation software *simOH* to the very low power CCP.

4. CONCLUSIONS

This paper demonstrates that a very low power capacitively coupled plasma (5-75 W, 13. 56 MHz) could be ignited and maintained on a kanthal tip with a diameter of 0. 8 mm (the authors previously showed that a CCP could not be ignited below 135 W on a conical tip with a tip angle of 60^o [16]). The very low power CCP was characterized from physical point of view, by means of rotational temperatures of the OH band (A $^2\Sigma^+$, $\nu = 0 \rightarrow$ X $^2\Pi$, $\nu' = 0$, at 306. 357 nm) as function of radiofrequency power, observation height, radial position, gas flow-rate and gas composition. The experimental spectra was compared to computer simulated syntethic spectra and found in good agreement. The temperatures determined from the OH (0, 0) spectra are in good agreement with temperatures obtained for other plasma spectral sources. They are similar, in dependency on operating conditions and observation modes, to the rotational temperatures determined in a capacitively coupled microwave (CMP) plasma by Masamba et al. [34] or in the furnace atomization plasma excitation spectroscopy source (FAPES) investigated by Le Blanc and Blades [35]. The rotational temperature values (2150-2760 W) are similar to those measured in He CMP (1800-3000 K) but higher the those from He FAPES (580-1400 K). Compared to inductively coupled plasmas (ICP), one can tell that, as it was expected, our rotational temperature are smaller than those in the ICP (2800-4700 K, 27. 13 MHz and 1. 3 kW RF power, 0-35 mm observation heights [36]).

Acknowledgements. This research was supported by Research Grants no.: 30/32575/1999, 26/292/2000 and 19/374/2001 of the National Council for Universitary Research (CNCSIS).

REFERENCES

[1] K. Baxter, *RadioNews* 1204, 1928.
[2] Y. Asami, T. Hori, *Nature* **144**, 981, 1939.
[3] G. D. Cristescu and R. Grigorovici, *Bull. Soc. Roum. Phys*. **42**, 37, 1941.
[4] G. I. Babat, *J. Instr. Electr. Eng. (London)* **94**, 27,1947.
[5] T. B. Reed, *J. Appl. Phys.* **32**, 821, 1961.

[6] S. Greenfield, I. L. Jones and C. T. Berry, *Analyst* **89**, 713-720, 1964.

[7] R. H. Wendt and V. A. Fassel, *Anal. Chem.* **37**, 920, 1965.

[8] D. C. Liang and M. W. Blades, *Anal. Chem.* **60**, 27, 1988.

[9] B. M. Patel, J. P. Deavor and J. D. Winefordner, *Talanta* **35**, 641, 1988.

[10] D. C. Liang and M. W. Blades, *Spectrochim. Acta.* **44B**, 1059, 1989.

[11] D. Huang and M. W. Blades, *J. Anal. At. Spectrosc.* **6**, 215, 1991.

[12] D. C. Liang, D. Huang and M. W. Blades, *J. Anal. At. Spectrosc.* **4**, 789, 1991.

[13] E. Tataru, S. D. Anghel and I. I. Popescu, *Rev. Roum. Phys.* **39**, 29, 1991.

[14] S. D. Anghel, *Studia Univ. "Babes-Bolyai" Cluj, Physica*, **XXXVIII**, nr. 1, 39, 1993.

[15] M. W Blades, Spectrochim. Acta **49B**, 47, 1994.

[16] E. A. Cordos, S. D. Anghel, T. Frentiu and A. Popescu, *J. Anal. At. Spectro*m **9**, 635-641, 1994.

[17] S. D. Anghel, E. Darvasi, T. Frentiu, A. M. Rusu A. Simon, and E. A. Cordos, *Fresenius Journ. Anal. Chem.* **355**, 250, 1996.

[18] S. D. Anghel, T. Frentiu, A. M. Rusu, L. Bese, and E. A. Cordos, *Fresenius Journ. Anal. Chem.* **355**, 252, 1996.

[19] T. Frentiu, A. . M. Rusu, M. Ponta, S. D. Anghel, and E. A. Cordos, *Fresenius Journ. Anal. Chem.* **355**, 254, 1996.

[20] E. A. Cordos, T. Frentiu, A. M. Rusu, S. D. Anghel, A. Fodor and M. Ponta, *Talanta* **48**, 827, 1999.

[21] S. D. Anghel, T. Frentiu, A. M. Rusu, A. Popescu, A. Simon, and E. A. Cordos, *Acta Chimica Hungarica - ACH Models in Chemistry* **136**, 131, 1999.

[22] T. Frentiu, A. M. Rusu, S. D. Anghel, A. Popescu, S. Negoescu, A. Simon, and E. A. Cordos, *Acta Chimica Hungarica - ACH Models in Chemistry* **136**, 119, 1999.

[23] S. D. Anghel, E. A. Cordos, T. Frentiu, A. Popescu and A. Simon, *J. Anal. At. Spectrom* **14**, 541, 1999.

[24] S. D. Anghel, *IEEE Trans. on Plasma Sci.* ¸ - accepted for publication, 2002.

[25] G. D. Cristescu and R. Grigorovici, *Com. Acad. RPR* **5**, 515, 1955.

[26] G. D. Cristescu and R. Grigorovici, *R. Rev. Phys*. **1**, 103, 1956.

[27] S. D. Anghel, Ph. D. Thesis, Babes-Bolyai University, 1991

[28] A. G. Gaydon, *Spectroscopy of Flames*, London: Chapman and Hall, 1957

[29] S. Pellerin, J. Koulidiati, O. Motret, K. Musiol, M. de Graaf, B. Pokrzywka and J. Chapelle, *High Temp. Material Processes* **1**, 493, 1997

[30] F. Bastien, in *Electrical Breakdown and Discharges in Gases: Macroscopic processe and Discharges*, Eds. E. E. Kunhardt and L. H Luessen, New York, Plenum Press, 1983, Ch. 7

[31] Ch. de Izarra, *Int. J. of Modern Phys. C* **11**, no. 5, 987, 2000

[32] D. Levin, Ch. O. Laux and Ch. H. Kruger, *J. Q. S. R. T.* **61**, no. 3, 377, 1999

[33] G. Dilecce, M. Simekand S. De Benedictis, *J. Phys. D: Appl. Phys* **34**, 1799, 2001

[34] W. R. L. Masamba, A. H. Ali and J. D. Winefordner, Spectrochim. Acta **47B**, 481, 1994

[35] C. W. Le Blanc and M. W. Blades, Spectrochim. Acta **50B**, 1395, 1995

[36] H. Kawaguchi, T. Ito and A Mizuike, Spectrochim. Acta **36B**, 615, 1981

STUDIA UNIVERSITATIS BABEŞ-BOLYAI, PHYSICA, XLVII, 1, 2002

AMORPHOUS LANTHANUM ALUMINOBORATES INVESTIGATED BY THERMAL ANALYSIS AND FTIR SPECTROSCOPY

S. SIMON[1], **R. GRECU***, **V. SIMON**[1]

ABSTRACT. Amorphous lanthanum aluminoborate samples prepared by sol-gel technique have been characterized by thermal analysis and IR spectroscopy. Thermal analysis showed that continuous weight losses take place up to 800°C as a result of nitrates decomposition, glycerol pyrolysis and dehydroxylation. The crystallization of amorphous xerogels took place between 760°C and 860°C. From FTIR measurements it results that in amorphous lanthanum aluminoborate xerogels aluminum occurs as hexa-, penta- and tetracoordinated and boron occurs as three- and tetracoordinated by oxygens. The main aluminum species is pentacoordinated while boron appears mainly as threecoordinated.

Introduction

Lanthanoborate glasses are interesting for their high refractive index and low-dispersion optical applications [1-3]. The addition of Al_2O_3 improves the glass-forming tendency and aqueous durability [3]. Up to now only one stable crystalline phase is known in the ternary lanthanum-aluminum-boron system [4]. The composition of this crystalline phase is $LaAl_{2.03}B_4O_{10.54}$ (124) and in its structure the La, Al and B atoms are surrounded by O atoms in trigonal prismatic, pyramidal and tetrahedral arrangements, respectively. It is an interesting oxide compound in which all cations exhibit unusual coordination: lanthanum is only hexacoordinated, aluminum only five coordinated and boron only tetracoordinated.

The local arrangements in the structural disordered borates have been investigated by different techniques like nuclear magnetic resonance [5-9], Raman [10, 11] and infrared spectroscopies [12-14]. The structural disordered form of the oxide compound with a composition corresponding to $LaAl_{2.03}B_4O_{10.54}$ crystalline phase can be obtained by quickly undercooling of the mixture melted at 1400°C or by sol-gel procedure [15]. The last method is much proper for following the local structural changes during the transformation from disordered system to the well-defined crystalline phase.

---

[1] *Babes-Bolyai University, Faculty of Physics, 3400 Cluj-Napoca, Romania*
* *Raluca Ripan Institute of Chemistry, 3400 Cluj-Napoca, Romania*

In this paper we have used thermal analysis and Fourier Transform Infrared Spectroscopy (FTIR) to characterize the local structure evolution by heat treatment up to 750°C in iron doped amorphous lanthanum aluminoborate xerogels of composition $LaAl_2B_4O_{10.5}$.

Experimental

The investigated system $1\%Fe_2O_3\cdot 99\%[LaAl_2B_4O_{10.5}]$ (mol %) was prepared by sol-gel method [15] from aqueous solution of $La(NO_3)_3\cdot 6H_2O$, $Al(NO_3)_3\cdot 9H_2O$, H_3BO_3 and Fe_2O_3 of analytical purity grade by thermal decomposition of starting nitrates and boric acid accompanied by simultaneous oxidation of glycerol. The reagents mixture solved in desalinized water appears as a transparent solution at room temperature. A viscous gel is obtained after 5 hours heating at 95°C. The further heating at this temperature leads to a spongious solid sample. Xerogel samples were obtained after heat treatment for 30 minutes at different temperatures, T_t, between 150 and 750°C.

The IR spectra were recorded on a FT/IR-610 JASCO spectrometer at room temperature in the wavenumbers range from 400 to 4000 cm^{-1} using the KBr disk technique. Due to the high hygroscopicity of KBr it was difficult to avoid the water adsorption during the prolonged grinding of powdered sample in KBr. The thermal analysis was realized up to 1000°C using a MOM derivatograph.

Results and discussion

The results of thermal analysis for xerogel sample obtained after a 30 minutes stage at 150°C are presented in Fig. 1. The thermogravimetric (TG) curve shows that up to 800°C the weight of the sample is decreasing as effect of losing water, nitrogen oxides and CO_2 resulted from nitrates decomposition and glycerol pyrolysis and later as effect of dehydroxylation. From differential thermogravimetry (DTG) we can easy identify the temperature at which the first two main losses take place: the nitrates decomposition at about 150°C and the glycerol pyrolysis around 210°C. Beside these events from differential thermal analysis (DTA) it is possible to evidence the structural changes that appear above 750°C when the crystalline phases are developing. This process starts at 760°C and different changes appear up to 950°C as result of successive phase transformations to the final crystalline phase of composition $LaAl_{2.03}B_4O_{10.5}$ as was confirmed by X-ray diffraction studies. The xerogels resulted after heat treatments applied at temperatures up to 750°C are without any crystalline phase.

The FTIR spectra of the investigated samples are given in Fig. 2. The spectra profile with large bands is typical for disordered systems.

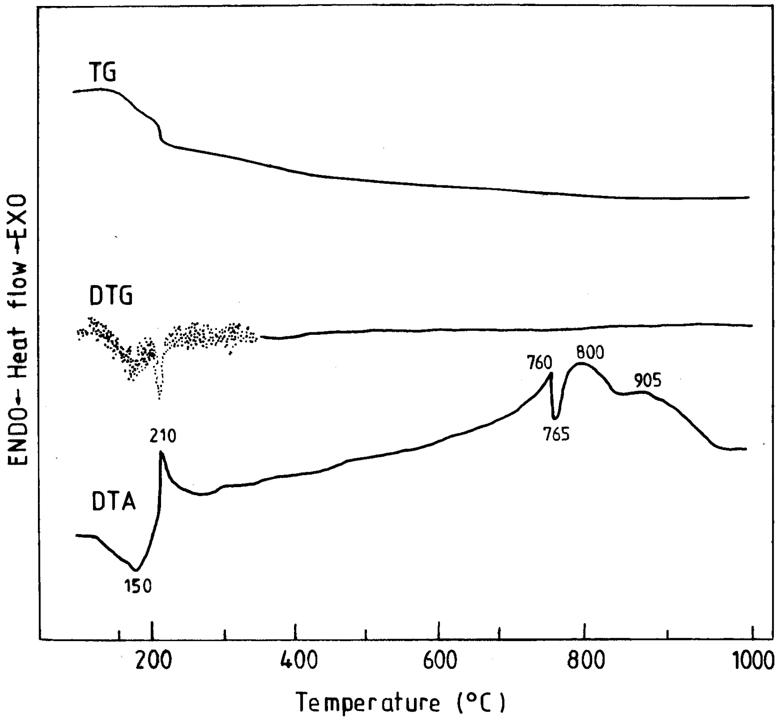

Fig. 1. *Differential thermal analysis curve for the sample heat treated at 150^{0}C.*

In spectrum of the sample heated at 150^{0} C for 30 minutes, the intense broad band at ~ 3430 cm^{-1} is assigned to stretching vibrations of the OH groups from crystallization water remained in samples from the starting reagents, from the physically adsorbed water either on the pore walls of the samples or on KBr. The intensity of this band gradually decreases and for samples heated above 410^{0} C it is mainly due to water adsorbed during the preparation of KBr disks. The band corresponding to bending vibration from water is observed at ~ 1630 cm^{-1} in all spectra.

The two weak bands at 2923 and 2853 cm^{-1} correspond to the asymmetric and symmetric stretching vibrations of the CH_2 groups, are observed in spectra of all samples and arise from the organic impurities occurring in KBr.

Coming back to the spectrum of the sample with T_t = 150^{0} C, the shoulder at ~ 3250 cm^{-1} can be assigned to hydroxyl groups involved in hydrogen bonding, most probably of B–OH type [16]. The two bands at 1642 and 1686 cm^{-1}, still observed for xerogels with T_t <600^{0}C confirm the nitrates (NO_3 $^{-}$) decomposition with the formation of nitrito [–O–N = O], nitrosyl

[$(NO)^+$] or nitrato (–O–NO_2) compounds [17]. In the last case, the maximum observed at 1318 cm^{-1} can be assigned to symmetric stretching of NO_2 group. The sharp peak at 1384 cm^{-1} indicates that, at this stage, a part of aluminum nitrate starting reagent is still present; it will disappear by further thermal treatment.

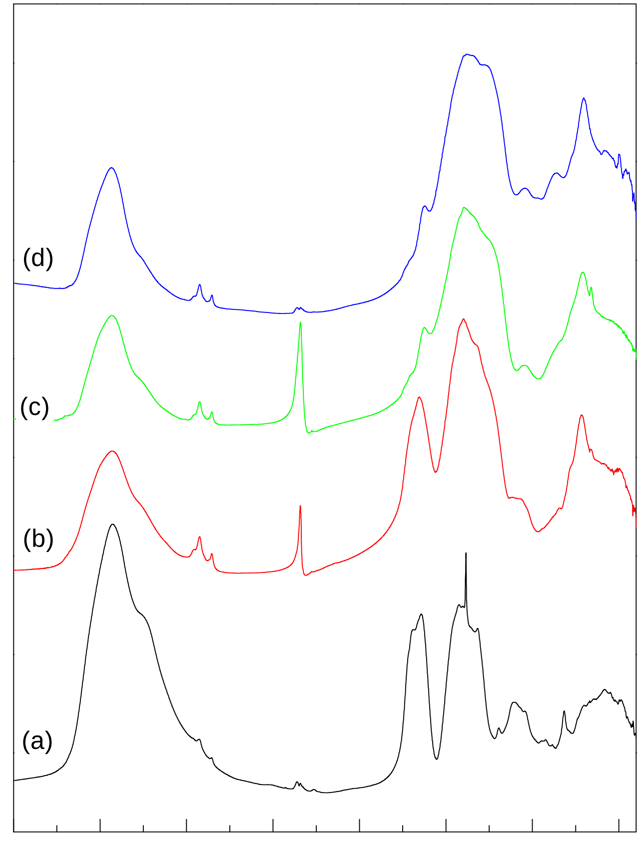

Fig. 2. *IR absorbance spectra of $LaAl_2B_4O_{10.5}$ xerogel samples heat treated at 150 (a), 410 (b), 600 (c) and 760°C (d).*

Around 2350 cm^{-1} a weak doublet is present in all spectra and is due to atmospheric CO_2 molecules. Superimposed on this doublet, the spectra of samples obtained after 30 minute stage at 410°C and 600°C contain an intense sharp peak (2342 cm^{-1}) assigned to compounds containing the NO–B– groups generated by glycerol combustion in the presence of nitrogen oxides resulted by nitrates decomposition at lower temperature but still present in the pores of xerogels. Such unusual reactions can be explained by the fact that in the closed pores there is not enough oxygen for a complete oxidation of the glycerol fragments.

The rise of treatment temperature to 410 ^{0} C has as effect the broadening of the bands observed at ~ 1652 cm^{-1} and ~ 1400 cm^{-1} . The last one become the most intense in the spectrum and under his envelope new bands with frequency shifted to lower frequency are detected, showing changes in the structure of the units involving boron.

Crystalline and non-crystalline borates are known to consist of different structural arrangements, which are composed of BO_3^{3-} triangles and BO_4^- tetrahedra with or without nonbridging oxygen ions [12]. The absorption bands in the infrared spectra of borate glasses are generally assigned to vibrational modes of BO_3^{3-} and BO_4^- units present in the structural grouping like boroxol, pentaborate, triborate, diborate, ring-type metaborate, chain-type metaborate, pyroborate and orthoborate [11]. The IR bands in the 1500 to 1100 cm^{-1} and 700 to 600 cm^{-1} ranges have been assigned to B-O stretching and out-of-plane bending vibrations of BO_3 units, respectively. The bonds in the range from 800 to 1100 cm^{-1} have been assigned to B-O stretching in BO_4 tetrahedral units [1, 2, 12-14]. Having these in mind we can try to describe the evolution of local surrounding of boron from amorphous xerogels by increasing the heat treatment temperature, before to become crystalline.

The band located at ~1400 cm^{-1} in spectrum of sample with T_t = 150°C is assigned to BO_3^{3-} units or to compounds resulting from the reaction between boric acid and glycerol. When the heat treatment temperature increases new bands at lower wave numbers are identified: ~ 1330 cm^{-1} for the sample treated to 410^0 C, ~ 1330 and ~ 1260 cm^{-1} for the sample heated to 600^0 or 750^0 C. This is partially due to the local distributions that take place when the dry xerogels are developing and surface hydroxyls are removing.

The relatively weak and large bands centered at about 1050 and 860 cm^{-1}, well observed in spectrum of sample with T_t = 750°C can be attributed to the BO_4^- tetrahedra.

The correlation between IR absorption bands and different types of aluminate polyhedra is based on IR results obtained for aluminate crystals. The Al-O stretching vibrations of tetrahedral AlO_4 groups are related with the bands in the region 900 – 750 cm^{-1} and the bands in 650 – 400 cm^{-1} region are associated with stretching modes of AlO_6 octahedra. Between these two relatively large regions some bands appear for the compounds with pentacoordinated aluminum [18].

It is well known [19, 20] that in amorphous aluminate xerogels there are, almost independent on composition, three types of aluminum: tetra-, penta- and hexacoordinated; therefore in the studied amorphous xerogels are expected bands from all these aluminum species. Inspecting the IR spectra region below 900 cm^{-1}, region with contributions from the aluminum polyhedra, one remarks first a relatively narrow peak at 820 cm^{-1} for the sample heat treated at 150^oC, peak assigned to Al-OH bonds from aluminum hydrate that also gives the peak around 1110 cm^{-1} [21]. For the same sample in the region between 600 and 450 cm^{-1} there is a broad band related to the AlO_6 octahedra. For the next three samples, obtained after heat treatments at 410, 600 and 750^oC, the main band is centered at 710 cm^{-1} and can be assigned to the pentacoordinated aluminums. A relatively weak contribution from the AlO_4 tetrahedra can be identified as a shoulder on the left side of the peak at 710 cm^{-1}.

Conclusions

The thermogravimetric analysis indicates that the main weight losses in lanthanum aluminoborate xerogels synthesized by sol-gel method take place between 150 and 300^oC as result of reagents decomposition and of glycerol oxidation. The weight looses continue up to 800^oC due to dehydroxylation of samples.

The FTIR spectroscopy studies evidence in all investigated samples the occurrence of boron in BO_3 triangles and BO_4 tetrahedra and of aluminum in polyhedra corresponding to tetra-, penta- and hexacoordinated aluminum. The main aluminum species is pentacoordinated while borons appear mainly as threecoordinated. Both physically adsorbed water and compounds resulted by nitrates decomposition and glycerol pyrolysis are identified in the spectra recorded from samples obtained after heat treatments at 150 and 410^oC, that is in agreement with the sequences of sol-gel synthesis procedure.

REFERENCES

1. I. N. Chakraborty, D. E. Day, J. C. Lapp, J. E. Shelby, J. Am. Ceram. Soc. 68, 7, 368 (1985).
2. I. N. Chakraborty, D. E. Day, J. Am. Ceram. Soc. 68**,** 12, 641 (1985).
3. R. K. Brow, D. R. Tallant, G. L. Turner, J. Am. Ceram. Soc. 80, 5, 1239 (1997).
4. P. Yang, W. Yu, J. Y. Wang, J. Q. Wei, Y. G. Liu, Acta Cryst. C54, 11 (1998).
5. P. E. Stallworth, P. J. Bray, in Glass Science and Technology, Eds. D. R. Uhlmann and N. J. Kreidl, Acad. Press Inc. , Boston (1990) p. 77-100.

6. B. C. Bunker, R. J. Kirkpatrick, R. K. Brow, G. L. Turner, C. Nelson, J. Am. Ceram. Soc. 74, 6, 14, 30 (1991).
7. R. K. Brow, D. R. Tallant, G. L. Turner, J. Am. Ceram. Soc. 79, 9, 1410 (1996).
8. S. Simon, G. J. M. P. van Moorsel, A. P. M. Kentgens, E. de Boer, Solid St. NMR, 5, 163 (1995).
9. L. Züchner, J. C. C. Chan, W. Müller Warmuth, H. Eckert, J. Phys. Chem. B, 102, 4495 (1998).
10. W. L. Konijnendijk, J. M. Stevels, J. Non-Cryst. Solids, 18, 307 (1975).
11. B. N. Meera, J. Ramakrishna, J. Non-Cryst. Solids, 159, 1 (1993).
12. J. Krogh-Moe, Phys. Chem. Glasses, 6, 2, 46 (1965).
13. E. I. Kamitsos, A. P. Patsis, M. A. Karakassides, G. D. Chryssikos, J. Non-Cryst. Solids, 126, 52 (1990).
14. Y. M. Moustafa, H. Doweidar, G. El-Damrawi, Phys. Chem. Glasses, 35, 2, 104 (1994).
15. F. Abbattista, A. Delmarstro, G. Gozzelino, D. Mazza, M. Vallino, G. Busca, V. Lorentzelli, J. Chem. Soc. Faraday Trans. , 86, 3653 (1990).
16. C. J. Brinker, B. M. Haaland, J. Am. Ceram. Soc. , 66, 758 (1983).
17. K. Nakamoto, Infrared Spectra of Inorganic and Coordination Compounds, John Wiley and Sons, Inc. , New York – London, 1963. .
18. B. T. Poe, P. F. McMillan, C. A. Angell, R. K. Sato, Chem. Geology, 96, 333 (1992).
19. S. Simon, A. van der Pol, E. J. Reijerse, A. P. M. Kentgens, G. J. M. P. van Moorsel and E. de Boer, J. Chem. Soc. Faraday Trans. , 97, 4756 (1994).
20. D. Iuga, S. Simon, A. P. M. Kentgens, E. de Boer , J. Phys. Chem. B, 3, 103 7591 (1999).
21. A. Vazguez, T. Lopez, R. Gomez, A. Morales, O. Novaro, J. Solid St. Chem. , 128, 161-168 (1997).

STUDIA UNIVERSITATIS BABEŞ-BOLYAI, PHYSICA, XLVII, 1, 2002

AM1/INDO SEMIEMIPRICAL CALCULATIONS ON TYROSYL RADICAL

V. CHIŞ[1]

ABSTRACT. Semiempirical calculations are used to obtain the hyperfine coupling constants (hcc's) for phenol ring and β-methylene protons in tyrosyl radical. Unpaired spin distribution in the aromatic ring has been calculated by the two-center dipole approximation for the radical produced in different systems. A comparison is made between the geometry of the radical optimized by the semiempirical Austin Model 1 (AM1) and the parent molecule. Proton hyperfine coupling constants are calculated by Intermediate Neglect of Differential Overlap (INDO) method for comparison with experimental determinations.

Introduction

Amino-acid radicals are important intermediates in a large variety of biochemical processes[1-3]. Particularly, the stable tyrosyl radical produced by oxidization of tyrosine molecule is essential for the catalytic activity of ribonucleotide reductase (RNR)[3.4] and it is shown to participate in the charge transfer pathways of several biological systems[5-10]. In RNR and Photosystem II (PSII) the tyrosyl side chain is located in the vicinity of a transition metal with redox activity that is essential for biological functions. The tyrosyl radical in biological systems are known to form covalent cross-links between DNA and proteins, catalyze a number of biosynthetic reactions and serve as an electron transfer intermediate in photosynthesis[11].

To identify and characterize the tyrosyl radical found in different systems, a great number of experiments have been carried out by electron paramagnetic resonance (EPR), electron nuclear double resonance (ENDOR) or vibrational spectroscopy[11-18]. Detailed experimental data have been obtained about the hyperfine structure, unpaired spin distribution, conformation and vibrational properties of the radical so that it became a well suited "prototype" on which the accuracy of different semi- and non-empirical methods in predicting its properties can be tested.

The principal values of the hyperfine tensors relative to ring protons are similar in the radicals detected in various systems, while the differences in the values of the tensors relative to the β-methylene protons are due to the different orientations of this group with respect to the phenol ring plane.

---

[1] *"Babeş-Bolyai" University, Faculty of Physics, 1, Kogălniceanu, RO-3400 Cluj-Napoca, Romania*

A number of theoretical studies, ranging from semiempirical to sophisticated Density Functional methods are also reported on model tyrosyl radicals[19-24]. Both, experimental and theoretical studies revealed very similar geometries for this radical in different systems. It is also generally proved that the spin density distribution follows an odd-alternant pattern, being localized in the phenol ring of the radical, mainly at C1, C3 and C5 positions. This spin density map is typical for alkyl-substituted phenoxyl radical, irrespective of the detailed alkyl substituent to ring carbons. Moreover, neither the methylene bridge conformation nor delocalized solvent interactions influence significantly the distribution of spin density in the tyrosine radicals.

Due to the difficulty of obtaining accurate hyperfine couplings using elaborate computationally expensive and time consuming *Ab Initio* and Density Functional methods, this work is intended to test the ability of semiempirical methods to calculate the geometry and hyperfine coupling constants for the tyrosyl radical and the possibility to extrapolate this kind of studies to other molecules of biological relevance.

Results and discussions

Spin densities from hyperfine coupling tensors

The magnitude of the isotropic component of an α-proton hyperfine coupling tensor $^{\alpha}a$ was suggested to vary directly as the lone electron orbital (LEO) spin density[25]

$$^{\alpha}a = Q_{CH}^{H}\rho \qquad (1)$$

The equations for the three dipolar components of the total hyperfine tensor $^{\alpha}A$ are given below

$$\begin{aligned} B_x &= K\rho(2R_H^2 - R_p^2)/(R_H^2 + R_p^2)^{5/2} \\ B_y &= -K\rho/(R_H^2 + R_p^2)^{3/2} \\ B_z &= K\rho(2R_p^2 - R_H^2)/(R_H^2 + R_p^2)^{5/2} \end{aligned} \qquad (2)$$

These are derived for a planar radical with the unpaired electron in a 2p orbital, as shown in Fig.1. R_p is the distance from the carbon nucleus to the effective center of the 2p orbital lobe, above or below the nodal plane and R_H is the $^{\alpha}$H-C bond length. The xy plane is the nodal plane of the 2p orbital.

The unpaired electron is located at two effective centers, above and below the radical plane on the LEO axis of symmetry. With R_H and R_p in Å and $B_{x,y,z}$ in units of MHz, the value of K is[26] 78.8MHz/Å^3. From the above equations one can obtain the expressions for R_H and R_p

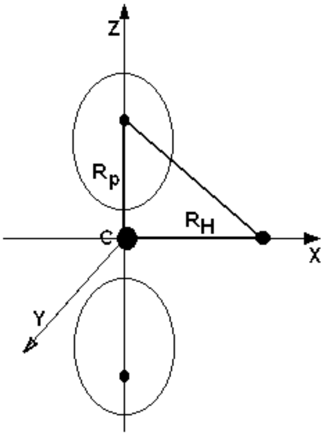

Fig. 1. *Diagram of a planar π radical defining the variables in Eq. (2)*

$$R_H^2 = \left(-\frac{K\rho}{B_y}\right)^{2/3} \cdot \frac{B_y - B_x}{3B_y} \qquad (3)$$

$$R_p^2 = \left(-\frac{K\rho}{B_y}\right)^{2/3} \cdot \frac{B_y - B_z}{3B_y}$$

Given an $^{\alpha}$A tensor and the spin density ρ one can use the above equations to calculate R_H and R_p. The best choice of the dipolar elements of the tensor to be used as a measure of the unpaired spin density is B_x due to the fact that it is least affected by changes in free radical geometry[26]. Thus, ρ is determined by the following equation

$$B_x = Q^{dip}\rho \qquad (4)$$

where the Q^{dip} proportionality constant is chosen empirically and the value 38.7MHz was found by Gordy[27] to reproduce a large range of free radicals when calculating the dipolar elements of the hyperfine coupling tensors.

We used this approach to estimate the unpaired spin density in the phenol ring of the tyrosyl radicals in biological systems using the hyperfine coupling tensors reported by different authors. The results are summarized in Table 1, and in Fig.2 is given the atom numbering scheme in the radical. For these calculations we used the following algorithm: ρ was calculated by using the eq. (4) and then R_H and R_p were obtained from eq. (3).

From Table 1, the medium spin densities are: 0.25 for the proton bonded to the C5 atom, 0.26 for the proton bonded to the C3 atom and 0.09 for the two protons at C2 and C6 positions. The medium carbon-proton bond length in the radicals are: 1.136Å, 1.151Å, 1.050Å and 1.050Å for H5, H3, H2 and H6 protons, respectively. All these values are slightly longer than their correspondents in the undamaged molecule and suggest a more relaxed geometry of the radical with respect to the parent molecule, as expected.

Finally, the medium R_p values are 0.701Å for C5-H5 bond, 0.695Å for C3-H3 bond and 0.725Å for C2-H2 and C6-H6 bonds. From Table 4 a value of -69 MHz is deduced for the Q constant which should be used in the McConnell equation for obtaining the unpaired spin density on C3 and C5 atoms from isotropic couplings of the protons directly bonded to them.

Table 1.

Bond lengths, effective spin centers and spin densities calculated from dipolar elements of $^{\alpha}$H hyperfine coupling tensors of tyrosyl radicals in different systems.

B_x (MHz)	B_z (MHz)	B_z (MHz)	$^{\alpha}a$ (MHz)	$\rho_{dip}$$^{(a)}$	R_H (Å)	R_p (Å)	$\rho_{iso}$$^{(b)}$	$-Q_{CH}^{H}$ (MHz)$^{($	Protons	System	Ref.
10.1	-1.7	-8.5	-17.5	0.27	1.150	0.696	0.25	66.0	3	L-TyrHCl	18
9.6	-1.5	-8.2	-17.0	0.25	1.139	0.701	0.25	68.0	5	L-TyrHCl	18
10.3	-1.6	-8.8	-18.1	0.27	1.136	0.702	0.26	68.0	3, 5	RNR	15
10.7	-1.5	-9.2	-19.7	0.28	1.132	0.704	0.28	71.3	3	N-ac-L-TyrHCl	13
9.3	-1.3	-8.0	-17.5	0.24	1.131	0.704	0.25	72.8	5	N-ac-L-TyrHCl	13
10.2	-2.1	-8.0	-17.4	0.26	1.197	0.676	0.25	66.0	3, 5	PSII	16
8.7	-0.8	-7.8	-17.4	0.22	1.104	0.714	0.25	77.4	3, 5	L-TyrHCl	12
10.2	-2.5	-7.8	-17.3	0.26	1.216	0.666	0.25	65.6	3	L-TyrHCl	28
10.1	-1.5	-8.7	-17.4	0.26	1.131	0.704	0.25	66.7	5	L-TyrHCl	28
9.8	-1.3	-8.6	-18.2	0.25	1.118	0.709	0.26	71.9	3, 5	PSII	17
3.2	0.3	-3.5	4.9	0.08	0.983	0.740	-0.07	-59.3	2, 6	RNR	15
3.3	0.4	-2.9	4.6	0.09	1.117	0.709	-0.07	-53.9	2, 6	PSII	17

(a)Calculated using eq. (4) with Q_{dip}=38.7MHz
(b)Calculated using eq. (1) with Q_{CH}^{H}=70.0MHz
(c)Calculated from eq. $^{\alpha}a/\rho_{dip}$

It should be noted that the accuracy of R_H and ρ_{dip} decrease for aromatic radicals due to the reduction in LEO spin density relative to other nearby sites of spin density. Even so, these values show consistent trends and they are in good agreement with those corresponding to other aromatic radicals[26], indicating in this case an electron loss radical type.

Calculated proton hyperfine coupling constants

In order to calculate the hyperfine coupling constants of the tyrosyl radical we used the AM1[29] and INDO[30] methods, this combination being the best choice for such a large molecule.

The hyperfine coupling constants of magnetic nuclei arises from the Fermi contact interaction between the unpaired electron and the nucleus and it is given by

$$A_n = \frac{2\mu_0}{3} g_e \mu_B g_n \mu_N \frac{1}{h a_0^3} Q(0) \tag{5}$$

There, A_n is in Hz, g_e and g_n are the electron and nuclear g factors, μ_B and μ_N are the Bohr and the nuclear magneton respectively, μ_0 is the vacuum magnetic permeability, h is the Planck constant, a_0 is the first Bohr radius and Q(0) represents the spin density at the nucleus n. Whereas

$g_e\mu_B g_n\mu_N \frac{1}{ha_0^3}$ is a constant for a specific nucleus, Q(0) has to be obtained from quantum theoretical calculations, based on the equation

$$Q(0) = \langle \Psi | \rho(r_n) | \Psi \rangle \tag{6}$$

where $\rho(r_n)$ is the spin density operator evaluated at the position of the nucleus n:

$$\rho(r_n) = \sum_k 2s_{zk}\delta(r_k - r_n) \tag{7}$$

r_k being the position vector of the k-th electron, s_{zk} is the individual electron spin angular momentum of the k-th electron, and δ(r) is the Dirac delta function.

All calculations were performed with the electronic structure program Gaussian 94[31]. First, we performed a full geometry optimization of the radical, starting from the geometry of the parent molecule, as obtained from neutron diffraction data[32].

However, in this geometry optimization the radical is supposed to be in gas phase and the matrix effects are not considered. We indirectly accounted for these effects via the available experimental data, by performing a new partial optimization setting the C-H bond lengths of the aromatic ring to the values obtained from experimental data by using the two-center dipole approximation (see Table 1). H7C7C1C6 dihedral angle has been obtained from isotropic hyperfine coupling constants of the H7 proton[18]. To take into account that the phenol oxygen is involved in a hydrogen bond interaction with nearby residues, a fixed value of 1.310Å was used for C4-O4 bond, as reported by Himo *et al.*[22] from a modeling hydrogen bonding study on a model tyrosyl radical. The resulted partial optimized geometrical parameters are given in Table 2, together

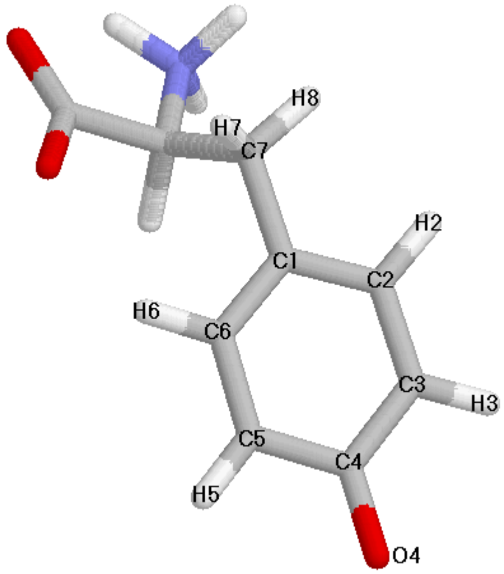

Fig. 2. *Optimized geometry of the tyrosyl radical (see text).*

Table 2.

Selected geometrical parameters of the tyrosyl radical and L-tyrosine-HCl molecule

Geometrical parameters	Parent molecule	Radical optimized geometry
Bond length		
C1C2	1.393	1.418
C2C3	1.394	1.379
C3C4	1.382	1.458
C4C5	1.393	1.459
C5C6	1.391	1.378
C6C1	1.393	1.420
C4O4	1.374	1.310*
C1C7	1.509	1.483
C1H7	2.146	2.153
C2H2	1.074	1.050*
C3H3	1.091	1.151*
C5H5	1.086	1.136*
C6H6	1.091	1.050*
C7H7	1.085	1.129
C7H8	1.080	1.124
Bond angles		
C1C2C3	121.0	120.6
C2C3C4	119.6	121.4
C3C4C5	120.0	116.3
C4C5C6	119.7	121.3
C5C6C1	120.9	120.6
C6C1C2	118.5	119.8
C6C1C7	121.2	119.9
H2C2C3	119.7	120.2
H3C3C4	120.1	117.2
H5C5C6	120.5	121.4
H6C6C1	120.1	118.9
C1C7H7	110.6	110.3
C1C7H8	109.8	110.8
Dihedral angles		
H2C2C1C6	179.9	177.6
H3C3C4C5	179.0	178.2
H5C5C4C3	179.4	178.3
H6C6C1C2	179.7	177.9
H7C7C1C6	53.1	50.7*
H8C7C1C2	7.9	10.6

* parameters fixed during the partial optimization

with their counterparts in the neutral molecule. L-tyrosine-HCl has been chosen for comparisons due to the fact that the most available experimental ENDOR data concerning the tyrosyl radical refers to γ-irradiated single crystals of this molecule[12,13,18,28].

Significant differences between the radical geometry and the unoxidized tyrosine are noted. Bonds C2-C3, C5-C6 and C4-O4 become shorter, while C1-C2, C3-C4, C4-C5 and C6-C1 become longer. Small changes in the bond angles also accompany these bond lengths. The greatest modification is that of C3C4C5 angle, whose value decreases from 120.0° to 116.3°. These results indicate that the original aromatic ring system adopts a quinoid-like structure on radical formation, with bonds C2-C3 and C5-C6 being shorter than the other carbon-carbon bonds in the ring. On closer examination of the bond lengths it is observed that the C1-C2 and C6-C1 bonds are shorter than C3-C4 and C4-C5 bonds. This suggest more delocalisation in the upper part of the ring compared with the lower part. One explanation for these geometrical features can be found by examining the classical resonances structures[20] for the tyrosyl radicals (Fig. 3). In these resonance forms there is the greatest amount of double bond character for C5-C6, C4-O4 and C2-C3 and the least for C4-C5 and C3-C4. The shortening of the C5-C6, C4-O4, and C2-C3 bonds on oxidation can be qualitatively explained by the decreased electron density between these bonds in the oxidized form.

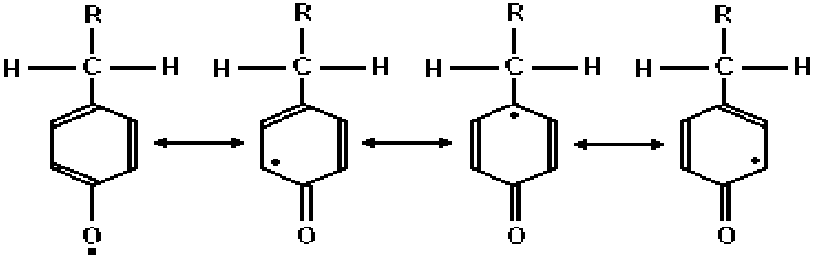

Fig. 3. Classical resonance structures for the tyrosyl radical

Table 3
INDO calculated hyperfine coupling constants of the ring and β-methylene protons*.

Proton	Experimental	INDO//AM1
H3	-17.4	-19.3
H5	-17.0	-18.2
H2	4.9	9.4
H6	5.4	9.1
H7	37.9	34.5
H8	2.3	2.1

* Values in MHz

The optimized geometry was then used in a subsequent INDO calculation to obtain the hyperfine coupling constants for the ring phenol and methylene protons. This method can provide accurate hyperfine coupling constants, if an accurate geometry is used for the radical[19,33] and this finding is confirmed in our study.

The hyperfine coupling constants calculated by INDO method are given in Table 3. The agreement between the experimentally determined hcc's by ENDOR spectroscopy and the calculated ones is good enough having in mind that in this calculations the radical is supposed to be in gas-phase and also, the hydrogen bonding effects are not directly considered. Especially good agreement is observed between the hcc's of the H3, H5, H7 and H8 protons. For H3 and H5 protons there is an appreciable amount of spin density on the corresponding carbon atoms in the ring. On the other hand, very small spin densities on C2 and C6 atoms are experimentally deduced, so that it is supposed that the unpaired spin densities in 1s orbitals of H2 and H6 atoms, from which the hcc's are calculated by INDO method, are greatly influenced by the spin densities from neighboring atomic centers C3 and C5, respectively. This influence results in an appreciable overestimation of the H2 and H6 hcc's.

The agreement is also very good for β-methylene protons. The isotropic part of a β-methylene coupling tensor is due predominantly to hyperconjugation between the aromatic π system of the ring and the 1s orbital on the hydrogen atom and it is described by McConnell relation[35]

$$A_{iso}=\rho_{\pi}B_2\cos^2\theta \tag{8}$$

where ρ_{π} is the unpaired spin density on the carbon atom bearing the odd electron (C1 in this case), B_2 is an empirical constant and θ represents the dihedral angle defined by the p_z orbital on the adjacent carbon on the aromatic ring and the C7-H bonds[34]. θ angle corresponding to H7 proton was estimated from ENDOR data using eq. (8) and then the dihedral angle H7C7C1C6 has been obtained. For H8 proton instead, the experimental studies generally report a very small value of the hyperfine coupling constant, which is explained by the orientation of C7H8 bond almost in the plane of the aromatic ring. Indeed, from optimized H8C7C1C2 dihedral angle, a value of 79.8^o is obtained for θ to be used in eq. (8) and then, with $\rho_{\pi}B_2$=63MHz[13], a hyperfine coupling constant of 2.0MHz is calculated for this proton. This result shows that McConnell relation holds very well in this case.

It should be noted that our semiempirical results are also in very good agreement with the Density Functional Calculations on model tyrosyl radical as reported by Himo *et al*.[22]

Conclusions

This study confirms that semiempirical calculation provide a very useful tool for obtaining the geometry and hyperfine coupling constants for rather big radicals like those involved in biological systems. The two-center dipole approximation is a simple, rapid and quite accurate method by which the unpaired spin density and C-H bond lengths can be quickly estimated. The AM1 optimization revealed minor differences between the parent molecule and radical geometry differences that are however reflected on calculated hcc's. The calculated hyperfine coupling constants by INDO method are in quantitative agreement with the experimental determinations for H3, H5 and β-methylene protons, while the unpaired spin densities in 1s orbitals of H2 and H6 atoms and hence their hcc's are greatly influenced by the spin densities on nearby atoms.

Due to the difficulty of obtaining accurate hyperfine coupling constants using more elaborate, computationally expensive and time consuming *Ab Initio* and DFT methods, this combination of AM1 and INDO methods should be preferred as an inexpensive and accurate approach of the hyperfine coupling determination for reasonably sized molecules.

Acknowledgements

This work has been possible due to a research fellowship performed under the CNR-NATO Outreach Fellowships programme of the Italian National Council of Research and it has been carried out at the "Universita Degli Studi di Padova, Dipartimento di Chimica Fisica".

REFERENCES

1. J. Z. Pedersen, A. Finazzi-Agro, *FEBS Lett.,* 325, 53 (1993).
2. J. A. Stubbe, W. A. van der Donk, *Chem. Rev*., 98, 705 (1998).
3. C. J. Easton, *Chem. Rev.,* 97, 53 (1997).
4. M. Fontecave, J. L. Pierre, *Bull. Soc. Chim. Fr*., 133, 653 (1996).
5. R. J. Hulsebosch, J. S. van den Brink, S. A. M. Nieuwenhuis, P. Gast, J. Raap, J. Lugtenburg, A. J. Hoff, *J. Am. Chem. Soc.,* 119, 8685 (1997).
6. P. Reichard, A. Ehrenberg, *Science*, 221, 514 (1983).
7. R. Karthein, R. Dietz, W. Nastainczyk, H. H. Ruf, *Eur. J. Biochem*, 171, 313 (1988).
8. B. A. Barry, G. T. Babcock, *Proc. Natl. Acad. Sci. USA*, 84, 7099 (1987).
9. M. M. Whittaker, J. W. Whittaker, *J. Biol. Chem.,* 265, 9610 (1990).
10. Ivancich, H. M. Jouve, B. Sartor, J. Gaillard, *Biochemistry*, 36, 9356 (1997).
11. Y. Qin, R. A. Wheeler, *J. Chem. Phys.,* 104, 1689 (1995).; Y. Qin, R. A. Wheeler, *J. Am. Chem. Soc.,* 117, 6083 (1995).
12. E. L. Fasanella, W. Gordy, *Proc. Natl. Acad. Sci. USA*, 62, 299 (1969).
13. Mezzetti, A. L. Maniero, M. Brustolon, G. Giacometti, L. C. Brunel, *J. Phys. Chem. A,* 103, 9636 (1999).
14. W. Hoganson, M. Sahlin, B. M. Sjoberg, G. T. Babcock, *J. Am. Chem. Soc.,* 118, 4672 (1996).
15. J. Bender, M. Sahlin, G. T. Babcock, B. A. Barry, T. K. Chandrashekar, S. P. Salowe, J. Stubbe, B. Lindstrom, L. Petersson, A. Ehrenberg, B. M. Sjoberg, *J. Am. Chem. Soc*., 111, 8076 (1989).
16. K. Warncke, G. T. Babcock, J. McCracken, *J. Am. Chem. Soc.,* 116, 7332 (1994).; K. Warncke, J. McCracken, *J. Chem. Phys.,* 101, 1832 (1994).
17. C. Tommos, X. S. Tang, K. Warncke, C. W. Hoganson, S. Styring, J. McCracken, B. A. Diner, G. T. Babcock, *J. Am. Chem. Soc.,* 117, 10325 (1995).
18. V. Chiş, A. L. Maniero, M. Brustolon, O. Cozar, L. David, Studia Physica, (submitted).
19. P. J. O’Malley, A. J. MacFarlane, *J. Mol. Struct. (Theochem).,* 277, 293 (1992).

20. P. J. O'Malley, A. J. MacFarlane, S. E. J. Rigby, J. H. A. Nugent, *Biochim. Biophys. Acta,* 1232, 175 (1995).
21. P. J. O'Malley, D. Ellson, *Biochim. Biophys. Acta,* 1320, 65 (1997).; P. J. O'Malley, *J. Am. Chem. Soc.,* 120, 11732 (1998).
22. F. Himo, A. Graslund, L. A. Eriksson, *Biophys. J.,* 72, 1556 (1997).
23. F. Dole, B. A. Diner, C. W. Hoganson, G. T. Babcock, R. D. Britt, *J. Am. Chem. Soc.,* 119, 11540 (1997).
24. M. Engstrom, F. Himo, A. Graslund, B. Minaev, O. Vahtras, H. Agren, *J. Phys. Chem.,* 104, 5149 (2000).
25. H. M. McConnell, J. Strathdee, *J. Mol. Phys.,* 2, 129 (1959).
26. W. A. Bernhard, *J. Chem. Phys.,* 81, 5928 (1984).
27. W. Gordy, Theory and Applications of Electron Spin resonance (Wiley, New York, 1980).
28. H. C. Box, E. E. Budzinski, H. G. Freund, *J. Chem. Phys.,* 61, 2222 (1974).
29. M. J. S. Dewar, E. G. Zoebisch, E. F. Healy, J. J. P. Stewart. *J. Am. Chem. Soc.,* 107, 3902 (1985).
30. J. A. Pople, D. L. Beveridge, P. A. Dobosh, *J. Am. Chem. Soc.,* 90, 4201 (1968).
31. Gaussian 94, Revision E. 2, M. J. Frisch, G. W. Trucks, H. B. Schlegel, P. M. W. Gill, B. G. Johnson, M. A. Robb, J. R. Cheeseman, T. Keith, G. A. Petersson, J. A. Montgomery, K. Raghavachari, M. A. Al-Laham, V. G. Zakrzewski, J. V. Ortiz, J. B. Foresman, J. Cioslowski, B. B. Stefanov, A. Nanayakkara, M. Challacombe, C. Y. Peng, P. Y. Ayala, W. Chen, M. W. Wong, J. L. Andres, E. S. Replogle, R. Gomperts, R. L. Martin, D. J. Fox, J. S. Binkley, D. J. Defrees, J. Baker, J. P. Stewart, M. Head-Gordon, C. Gonzalez, and J. A. Pople, Gaussian, Inc., Pittsburgh PA, 1995.
32. M. N. Frey, T. F. Koetzle, M. S. Lehman, W. C. Hamilton, *J. Chem. Phys.,* 58, 2547 (1973).
33. P. Smith, W. H. Donovan, *J. Mol. Struct. (Theochem).*, 204, 21 (1990).
34. W. Derbshire, *Mol. Phys*., 5, 225 (1962).; E. W. Stone, A. H. Maki, *J. Chem. Phys.,* 37, 1326 (1962).
35. N. M. Atherton, Principles of Electron Spin Resonance, (Ellis Horwood, London, 1993).

STUDIA UNIVERSITATIS BABEŞ-BOLYAI, PHYSICA, XLVII, 1, 2002

Ab Initio AND DFT STUDY ON HYPERFINE STRUCTURE OF 1,2-BENZOSEMIQUINONE ANION RADICAL

V. CHIŞ*, A. NEMEŞ*, L. DAVID*, O. COZAR*

ABSTRACT. The effects of different basis sets and computational methods on calculated isotropic hyperfine coupling constants (hfcc's) of 1,2-benzosemiquinone radical have been investigated for a set of eight solvents. The influence of the surrounding solvent molecules by their dielectric properties has been considered by applying the Onsager and isodensity polarizable continuum (IPCM) model. A very good quantitative agreement has been obtained between the computed hfcc's and the experimental ones, for all the solvents investigated, by an appropriate adjustment of the isosurface isodensity parameter in the IPCM model. For the gas-phase radical instead, it is found that Intermediate Neglect of Differential Overlap (INDO) method works better than Density Functional method for predicting hfcc's.

Introduction

Quinones represent important cofactors for electron transfer in photosynthesis, acting as electron acceptors in the initial charge separation process [1]. In particular, directly covalently linked porphyrin-1,2-benzosemoquinone anion radicals are well studied model compounds for mimicking primary processes of photosynthesis having as aim a better understanding of the factors governing the photoinduced charge separation reactions as the mean of capturing and storing solar energy [2]. Moreover, redox active crown ethers including quinones are well suited for studies of electrochemically driven ion transport mechanisms [3]. This combination of redox and complexing reactions is also provided by ortho quinones due to their close lying oxygens [4].

In general, these relatively stable radicals are generated easily and may be studied by electron spin resonance (ESR) spectroscopy in a variety of solvents [5]. The ESR spectra provide the hyperfine coupling constants of magnetic nuclei and the line pattern of the spectrum can provide a good insight into the structure of these radicals. However, the experimental data have to be compared with their theoretical counterparts for a better understanding of the particular properties of the detected radicals. Moreover, the analysis is often complicated by a strong influence of the solvent on the observed ESR spectra, and the hyperfine coupling constants observed in

---

** Babeş-Bolyai University, Faculty of Physics, 1 Kogălniceanu,RO-3400 Cluj-Napoca, Romania*

solution frequently disagree with those predicated by quantum-chemical calculations on the free, isolated species. Theory may be of assistance through comparisons of observed and computed hyperfine coupling constants, which may lead to the assignment of plausible geometries, energies reaction barriers, transition states, charge and spin distributions and various other properties.

In the last decade, methods based on Density Functional Theory (DFT) are becoming an alternative approach for calculating hfcc's and this is due to considerably less computational cost and memory requirements than those of conventional correlated *Ab Initio* procedures [6,7,21,22]. In addition, due to their lower computational cost and hence to their ability to treat larger systems, DFT methods may be used to obtain more realistic descriptions of the interactions between radical systems and their surroundings by explicit consideration of the latter.

At least to our knowledge three theoretical studies are reported on benzosemiquinone (BSQ) anion radicals. Tripathi and coworkers [30] reported an unrestricted Hartree-Fock (UHF) *Ab Initio* study on the calculated hyperfine structure of 1,3-BSQ radical. O'Malley [8] reported hybrid density functional calculations on the 1,4-BSQ anion radical in its free and hydrogen bonded forms and Langgard and Spanget-Larsen [23] studied the influence of the solvent effects on the ESR spectra of 1,2- and 1,4- BSQ by using DFT approaches.

In this work we used INDO, *Ab Initio* and DFT molecular orbital calculations to examine the structure and hyperfine coupling constants of the 1,2-BSQ radical, shown in Fig.1 together with the atom numbering scheme used. We focussed on the influence of several solvents for which experimental data are available [5], on the molecular structure and the spin density distribution of the systems by using the Onsager model [9] and the more recent isodensity polarizable continuum model (IPCM) [10].

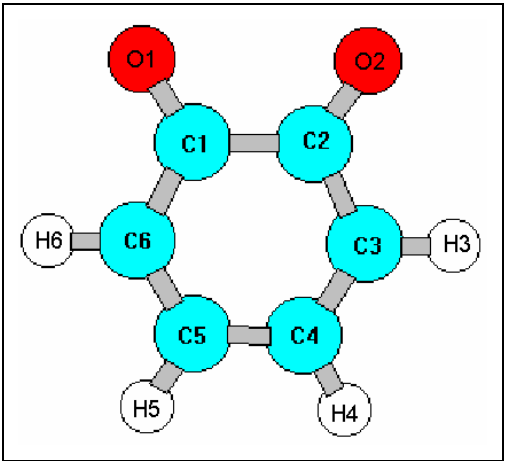

Fig. 1. *1,2-Benzosemiquinone radical*

Calculation of hyperfine coupling constants

The hyperfine coupling constants of magnetic nuclei arises from the Fermi contact interaction between the unpaired electron and the nucleus [11,12] and are given by

$$A_n = \frac{2\mu_0}{3} g_e \mu_B g_n \mu_N \frac{1}{h a_0^3} Q(0) \tag{1}$$

Here, A_n is in Hz, g_e and g_n are the electron and nuclear g factors, μ_B and μ_N are the Bohr and the nuclear magneton respectively, μ_0 is the vacuum magnetic permeability, h is the Planck constant, a_0 is the first Bohr radius and Q (0) represents the spin density at the nucleus n. Whereas $g_e \mu_B g_n \mu_N \frac{1}{h a_0^3}$ is a constant for a specific nucleus, Q (0) has to be obtained from quantum theoretical calculations, based on the equation

$$Q(0) = \left\langle \Psi \middle| \rho(r_n) \middle| \Psi \right\rangle \tag{2}$$

where ρ (r_n) is the spin density operator evaluated at the position of the nucleus n:

$$\rho(r_n) = \sum_k 2 s_{zk} \delta(r_k - r_n) \tag{3}$$

r_k being the position vector of the k-th electron, s_{zk} is the individual electron spin angular momentum of the k-th electron, and δ (r) is the Dirac delta function.

The interaction between the nucleus and the unpaired electron depends upon the s character of the singly occupied molecular orbital at the particular atom. Thus, it is necessary to have representative geometry parameters for the radical and a wavefunction that describes the area at the nucleus in detail.

Effects of the solvent

The polarized solvent generates an electrostatic field, called a reaction field, at each solute molecule. This reaction field alters the electronic wavefunction of the solute molecule from its state in the gas phase and produces an induced dipole moment that adds to the permanent dipole moment of the solute. The molecular electronic wave function is therefore changed from its gas phase state and all molecular properties in solution will be altered. Because an additional moment is induced by the solvent's reaction field, a polar molecule will experience a larger moment in a polar solvent than in gas phase. A practical approach to account for solvent effects is to use a self-consistent reaction field (SCRF) method, in which the solvent is treated not as a system of molecules with various orientations but as a continuous dielectric that surrounds the cavity containing the solute molecule.

The interaction between a solute molecule and the surrounding dielectric is represented by an additional term added to the gas-phase electronic Hamiltonian operator for the molecule.

a) Onsager Model

Onsager reaction field model [9] assumes that the solute molecule is placed in a spherical cavity, with radius a_o, embedded in a continuos medium defined by a dielectric constant ε. The simplest approach to obtain the cavity radius is from the solute molar volume (V_m) which is given directly by experiment or from the greatest internuclear distance and then by adding the van der Waals radii of the two atoms involved. This method is able to provide reasonable estimates of solvents effects in conformational equilibria and rotational barriers studies.

b) Isodensity Polarizable Continuum Model (IPCM)

This model was initially proposed by the group of Tomasi [13,14]. The solute cavity is specified as a set of fixed, intersecting atomic spheres, and the electrostatic multipole expansion includes higher order terms. In this model the cavity has a more realistic shape, as an isosurface of the total molecular electron density [10] and it is determined during the calculation of the molecular energy. The electronic wave function of the solute and hence the size of the molecular cavity changes in each SCRF iteration. Therefore, the cavity shape corresponds to the reactive shape of the molecule.

Computational Details

For the radical systems, we used *Ab Initio,* UHF and DFT methods. The basis sets used represent two distinct groups: the Pople's 4-31G and 6-31G series up to 6-31+G (d) [17] and the new specially tailored for hfcc's calculations EPR-II and EPR-III basis sets of Barone [21,22,33]. For Density Functional calculation the hybrid B3LYP functional [25,26] has been chosen due to the fact that it proved its ability for reproducing the free radical properties with high accuracy [8,21-24,32,34]. The force constant matrices calculated for all stationary points were checked to have no negative eigenvalues in order to ensure that they are minima on the potential energy surface. During the optimization process the geometry of the radical has been constrained to C_{2v} symmetry. Comparative hfcc's calculations were also performed using the semiempirical INDO method in conjunction with optimized radical geometry at different *Ab Initio* and DFT levels of theory. We have also tested the INDO method because it is capable of calculating negative spin densities arising from electron correlation since it uses unrestricted wave functions. It is also able to account for spin polarization by including one-center exchange integrals, so that unpaired spin arises naturally in the 1s orbitals of hydrogen atoms attached to aromatic carbon atoms. The INDO method is thus the least complex semiempirical method available which is able to account in general for the observed features of the ESR spectra of free radicals and it is expected to work well only for radicals at or near their equilibrium geometries and also, with no unusual bonding situations.

The Self-Consistent Reaction Field method (SCRF) [9,15] (Onsager and IPCM models) was used to model the long-range environmental effects on hyperfine couplings. All the calculations were performed using the GAUSSIAN 98W program package.[16]

Results and Discussion

1. Geometry

Selected bond lengths and angles for 1,2-BSQ radical in its free (gas-phase) form, calculated at different levels of theory with various basis sets, are given in Table 1.

Table 1.

Calculated bond lengths and angles of 1,2-BSQ radical in its free form using different basis sets. (bond lengths in Å and angles in degrees)

Geometrical parameter	UHF 6-31+G (d)	UHF EPR II	UHF EPR III	B3LYP 6-31+G(d)	B3LYP EPR-II	B3LYP EPR-III
$C_1 - O_1$	1.237	1.237	1.228	1.259	1.259	1.250
$C_1 - C_2$	1.496	1.502	1.498	1.516	1.523	1.513
$C_2 - C_3$	1.440	1.444	1.438	1.448	1.454	1.443
$C_3 - C_4$	1.367	1.373	1.362	1.382	1.388	1.373
$C_4 - C_5$	1.417	1.420	1.412	1.423	1.428	1.417
$C_3 - H_3$	1.077	1.079	1.075	1.089	1.089	1.085
$C_4 - H_4$	1.078	1.080	1.076	1.090	1.090	1.085
$C_1C_2C_3$	116.8	116.8	116.7	116.7	116.8	116.6
$C_2C_3C_4$	123.0	122.9	123.0	122.9	122.8	122.9
$C_3C_4C_5$	120.2	120.3	120.3	119.5	120.4	120.4
$O_2C_2C_3$	121.5	121.6	121.7	121.7	121.8	121.8
$O_2C_2C_1$	121.8	121.6	121.7	121.6	121.5	121.5
$H_4C_4C_3$	120.1	120.1	120.1	120.1	120.1	120.1
$H_3C_3C_4$	120.9	120.9	120.8	121.0	121.0	121.0

To our knowledge, there is no experimental data characterizing the geometry of the radical, so the calculated values are compared with experimental and theoretical results for other organic molecules [17]. As one can see from Table 1 there is an evident similarity between geometries calculated by different methods, the major difference being noted for the skeletal bond lengths, which comes out slightly longer with DFT method with respect to UHF. However, no consistent trend is observed by passing from a basis set to another within the same computational method. On closer examination of the bond lengths it is observed that the C3-C4 and C4-C5 bonds are shorter than the C1-C2 and C2-C3 bonds. This suggests more delocalisation of the electron distribution in the lower part of the ring compared with the upper part (see Figure 1). One explanation for these geometrical features is given by the classical resonance structures of the radical which suggest a localization of the unpaired electron mainly at C1 and C2 positions. In this resonance forms there is the greatest amount of double bond character for C3-C4 and C5-C6 and the least for C1-C2, C2-C3 and C1-C6. C-O calculated bonds are closer to the experimentally observed C=O double bond lengths in para-benzoquinone (1.225 Å) [27] than to the C-O single bond lengths in phenol (1.375 or 1.381 Å) [28]. This is even more evident for the UHF case. It is worth to mention also that the calculated C-O bond in gas phase at B3LYP/EPR-II level is slightly shorter than the calculated C-O bond (1.27 Å) in 1,4-BSQ, at the same level of theory [8]. The C-H bond lengths obtained at UHF level of theory are generally shorter than those calculated by DFT method. The C-H bond lengths of phenol for example, were reported to range from 1.083 Å to 1.087 Å [28] and we would expect that the C-H distance of the 1,2-BSQ anion are similar because the radical's unpaired electron occupies primarily π atomic orbitals. Thus the DFT C-H distances are closer to those experimentally determined C-H distance in closed-shell molecules and are likely to be closer to the real C-H distance in the radical. No major angular changes are found between the used methods or basis sets. However, the narrowing of the C1C2C3 angle and simultaneously widening of C2C3C4 angle with respect to the benzene molecule suggest a compression of the radical along the C3-C6 direction, which is consistent with the above observations for C-C and C-O bonds.

2. Isotropic Hyperfine Couplings

a) Experimental hyperfine coupling constants

Many experimental studies have been reported on hyperfine structure of 1,2-BSQ radical. The hfcc's have been measured in different solvents with dielectric constant ranging from 5.4 to 78.4. As easily can be seen in Table 2, were all the available experimental data [5] are collected, the hfcc's are highly sensitive to the impact of solvent. Thus, the smaller $A_{H3,H6}$ isotropic hfcc's are between –0.6G (for methanol) and –1.56G (for hexamethylphosphoric acid). The greater $A_{H4,H5}$ values are ranging from –3.82 G (for methanol) to –3.30G (for acetonitrile). As a general trend, it can be observed that the smaller the $A_{H3,H6}$ value, the greater $A_{H4,H5}$ constant. However, even accounting for the experimental errors, it can not be concluded that the sum of the four proton hfcc's is constant over all the solvents.

The strong influence of the solvent effects on the hfcc's is expected due to the dipolar moment which this molecule posses. The situation is contrary for 1,4-BSQ radical which has no permanent dipolar moment. For the later molecule the four protons are magnetically equivalent with an isotropic hfcc's between –2.2G (for ethylene glycol) and –2.44G (for hexamethylphosphoric acid).

Table 2.

Experimental hyperfine coupling constants of 1,2-BSQ radical in different solvents [5]

Solvent	dielectric constant	$A_{H3,H6}$ (G)	$A_{H4,H5}$ (G)
2-methyltetrahydrofuran (MeTHF)	5.4	-1.20	-3.44
ethanol (EtOH)	24.5	-0.93	-3.59
hexamethylphosphoric acid (HMPA)	30.0	-1.56	-3.34
methanol (MeOH)	32.6	-0.60	-3.82
acetonitrile (MeCN)	36.6	-1.50	-3.30
dimethylformamide (DMF)	36.7	-1.28	-3.48
dimethylsulfoxide (DMSO)	46.7	-1.39	-3.45
water	78.4	-0.75	-3.68

b) Calculated data

First we optimized and calculated hfcc's of the radical in gas phase. The geometries are those given in Table 1 and the computed hfcc's are shown in Table 3. Since the optimizations resulted always in a planar C_{2v} structure, the H3 with H6 and H4 with H5 protons are magnetically equivalent, as observed experimentally.

Table 3.

Calculated hyperfine coupling constants of gas-phase 1,2-BSQ radical using different methods and basis sets.

Method / Basis set	Energy (u.a.)	$<S^2>$	Dipole moment (Debye)	$A_{H3,H6}$ (G)	$A_{H4,H5}$ (G)	$A^{INDO}_{H3,H6}$ (G)	$A^{INDO}_{H4,H5}$ (G)
UHF/ *4 –31G*	-378.70	0.91 / 0.76	6.24	-0.65	-6.42	-0.48	-2.80
UHF/ *6 –31+G(d)*	-379.27	0.86 / 0.75	5.97	-2.61	-5.94	-0.84	-3.32
UHF/ EPR II	-379.33	0.87 / 0.75	5.66	-2.43	-6.02	-0.84	-3.41
UHF/ EPR III	-379.41	0.86/ 0.75	5.73	-2.95	-5.25	-0.93	-3.36
B3LYP/ *4 – 31G*	-380.99	0.76 / 0.75	5.72	-2.39	-3.07	-0.39	-3.06
B3LYP/ *6-31+G(d)*	-381.53	0.76 / 0.75	5.89	-2.70	-2.76	-0.64	-3.39
B3LYP/ EPR II	-381.58	0.76 / 0.75	5.42	-2.67	-2.78	-0.65	-3.49
B3LYP/ EPR III	-381.68	0.76 / 0.75	5.66	-2.71	-2.49	-0.73	-3.38

Ab Initio and DFT methods with different basis sets were used to calculate the isotropic hyperfine couplings of the radical. In any case, the spin densities have been computed after geometry optimization with the same basis set. The isotropic Fermi contact arises from the presence of finite unpaired electron density at the nucleus in question. The unpaired electron is located in a π-type orbital and hence, unpaired spin density arises at the proton positions *via* a delicate balance of various spin polarization mechanism [19,20], giving negative splitting constants. The single occupied molecular orbital (SOMO) plot is shown in Figure 2 and it can be seen that the molecular orbital is bonding between C1-C6 and C2-C3 atoms and nonbonding between C3-C4, C5-C6 and C-O atoms. As shown in Table 3, lower total energies of the radical are obtained by DFT method with respect to UHF case. Improving the quality of the basis set within the same computational approach results again in lowered energies.

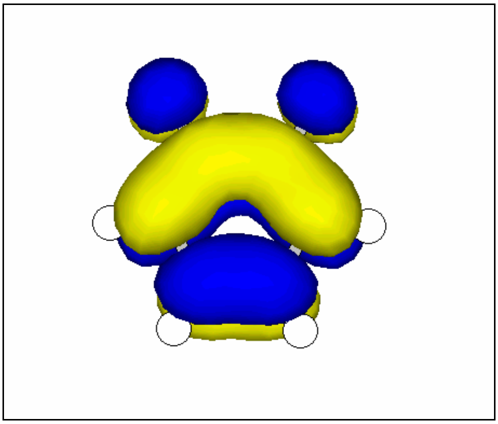

Fig. 2. *α highest single occupied molecular orbital for 1,2-BSQ at UHF/6-31G level contoured at 0.001 /au^3. The radical orientation is as shown in Figure 1*

The third column in Table 3 contains the expectation value of the spin operator $\mathbf{S^2}$. A high spin contamination of the wavefunction, reflected in large <S^2> values, can affect the geometry and population analysis and significantly alter the spin density. It is generally accepted [18] that the spin contamination is negligible if the value <S^2> differs from S (S+1) (i.e. 0.750 for pure doublet states) by less than 10%.

It is well known that the UHF approach has the severe drawback of providing wave functions that are not exact eigenfunctions of the $\mathbf{S^2}$ operator because the description of the doublet ground state of radicals is contamined by some contributions of higher spin multiplicities (quartet, sextet, etc.). Some techniques exist [35] that annihilate this spin contamination and they are implemented in the Gaussian 98W program package. In Table 3 the $<S^2>$ values are given before/after spin annihilation. Even after removing the spin contamination, the UHF method give very unsatisfactory hfcc's, clearly due to the overestimation of spin polarization. Surprisingly, the 4-31G basis set provide $A_{H3,H6}$ within the range of experimental data but this is most probably an effect of fortuitous cancellation of errors. On the other hand, the corresponding $<S^2>$ value obtained by pure functionals in the unrestricted Kohn-Sham (UKS) formalism upon which the DFT methods are based [36], is very close to the theoretical value for the pure spin state. However, for the hybrid B3LYP functional the spin contamination can not be neglected due to the inclusion of the exact exchange energy given by Hartree-Fock theory. Anyway, a substantial improving of the calculated $A_{H4,H5}$ values is obtained in this case, values quantitatively lowered under the corresponding experimental counterparts. It seems that contrary to the UHF formalism, DFT method underestimates the spin polarization of 1s orbitals of the H4 and H5 hydrogens. Instead, $A_{H3,H6}$ values are still overestimated by a factor of about 3, being very close to the $A_{H4,H5}$ values, in total disagreement with experimental findings. The zero-order direct contributions arising from the orbitals singly occupied by the unpaired electron contributes directly for anisotropic dipolar couplings and for isotropic Fermi contact couplings only in the case of sigma radicals. Thus, this mechanism cannot be responsible for the unpaired spin density at H3 and H6 positions and in conclusion the wrong $A_{H3,H6}$ values are due to an appreciable overestimation of spin polarization of 1s corresponding orbitals. The situation is more intriguing because it is totally opposed to the 1,4-BSQ radical where the hfcc's are very well reproduced even for the gas-phase radical [8].

The INDO method has been tested in calculating the hfcc's for the radical in gas phase optimized at different levels of theory. Surprisingly, with this method a much better quantitative agreement was obtained between the experimental data and calculated hfcc's values, especially for the B3LYP / EPR-II and B3LYP / EPR-III optimized geometries.

For instance, the relative errors of the calculated hfcc's at INDO// B3LYP/EPR-II level, are 1.3% for $A_{H3,H6}$ and 5% for $A_{H4,H5}$ when compared with the corresponding values in water. This agreement is hard to surpass in quality by the use of high level *Ab Initio* or DFT methods. For comparisons the corresponding errors at B3LYP/EPR-II and B3LYP/EPR-III are 25.6% and 24% respectively. The same excellent agreement given by INDO method has been also reported by Sinnecker *et al.*[29] in a study of hfcc's of *bacteriochlorophyll a* radical cation and anion. Further studies are necessary to elucidate why this method works so well on this radical while in the case of 1,3- and 1,4-BSQ radicals it performs much worse [31].

Solvent Effects

Two models have been used in order to test the influence of environmental surrounding on the hyperfine structure of 1,2-BSQ, namely the Onsager [9] and IPCM [14]. The hfcc's have been calculated in single point runs for all the solvents for which experimental data exist and the results are summarized in Table 4. For these calculations we used the optimized B3LYP/EPR-II geometry of the gas-phase radical. A value of 4.03Å has been obtained from molecular volume calculations (so called *Volume* algorithm in Gaussian 98 [10]) for the cavity radius to be used with Onsager model and the solute-solvent interaction was treated at the dipole level. The molecular structure of the radical was not optimized for each different value of ε because it was shown that the influence of the solvent field on the geometrical parameters is minimal [23]. In the limits of Onsager model, the dipole moment changes significantly between the gas-phase (5.42D) and MeTHF (7.30D) and then remains nearly constant until water (7.89D). These changes are even more evident in the IPCM model and indicate that the radical is strongly polarized by the dielectric surroundings. The strongly polarized electronic structure should essentially influence the spin density distribution of the radical.

Indeed, as shown in Fig.3, a complete rearrangement of spin density distribution occurs by considering the solvent effects.

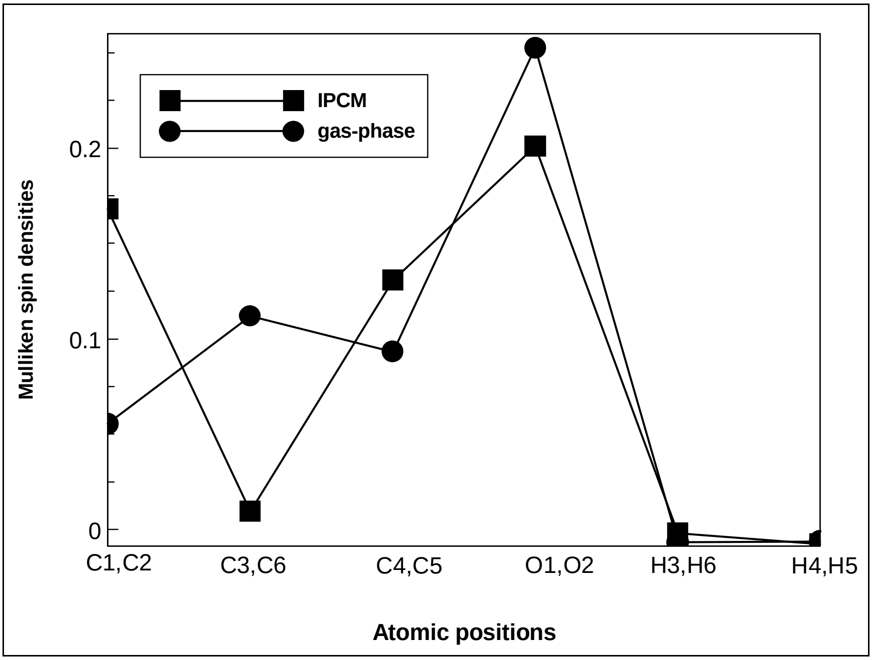

Fig. 3. *Mulliken spin densities on atomic centers in gas phase and solvated 1,2-BSQ radical.*

A substantial reduction of spin densities on C3, C6 atoms, simultaneously with an increasing on C4, C5 centers is observed in IPCM model. However, the highest spin density, about 50% for gas-phase and 40% for IPCM, is localized on the oxygen atoms.

The Onsager model does not lead to a good matching between the calculated and experimental hfcc's, the only gains being a better separation of the calculated values. While $A_{H4,H5}$ values are in qualitative agreement with experimental determinations with a 15% medium relative errors, $A_{H3,H6}$ values with a 112% medium relative errors, still remain too far away from the experimental range.

Table 4.

B3LYP/EPR-II calculated isotropic hyperfine couplings of 1,2-BSQ radical on B3LYP/EPR-II gas-phase geometry by using Onsager and IPCM solvation models.

Solvent	Onsager			IPCM		
	Dipole moment (Debye)	$A_{H3,H6}$ (G)	$A_{H4,H5}$ (G)	Dipole moment (Debye)	$A_{H3,H6}$ (G)	$A_{H4,H5}$ (G)
MeTHF	7.30	-2.34	-2.90	9.87	-1.34	-3.29
EtOH	7.78	-2.19	-2.98	11.02	-0.95	-3.49
HMPA	7.81	-2.18	-2.98	11.28	-0.93	-3.50
MeOH	7.82	-2.18	-2.99	11.31	-0.91	-3.51
MeCN	7.83	-2.18	-2.99	11.34	-0.91	-3.51
DMF	7.83	-2.18	-2.99	11.35	-0.91	-3.51
DMSO	7.85	-2.17	-2.99	11.41	-0.89	-3.52
H_2O	7.89	-2.16	-3.00	11.49	-0.86	-3.54

The same trend of increasing the $|A_{H4,H5}|$ and simultaneously decreasing the $|A_{H3,H6}|$ values by increasing the dielectric constant, observed on computed gas-phase hfcc's is valable for both Onsager and IPCM models.

Because the Onsager model fails to quantitatively reproduce the hfcc's we switched to the IPCM solvation model for which we must provide the isodensity value, an empirical parameter which characterize the isosurface of the total molecular electron density. As seen in Fig.4, the most affected calculated hfcc's by varying the isodensity parameter are $A_{H3,H6}$, calculated with a mean relative error of 13% with respect to 3% for $A_{H4,H5}$ values over the investigated range of isodensity. The best isodensity value for water seems to be 0.0035, level at which the experimental hfcc's are reproduced with a mean relative error of only 2%. As seen in Table 4, the same overall very good agreement is obtained for all the solvents investigated.

In addition it is worth to note that the dependence of the calculated hfcc's with ε follows a continuous curve, while the variation of those experimentally determined shows marked discontinuities around ε=30, both for $A_{H3,H6}$ and $A_{H4,H5}$ values. Most probably, these discrepancies are due to the experimental errors.

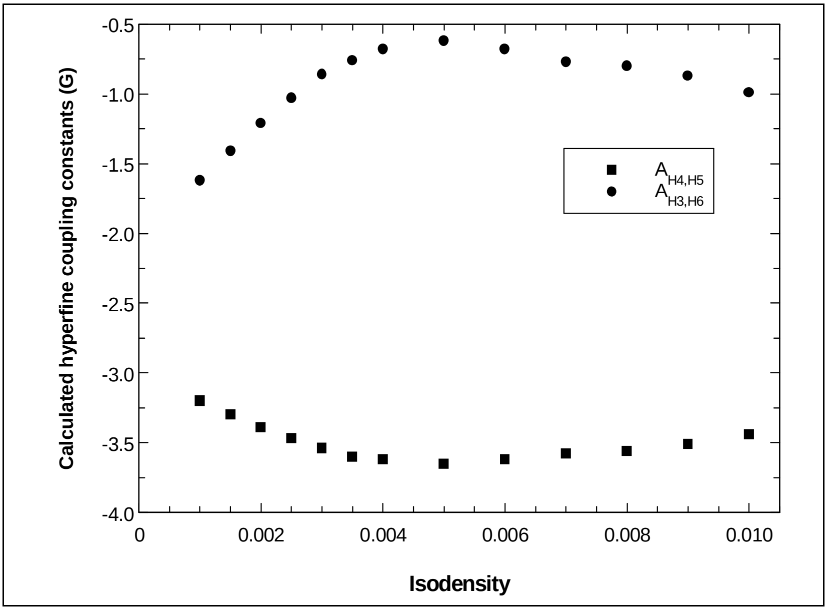

Fig. 4. *Predicted proton hfcc's of 1,2-BSQ radical in water as a function of surface isodensity*

Conclusions

In the present study, geometry and hyperfine coupling constants for 1,2-benzosemiquinone anion radical were calculated through the use of INDO, *Ab Initio*, and Density Functional methods. Geometrical features suggest a quinoid structure of the radical with an increased delocalisation of the electron distribution between C3-C4 and C5-C6 positions.

Hfcc's have been calculated for the gas phase and solvated radical (Onsager and IPCM models). It is shown that conventional UHF method is not at all suited for predicting hfcc's due to a high spin contamination of the wave function. Even DFT method provide poor results for the gas-phase free radical, especially by an increased overestimation of the 1s orbitals of H3 and H6 hydrogens. On the other hand a very good agreement has been obtained between the INDO calculated hfcc's and the experimental ones, especially for the gas-phase B3LYP/EPR-II optimized geometry.

The Onsager solvation model does not provide a good consistency between the calculated and experimental hfcc's. The situation is drastically changed within the IPCM model for which we reproduced the experimental hfcc's with a high level of accuracy. For water, an isodensity of 0.0035 was found as the best value for matching the theoretical and experimental hfcc's. The later have been reproduced with a mean deviation of no more than 6%. Especially, $A_{H4,H5}$ values were calculated with mean relative errors of 4% over all the used solvents.

REFERENCES

1. M. Y. Okamura, G. Feher, *Annu. Rev. Biochem.*, 61,861 (1992).
2. H. Kurrek, M. Huber, *Angew. Chem. Int. Ed. Engl.,* 34,849 (1995); H. Kurrek, S. Aguirre, S. N. Batchelor, H. Dieks, J. V. Gersdorff, C. W. M. Kay, H. Möβler, H. Newman, D. Niethammer, J. Schlupmann, J. Sobek, M. Speck, T. Stabingis, L. Sun, P. Tian, A. Wiehe, K. Möbius, *Solar Energy Materials and Solar Cells,* 38, 91 (1995).
3. M. Delgado, R. E. Wolf Jr., J. R. Hartman, G. McCafferty, R. Yagbasan, S. C. Rawle, D. J. Watkin, S. R. Cooper, *J. Am. Chem. Soc.,* 114, 8983 (1992)
4. L. Sun, J. V. Gersdorff, D. Niethammer, P. Tian, H. Kurreck, *Angew. Chem. Int. Ed. Engl.,* 33, 2318 (1994).
5. J. A. Pedersen, *CRC Handbook of EPR Spectra from Quinones and Quinols,* CRC Press, Boca Raton, Florida, 1985.
6. V. Barone, C. Adamo, N. Russo, *Chem. Phys. Lett.,* 5, 212 (1993).
7. L. A. Eriksson, P. L. Malkina, V. G. Malkin, D. R. Salahub, *J. Chem. Phys*, 100, 5066 (1994).
8. P. J. O'Malley, *J. Phys. Chem.,* 101, 6334 (1997).
9. M. W. Wong, M. J. Frisch, K. B. Wiberg, *J. Am. Chem. Soc.,* 113, 4776 (1991).
10. J. B. Foresman, T. A. Keith, K. B. Wiberg, J. Snoonian and M. J. Frisch, *J. Phys. Chem.,* 100, 16098 (1996); J. B. Foresman, A. Frisch, *Exploring Chemistry with Electronic Structure Methods*, 2nd ed., Gaussian Inc., Pittsburg, PA, (1996).
11. E. Fermi, *Z. Phys.,* 60, 320 (1930)
12. J. A. Weil, J. R. Bolton, J. E. Wertz, *Electron Paramagnetic Resonance,* Wiley, New York, 1994.
13. S. Miertus, J. Tomasi, *Chem. Phys.* 65, 239 (1982).
14. S. Miertus, S. Scrocco, J. Tomasi, *Chem. Phys.* 55, 117 (1981).
15. M. Karelson, T. Tamm, M. C. Zerner, *J. Phys. Chem.,* 97, 11901 (1993).

16. *Gaussian 98, Revision A. 7*, M. J. Frisch, G. W. Trucks, H. B. Schlegel, G. E. Scuseria, M. A. Robb, J. R. Cheeseman, V. G. Zakrzewski, J. A. Montgomery, Jr., R. E. Stratmann, J. C. Burant, S. Dapprich, J. M. Millam, A. D. Daniels, K. N. Kudin, M. C. Strain, O. Farkas, J. Tomasi, V. Barone, M. Cossi, R. Cammi, B. Mennucci, C. Pomelli, C. Adamo, S. Clifford, J. Ochterski, G. A. Petersson, P. Y. Ayala, Q. Cui, K. Morokuma, D. K. Malick, A. D. Rabuck, K. Raghavachari, J. B. Foresman, J. Cioslowski, J. V. Ortiz, A. G. Baboul, B. B. Stefanov, G. Liu, A. Liashenko, P. Piskorz, I. Komaromi, R. Gomperts, R. L. Martin, D. J. Fox, T. Keith, M. A. Al-Laham, C. Y. Peng, A. Nanayakkara, C. Gonzalez, M. Challacombe, P. M. W. Gill, B. Johnson, W. Chen, M. W. Wong, J. L. Andres, C. Gonzalez, M. Head-Gordon, E. S. Replogle, and J. A. Pople, Gaussian, Inc., Pittsburgh PA, (1998).
17. W. J. Hehre, L. Radom, P. v. R. Schleyer, J. A. Pople, *"Ab Initio" Molecular Orbital Theory*, John Wiley & Sons, New York, 1986.
18. M. W. Wong, L. Radom, *J. Phys. Chem.,* 99, 8582 (1995).
19. W. Gordy, *Theory and Applications of Electron Spin Resonance,* Wiley, New York, 1980.
20. M. J. Cohen, D. P. Chong, *Chem. Phys. Lett.,* 234, 405 (1995).
21. V. Barone, in: D. P. Chong (Ed.) *Recent Advances in Density Functional Methods*, Part I, World Scientific Publishing, Singapore, 287 (1994).
22. C. Adamo, V. Barone, A. Fortunelli, *J. Chem. Phys.,* 102, 384 (1995).
23. M. Langaard, J. Spanget-Larsen, *J. Molec. Struct. (Theochem)*, 431, 173 (1998).
24. S. Naumov, A. Barthel, J. Reinhold, J. Geimer, D. Beckert, *Phys. Chem. Chem. Phys*., 2, 4207 (2000).
25. A. D. Becke, *J. Chem. Phys.,* 98, 5648 (1993).
26. C. Lee, W. Yang, R. G. Parr, *Phys. Rev. B*, 37, 785 (1998).
27. K. Hagen, K. Hedberg, *J. Chem. Phys.,* 59, 158 (1973).
28. G. Portalone, G. Schultz, A. Domenicano, I. Hargittai, *Chem. Phys. Lett.,* 197, 482 (1992).
29. S. Sinnecker, W. Koch, W. Lubitz, *Phys. Chem. Chem. Phys*., 2, 4772 (2000)
30. G. N. R. Tripathi, D. M. Chipman, C. A. Miderski, H. F. Davis, R. W. Fessenden, R. H. Schuler, *J. Phys. Chem.,* 90, 3968 (1986).
31. V. Chiş, manuscript in preparation.
32. J. W. Gauld, L. A. Eriksson, L. Radom, *J. Phys. Chem. A*, 101, 1352 (1997).
33. N. Rega, M. Cossi, V. Barone, *J. Chem. Phys.,* 105, 11060 (1996).
34. C. W. Bauschlicher Jr., *Chem. Phys. Lett.,* 246, 40 (1995).
35. D. M. Chipman, *Theor. Chim. Acta*, 82, 93 (1992) and references therein.
36. R. G. Parr, W. Yang, *Density Functional Theory of atoms and molecules*, Oxford University Press, 1989.